1992

# Use of a Fourier deconvolution method in particle size determination and use of molecular mechanics in crystal structure determinations

Yingzhong Su
*Iowa State University*

## Recommended Citation

Su, Yingzhong, "Use of a Fourier deconvolution method in particle size determination and use of molecular mechanics in crystal structure determinations " (1992). *Retrospective Theses and Dissertations*. 9955.
https://lib.dr.iastate.edu/rtd/9955

# INFORMATION TO USERS

This manuscript has been reproduced from the microfilm master. UMI films the text directly from the original or copy submitted. Thus, some thesis and dissertation copies are in typewriter face, while others may be from any type of computer printer.

**The quality of this reproduction is dependent upon the quality of the copy submitted.** Broken or indistinct print, colored or poor quality illustrations and photographs, print bleedthrough, substandard margins, and improper alignment can adversely affect reproduction.

In the unlikely event that the author did not send UMI a complete manuscript and there are missing pages, these will be noted. Also, if unauthorized copyright material had to be removed, a note will indicate the deletion.

Oversize materials (e.g., maps, drawings, charts) are reproduced by sectioning the original, beginning at the upper left-hand corner and continuing from left to right in equal sections with small overlaps. Each original is also photographed in one exposure and is included in reduced form at the back of the book.

Photographs included in the original manuscript have been reproduced xerographically in this copy. Higher quality 6" x 9" black and white photographic prints are available for any photographs or illustrations appearing in this copy for an additional charge. Contact UMI directly to order.

U·M·I

University Microfilms International
A Bell & Howell Information Company
300 North Zeeb Road, Ann Arbor, MI 48106-1346 USA
313/761-4700 800/521-0600

Order Number 9223969

# Use of a Fourier deconvolution method in particle size determination and use of molecular mechanics in crystal structure determinations

Su, Yingzhong, Ph.D.

Iowa State University, 1992

U·M·I
300 N. Zeeb Rd.
Ann Arbor, MI 48106

# Use of a Fourier deconvolution method in particle size determination and use of molecular mechanics in crystal structure determinations

by

Yingzhong Su

A Dissertation Submitted to the
Graduate Faculty in Partial Fulfillment of the
Requirement for the Degree of
DOCTOR OF PHILOSOPHY

Department: Chemistry
Major: Physical Chemistry

Approved:

In Charge of Major Work

For the Major Department

For the Graduate College

Iowa State University
Ames, Iowa

1992

# TABLE OF CONTENTS

## SECTION II

## STRUCTURE DETERMINATION OF SELECTED SULFUR-CONTAINING ORGANOMETALLIC COMPOUNDS BY X-RAY DIFFRACTION AND MOLECULAR MECHANICS METHODS .......... 87

## SECTION III

## AN ALIGNMENT PROCEDURE FOR A HILGER-WATTS DIFFRACTOMETER ON A RIGAKU ROTATING ANODE X-RAY GENERATOR .... 127

# GENERAL INTRODDUCTION

X-ray crystallography plays an important role in the research of many scientific disciplines including chemistry, physics, biology, geology, and metallurgical/material science. Both powder and single crystal diffraction techniques can provide valuable information.

X-ray powder diffraction, although presenting all data in a one-dimensional fashion due to the random orientation of the small crystals as compared with the three-dimensional nature of the single crystal diffraction pattern, still has wide application in the above disciplines. One such application is the grain size determination of powder materials.

X-ray single crystal diffraction structure determination has become a routine tool, thanks to the development of the sophisticated computer software packages. In the course of pursuing my Ph.D. degree, I have solved a number of single crystal structures. Some of these structural results have been or are going to be published (see reference [8-13] in the end of Section II). Two of them are worth special mention because the investigations involved a combination of X-ray diffraction and molecular mechanics.

Alignment of a diffractometer to an X-ray generator is crucial in order to obtain accurate data for structure determination. But reliance on just the use of invisible X rays can be tedious and sometimes even hazardous, especially when a diffractometer is completely out of alignment.

In this dissertation, X-ray grain size determination of a powder sample, single crystal structure dertermination of selected metal complexes and an alignment procedure using ordinary optical telescopes to align a diffractometer to an X-ray generator will be discussed.

## Explanation of Dissertation Format

An alternate format is used in this dissertation. The whole dissertation is divided into three sections: Section I discusses X-ray grain size determination using a Fourier deconvolution method; Section II discusses single crystal structure determination combined with molecular mechanics calculation; Section III discusses optical alignment of a Hilger-Watts four-cycle diffractometer with a Rigaku rotating anode X-ray generator. The first two sections individually contain a separate list of references. Parts of Section I and Section II have been submitted for publication and presentation respectively. Section III is in the form of instruction for future routine use in our X-ray Lab. A General Summary and Acknowledgements are following the sections.

# SECTION I

# A FOURIER DECONVOLUTION METHOD FOR GRAIN SIZE STUDY VIA X-RAY POWDER DIFFRACTION

# INTRODUCTION

It is well known that, in metallurgical science, the grain size of the polycrystalline metal or alloy and, in material science, the grain size of the powdered materials sometimes have pronounced effects on many of their properties.

When the grain size is in the range of 100μm to 10μm, an optical microscope is suitable to measure the dimension of the particles.

The emergence of the electron microscope, with its much higher magnification whereby the image of the object can be seen on a CRT screen or in the form of photographs, makes it possible to "directly" measure the size of particles having dimensions as small as 100Å by the scanning electron microscope or 2.3Å by the transmission electron microscope.

However, when using such electron microscopes, the samples must undergo a series of treatment procedures, which often take days to complete. In addition to this disadvantage, only a small area of the sample facing the probe can be examined at any one time. This area is usually too small to represent the properties of the whole sample, and the individual result can lack statistical significance.

On the other hand, X-ray powder diffractometry provides a means to give a statistical estimate of the particle dimension of a sample of interest (of fine grain size) via a measurement of its peak broadening with respect to a standard sample (of coarse grain size > 1,000Å). It is relatively easy and features fast sample preparation. For example, data collection for the standard and the sample of interest can be carried out within several hours.

However, the most readily available computer programs which can be used to estimate grain size are the Rietveld refinement programs (see below), in which the recorded peaks are fit with a certain profile function having refinable parameters. Then the grain size can be calculated using the resulting FWHM's (Full - Width - at - Half - Maximum). However, the exact mathematical relation used is dependent on assumptions as to a particular peak shape.

It was shown[1] that the broadened peak of the sample of interest is a convolution of a peak width due to the grain size effect and a peak width characteristic of the instrument itself, i.e., the peak given by the standard sample. According to Klug & Alexander[2], the Fourier method is the "most powerful technique" for the deconvolution in order to obtain the pure grain size peak width from the recorded X-ray diffraction peaks.

In this section, a computer program is described which converts this theory into practice. Results of grain size thus determined are compared with those obtained from the Rietveld refinement program and with those determined using TEM techniques. In all of these studies, a powdered magnet material $Nd_2Fe_{14}B$ was used.

## SAMPLE DESCRIPTION

The rare earth-iron permanent magnets, of nominal combination $Nd_2Fe_{14}B$, have the highest magnetic properties yet discovered. The theoretical maximum energy product $[(BH)_{max}]$ for this magnet is about 64MGOe, while experimental energy products have reached as high as 40MGOe. The high coercivity of $Nd_2Fe_{14}B$ is due to the small grain size, which impedes the movement of magnetic domain walls. Recently Anderson[3] used high pressure gas atomization to produce the isotropic $Nd_2Fe_{14}B$ magnet.

The $Nd_2Fe_{14}B$ samples[4] were prepared stoichiometrically from 32.5wt% Nd, 66.2wt% Fe and 1.32wt% B, (of purity 99.99wt%, 99.9wt% and 99.2wt%, respectively). The mixture was arc melted several times to ensure that the resulting ingot had a homogeneous composition, then the ingot was melt-spinned with a 44 m/s copper wheel speed in an Ar atmosphere to form ribbons, some of which were used for subsequent grain size investigation. One part of the ribbon was annealed at 900 ± 10°C for one week to let the grains grow bigger to form the coarse, "standard" sample.

# TRANSMISSION ELECTRON MICROSCOPE (TEM) INVESTIGATION OF THE GRAIN SIZE

A powder of the fine grain size sample from the ribbon was mixed with copper and silver powder. The mixture was pelleted into a 3mm disc, then thinned with a Minimet grinding machine. The thin disc was ion milled with a cold stage.

A microstructure investigation of the sample so prepared was performed on a Philip's CM30 STEM electron microscope. The grain shape and grain size thus revealed are shown in Fig. I .1-I .3. It can be seen that the grain size for the region of the sample surveyed is in the range of *ca.* 350Å.

Determination of grain size via analysis of peak broadening of the X-ray diffraction patterns was next carried out.

Fig. I. 1 A transmission electron microscope photos of ribbon sample

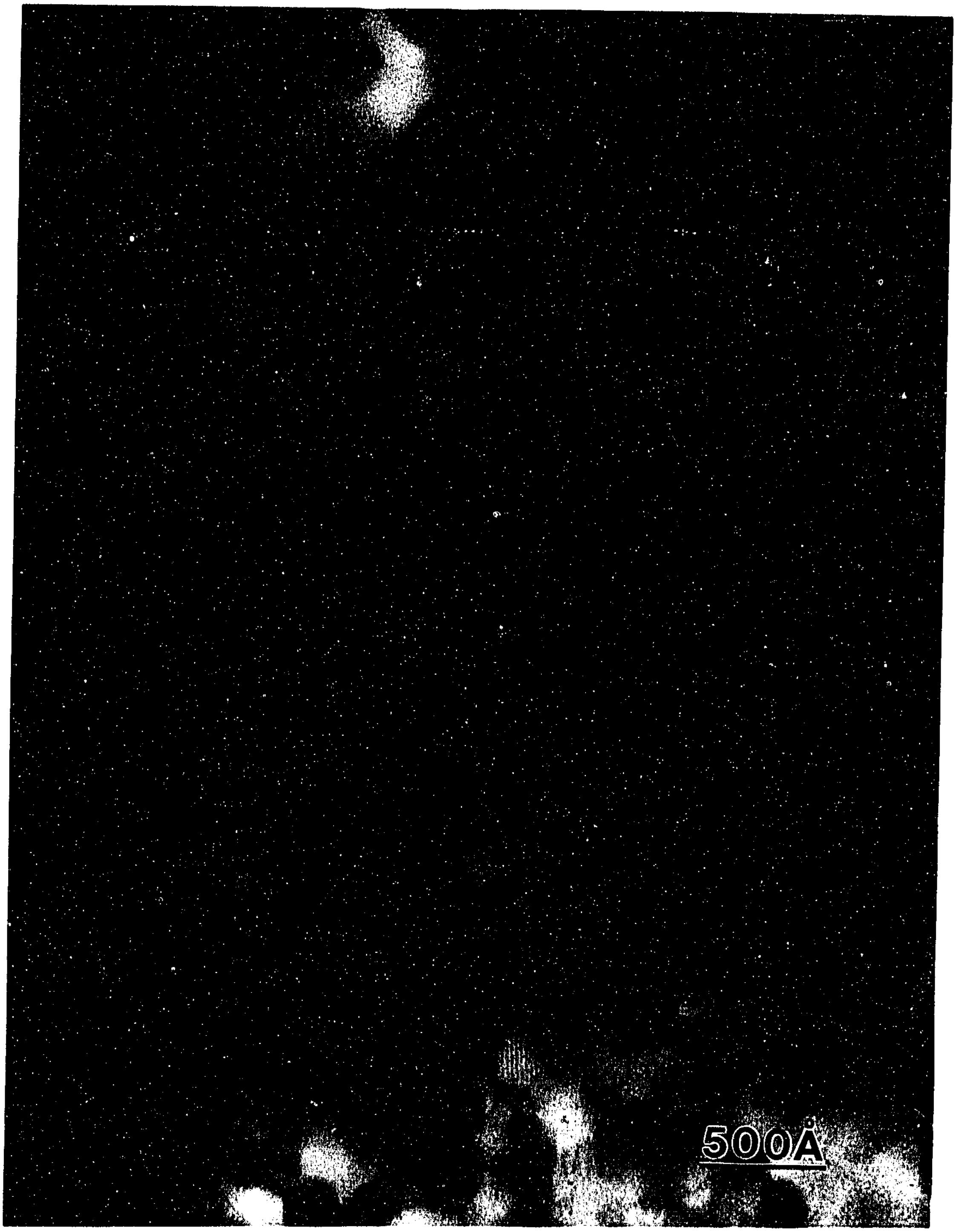
500Å

Fig. I. 2 A transmission electron microscope photos of ribbon sample

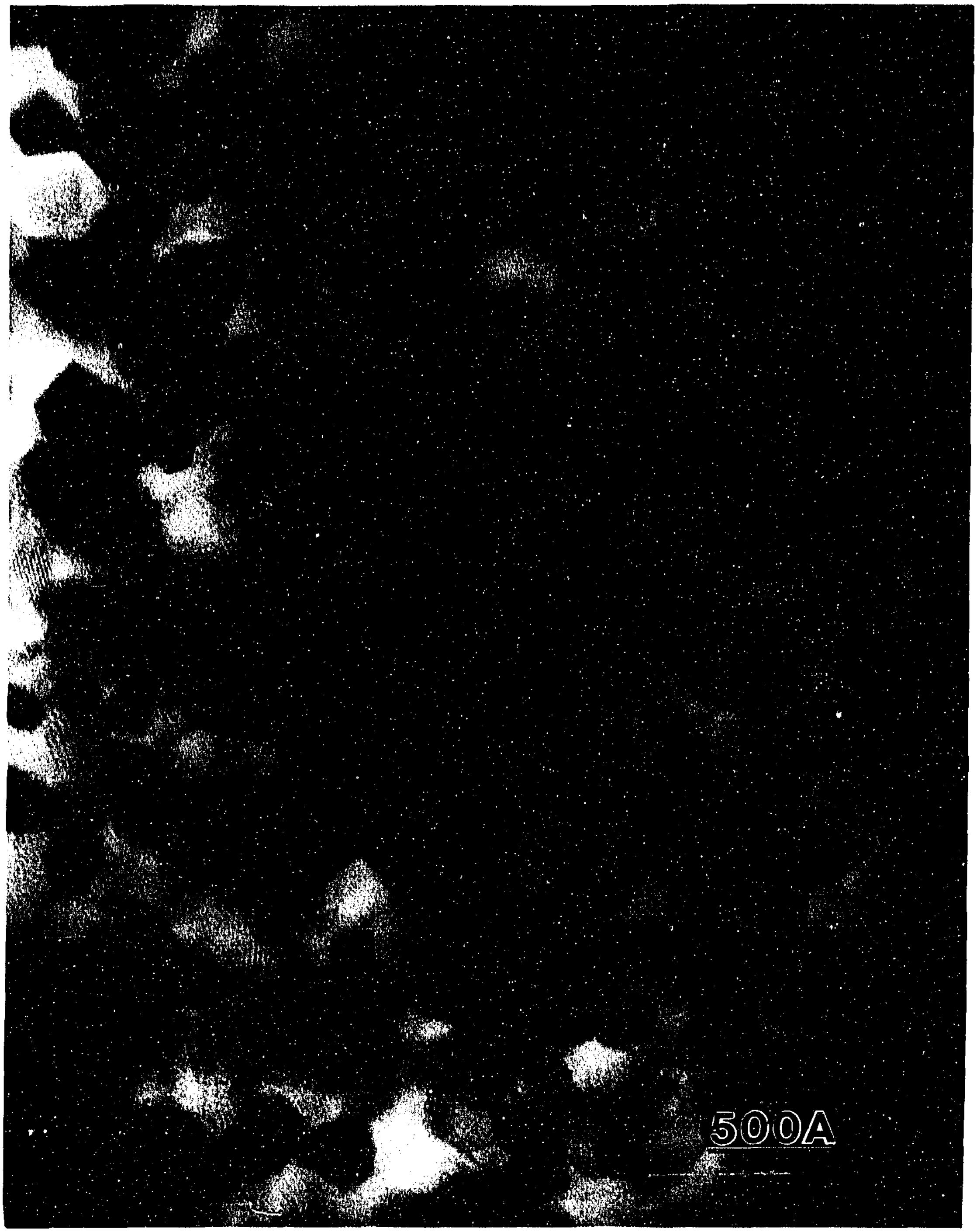
500A

Fig. I. 3 A transmission electron microscope photos of ribbon sample

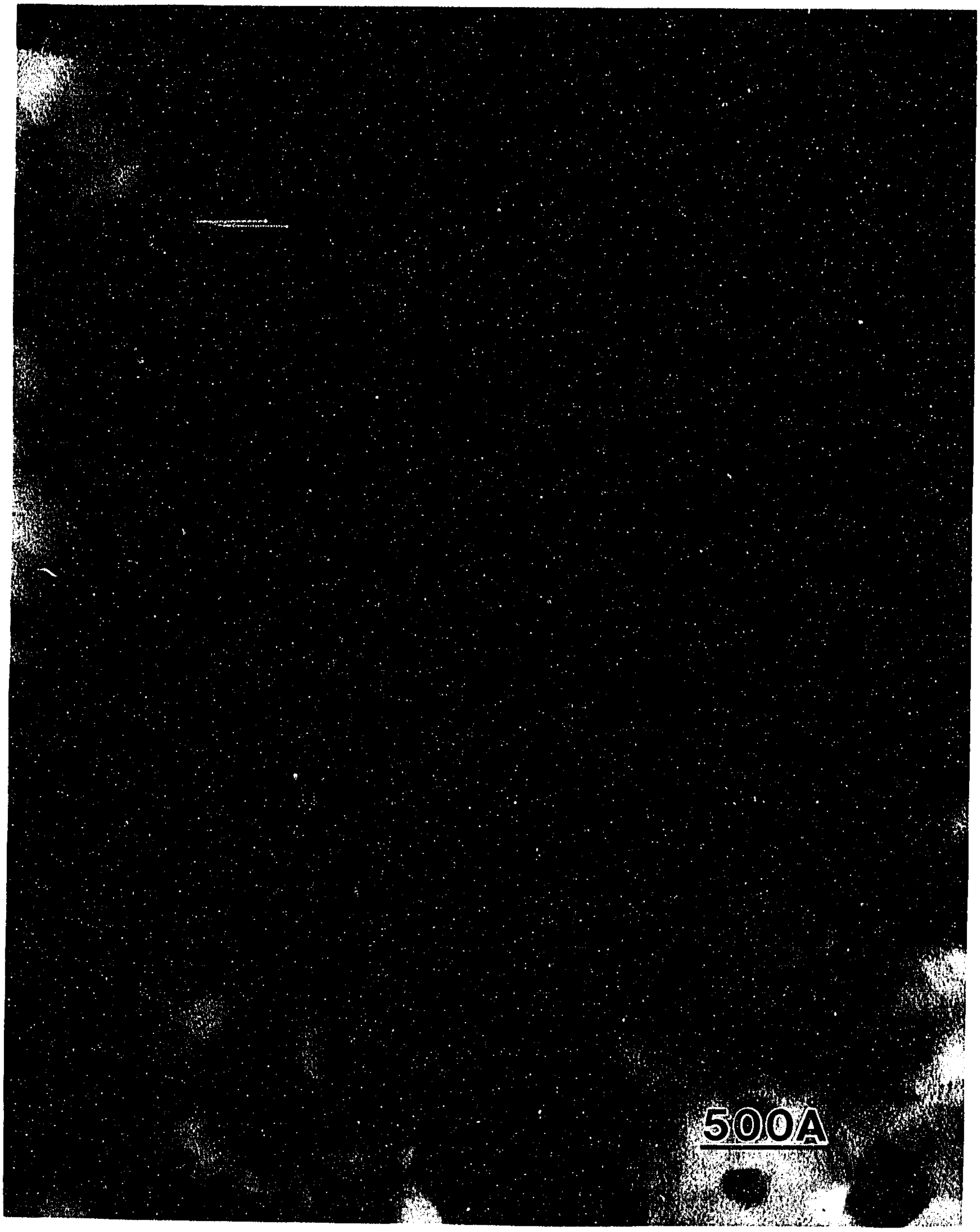

500A

## BROADENING OF DIFFRACTION PEAKS DUE TO THE GRAIN SIZE EFFECT

Grain size can be determined according to Scherrer's formula[5]:

$$t = \frac{K * \lambda}{B * \cos\theta} \tag{1}$$

where $t$ is the mean dimension of the grain, $\lambda$ the X-ray wave length, $\theta$ the peak position in the pattern, $K$ a constant usually of a value *ca.* 0.9, and $B$ is the pure X-ray diffraction broadening, i.e., the broadening of FWHM of the peak in question with respect to the corresponding FWHM of the "standard" peak.

Bragg[6] has given a simplified derivation of the Scherrer equation which can be represented as follows:

Referring to Fig. I .4, consider diffraction of X rays of wavelength $\lambda$ by a crystal grain in the form of a platelet. Suppose that the platelet consists of $p$ atomic (hkl) planes having the spacing $d$ with respect to each other and being parallel to the surface of the platelet. If $p$ is large enough, the thickness of the platelet $(p - 1)d \approx pd$.

Let $t_{hkl} = pd$. The relationship between $t_{hkl}$ and the intensity at the FWHM of the reflection (hkl) is to be found.

From Bragg's equation, if the path difference $\Delta l$ between the rays reflected

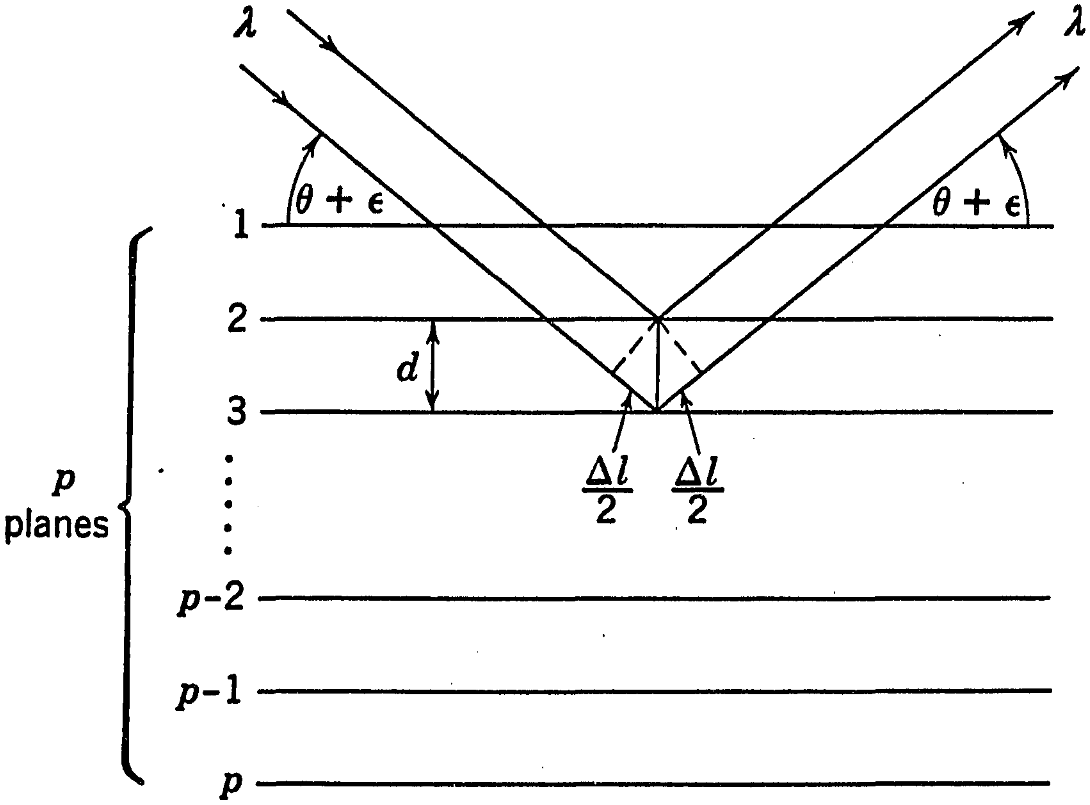

Fig. I.4. Diffraction of X-rays of wavelength λ by a crystal grain in the form of a platelet.

from successive planes is equal to the multiple of the wavelength $\lambda$, the amplitude of the diffracted beam will be a maximum:

$$\begin{aligned} n\lambda &= \Delta l \\ &= 2d\sin\theta \end{aligned} \tag{2}$$

When the glancing angle differs from $\theta$ By a small amount $\varepsilon$, the path difference may be written:

$$\begin{aligned} \Delta l &= 2d\sin(\theta+\epsilon) \\ &= 2d(\sin\theta\cos\epsilon+\cos\theta\sin\epsilon) \\ &= n\lambda\cos\epsilon+\sin\epsilon\, 2d\cos\theta \end{aligned} \tag{3}$$

with $\varepsilon$ in radians; since $\varepsilon$ is expected to be small, $\sin\varepsilon \approx \varepsilon$ and $\cos\varepsilon \approx 1$, and (3) can be written as

$$\Delta l = n\lambda + 2\epsilon d\cos\theta$$

The corresponding phase difference is

$$\begin{aligned} \frac{2\pi}{\lambda}\Delta l &= 2n\pi+\frac{4\pi}{\lambda}\epsilon d\cos\theta \\ &= \frac{4\pi\epsilon d\cos\theta}{\lambda} \end{aligned} \tag{4}$$

By well-known principles of optics[7], if $n$ equal vectors of amplitude $a$ differ in phase by successive uniform increments, the resultant amplitude is

$$A = an\frac{\sin\alpha}{\alpha} \tag{5}$$

$\alpha$ being one half of the phase difference between the first and last vectors of the series. Therefore, the phase difference between the first and the $p^{th}$ planes in Fig. I .4 is

$$\phi = \frac{4\pi p e d\cos\theta}{\lambda} \tag{5'}$$

and by equating $\alpha$ and $\phi/2$ according to (5), the resultant amplitude of the reflected wave is

$$A = \frac{ap\sin\frac{2\pi p e d\cos\theta}{\lambda}}{\frac{2\pi p e d\cos\theta}{\lambda}} \tag{6}$$

The amplitude of the reflected ray is a maximum when $\epsilon = 0$ and the reflected rays from all $p$ planes are in phase. Utilizing the knowledge that in (6) when $\phi$ becomes zero, one has:

$$\lim_{\phi\to 0}\frac{\sin\phi}{\phi} = 1$$

therefore

$$A_0 = ap \tag{7}$$

Knowing that the maximum intensity $I_0 = A_0^2$, at half-maximum intensity, according to (5)

$$\frac{\sin^2\frac{\phi}{2}}{\left(\frac{\phi}{2}\right)^2} = \frac{A^2}{A_0^2} = \frac{1}{2} \tag{8}$$

Bragg used a graphical scheme to find the solution of $\phi$ in equation (8), by plotting the left hand side of (8) against $\phi/2$, and he found that

$$\frac{\phi}{2} = 1.40$$

With $\epsilon_H$ being the angular deviation from the Bragg angle $\theta$ of the incident or the reflected rays, (5') now has the value

$$\frac{2\pi p \epsilon_H d \cos\theta}{\lambda} = 1.40$$

Thus, the full angular width at half-maximum intensity of the reflection

$$\begin{aligned} B_{hkl} &= 4\,\epsilon_H \\ &= 4 * \frac{1.40\,\lambda}{2\pi p d \cos\theta} \end{aligned}$$

and Scherrer's equation (1) is obtained with

$$\begin{aligned} K &= \frac{4 * 1.40}{2\pi} \\ &= 0.892 \end{aligned}$$

The author of this dissertation employed Newton - Raphson iteration

$$x_{r+1} = x_r - \frac{f(x_r)}{f'(x_r)} \qquad (9)$$

for the root $x$ of equation $f(x) = 0$, to find the solution of $\phi$ of equation (8):

$$\frac{\sin^2\frac{\phi}{2}}{\left(\frac{\phi}{2}\right)^2} = \frac{1}{2} \qquad (8')$$

Letting $x = \phi/2$, the equation becomes

$$\frac{\sin^2 x}{x^2} = \frac{1}{2}$$

whereas in (9), correspondingly

$$f(x) = 2\sin^2 x - x^2$$

and

$$f'(x) = 2\sin 2x - 2x$$

The iteration formula (9) becomes

$$x_{r+1} = x_r - \frac{2\sin^2 x - x^2}{2\sin 2x - 2x} \qquad (9')$$

Knowing that when $x = 1$

$$\frac{\sin^2 x}{x^2} = 0.70807$$

when $x = 2$

$$\frac{\sin^2 x}{x^2} = 0.20671$$

$x$ should have the value $1 < x < 2$.

Starting with $x_r = 1$, several iterations on (9') produced the converged value of $x = 1.391$ with $(x_{r+1} - x_r) < 10^{-8}$. This gives $K = 0.886$ for Scherrer's equation.

## DETERMINATION OF $B$ IN SCHERRER'S EQUATION

From the above derivation, $K$ is known to have the value of 0.886, and $B$ is defined as the Full-Width-at-Half-Maximum (FWHM) of the peak whose profile is purely due to the effects of small grain size.

In order to obtain $B$, X-ray diffraction data collection should be carried out on two samples of the material. The first sample is that of interest, i.e., of grain size less than 1,000Å, and will yield a diffraction pattern whose peak profile will be denoted as $h(\nu)$. The second sample is the "standard sample" of grain size > 1,000Å, giving a profile $g(\nu)$. If the peak $h(\nu)$ at the position $\nu_k$ of the first pattern has a FWHM of $B_h$ and the corresponding peak $g(\nu)$ of the second pattern gives $B_g$, $B$ can be calculated as

$$B = B_h - B_g$$

according to Scherrer[5], if the peak has Lorentzian shape:

$$f(\nu) = \frac{C_0}{1 + \dfrac{4(\nu - \nu_k)^2}{B_k^2}}$$

where $C_0$ is a constant, $B_k$ is the FWHM of a peak at position $\nu_k$. Alternatively, $B$ can be calculated as

$$B^2 = B_h^2 - B_g^2$$

according to Warren[8],[9], if the peak has Gaussian shape:

$$f(\nu) = \exp\left(-C_1 \frac{(\nu - \nu_k)^2}{B_k^2}\right)$$

where $C_1$ is a constant, $B_k$ is the FWHM of a peak at position $\nu_k$.

However, the peaks produced by a particular instrument are usually between Lorentzian and Gaussian in nature, and the FWHM of the profiles in the recorded raw X-ray diffraction patterns are also sometimes hard to determine due to the existing background intensity and the noise associated with it, due to peak overlap, etc.

## Rietveld Refinement for the Determination of $B_h$ and $B_g$

Rietveld refinement is one of the most popular techniques nowadays in X-ray powder diffraction analysis. It provides a scheme to determine the FWHM of the peak in the pattern via optimally fitting the recorded pattern with a peak which is theoretically generated by a certain type of function (e.g., Gaussian, Lorentzian, Pseudo Voigt or Pearson VII, etc.) and generated according to the given compositional and structural information (i.e., chemical species, cell parameters, space group and atomic positions, etc.). In practice, it calculates the theoretical intensity at the $j^{th}$ data point as

$$Y_{c_j} = \sum_p A_p \sum_k L_k |F_k|^2 \, \Phi(2\theta_j - 2\theta_k) \, P_k + BK_j$$

where $A_p$ is a scale factor for the $p^{th}$ phase; $L_k$ contains correction factors such as Lorentz, polarization, multiplicity and absorption factors; $\Phi$ is the reflection profile function; $F_k$ is the structure factor for the $k^{th}$ reflection; $P_k$ is the preferred orientation function; and $BK_j$ is the background intensity at $j^{th}$ data point. The summations are over all the phases and reflections.

The calculated intensity $Y_{cj}$ undergoes least squares refinement with respect to all the parameters to best fit the observed intensity $Y_{oj}$ when the normal equation

$$A\, d = g$$

is solved for the parameter shifts $d$; where $A$ and $g$ are the matrices with elements

$$a_{ij} = \sum \omega \frac{\partial Y_c}{\partial P_i} \frac{\partial Y_c}{\partial P_j}$$

and

$$g_i = \sum (Y_o - Y_c) \frac{\partial Y_c}{\partial P_i}$$

Then the FWHM of the theoretically generated peak above the theoretically generated background is taken as the FWHM of the recorded peak. Hence $B_h$ and $B_g$ can be determined by running the respective Rietveld refinements.

However, two problems remain:

a) The recorded peak may not necessarily be fit very well by the reflection profile function chosen during the Reitveld refinement. In practice, a refinement residual always exists, having a value of 4 - 5% at its best; and such a refinement may not be very sensitive to types of peak function assumed.

b) The formula $B^2 = B_h^2 - B_g^2$ for the $B$ used in Scherrer's equation is true only when the corresponding peaks are of Gaussian nature, and $B = B_h - B_g$ is true only when the corresponding peaks are of Lorentzian nature. For other peak function types, no clear relation exists.

## Rietveld Refinement of the Standard and the Ribbon Samples

X-ray diffraction data of the "standard" sample and the ribbon sample were obtained using a Philips 1729 X-ray diffractometer at a power level of 20 mA × 40 kV, using Cu K$\alpha$ radiation with scanning step size of 0.02°, 20 seconds per scan step interval, and over a 2$\theta$ range of 20° - 80°.

The Rietveld program DBW3 . 2S[10] was used to perform the refinements. Whole pattern refinements were used. Fig. I .5 and Fig. I .6 show the recorded pattern (red dots), the theoretically generated profile (green solid line), the difference between them (yellow), and the peak positions of the generated profile (purple), for the standard and the ribbon, respectively. The residual factors for the standard sample were $\mathbf{R_p} = 5.26\%$ and $\mathbf{R_{wp}} = 7.18\%$, those for the ribbon sample were $\mathbf{R_p} = 3.85\%$ and $\mathbf{R_{wp}} = 5.15\%$. where the pattern R-factor is defined as

$$R_p = \frac{\sum |Y_i - Y_{c_i}|}{\sum |Y_i|}$$

and the weighted pattern R-factor as

$$R_{wp} = \frac{\sum w_i (Y_i - Y_{c_i})^2}{\sum w_i Y_i^2}$$

The program DBW3.2S was originally written for IBM computers, and after it was transplanted onto our VAX system, only the Pearson VII profile function was implemented for the generation of the theoretical patterns, as this function appeared to provide the best fit. This function is different from either a Gaussian or a Lorentzian function.

Fig. I .5 Plotting of Rietveld Refinement Result on the Standard Sample.

Red dots represent experimental data, green line represents the calculated pattern, yellow line represents the difference between the experimental data and the calculated, blue line is the zero point of the background, the small purple ticks right above the $2\theta$ abscissa are the calculated $K\alpha_1$ and $K\alpha_2$ peak positions.

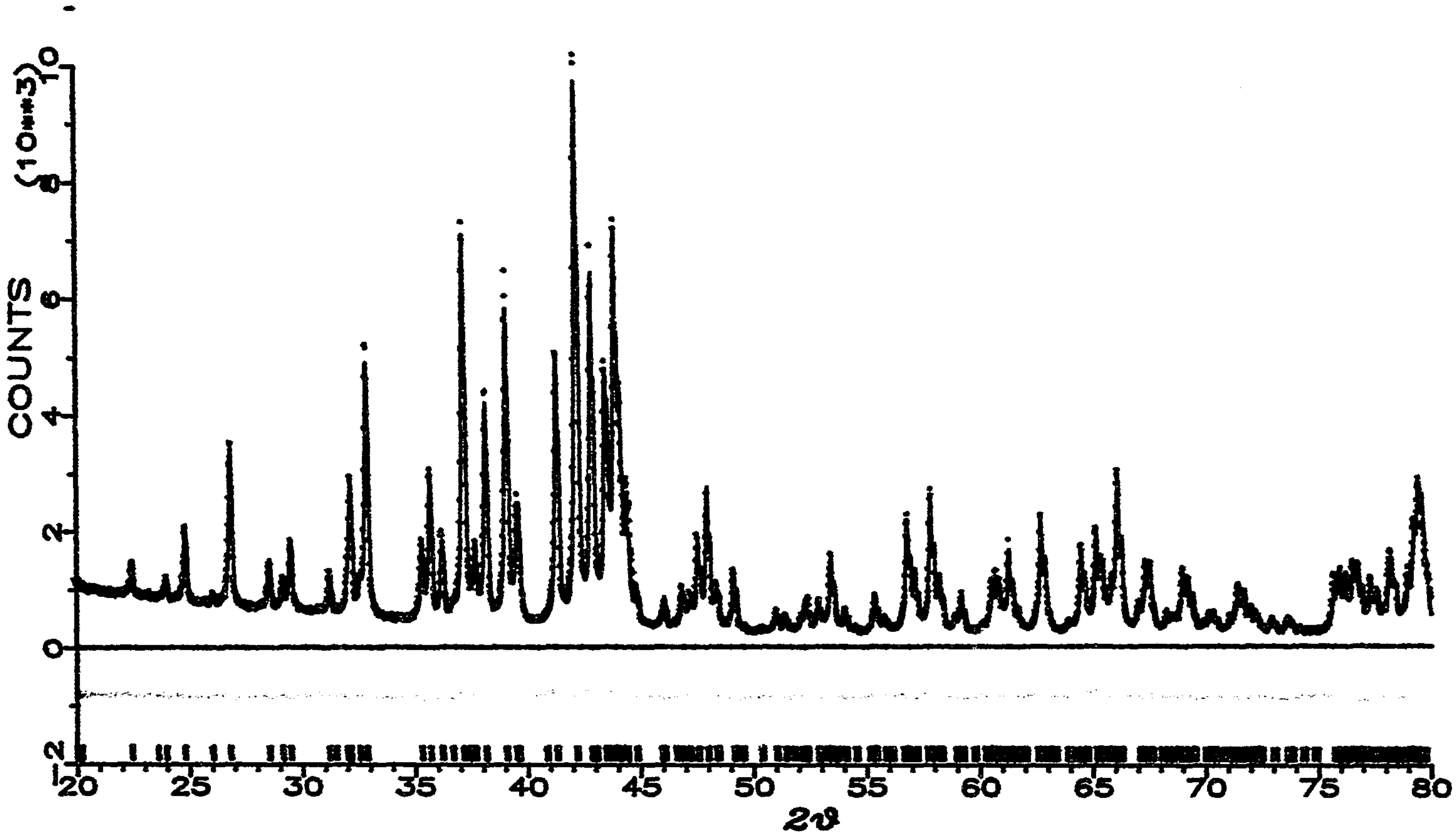
COUNTS
(10**3)
10
8
6
4
2
0
2
20
25
30
35
40
45
50
55
60
65
70
75
80
2θ

Fig. I.6 Plotting of Rietveld Refinement Result on the Ribbon Sample.

Red dots represent experimental data, green line represents the calculated pattern, yellow line represents the difference between the experimental data and the calculated, blue line is the zero point of the background, the small purple ticks right above the $2\theta$ abscissa are the calculated $K\alpha_1$ and $K\alpha_2$ peak positions.

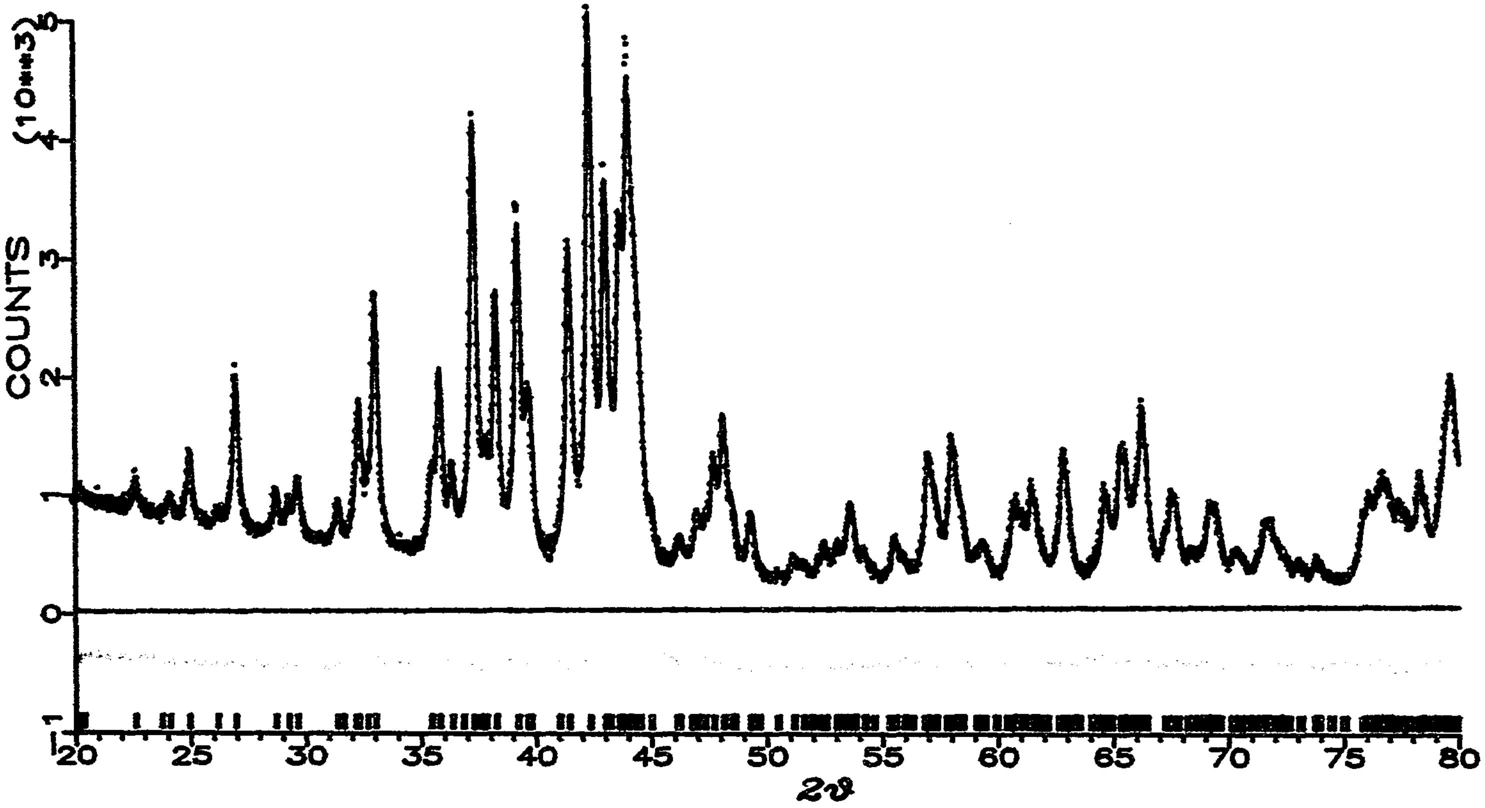
COUNTS
(10**3)
0
1
2
3
4
5
20
25
30
35
40
45
50
55
60
65
70
75
80
2ϑ

Since the samples were stress free, and some authors[11] claim that the peak shape due to a pure grain size effect should be of Gaussian nature, the formula $B^2 = B_h^2 - B_g^2$ was used to calculate $B$, which was then used to calculate the grain size of the ribbon using Scherrer's formula.

Peaks having their peak heights above the backgrounds by greater than ~ 1 × $10^3$ count in the ribbon pattern and ~ 2 × $10^3$ count in the standard pattern were chosen to obtain the FWHM's of them, namely the $B_h$'s and the $B_g$'s respectively, for the calculation of "the pure peak broadening", the $B$'s. The results of the grain size calculation are listed in Table I .1

It was found that the grain sizes thus calculated had a tendency to decrease while the peak position angles increased. This was most probably due to the peak shapes of the patterns in question being different form those of Gaussian peaks. Because of this result, we decided to try a different approach, an approach that employs a Fourier deconvolution technique, for grain size analysis.

Table I .1 Grain Size Determination for $Nd_2Fe_{14}B$ Ribbon by Rietveld Refinement

| Two theta (degree) | Peak Broadening (degree) | Grain Size (Angstrom) |
|---|---|---|
| 26.92 | 0.206 | 390.8 |
| 32.25 | 0.215 | 379.5 |
| 32.96 | 0.216 | 378.1 |
| 35.78 | 0.220 | 373.1 |
| 37.25 | 0.223 | 370.7 |
| 38.23 | 0.224 | 369.2 |
| 39.17 | 0.226 | 367.8 |
| 39.63 | 0.226 | 367.1 |
| 41.40 | 0.229 | 364.6 |
| 42.28 | 0.230 | 363.4 |
| 42.95 | 0.232 | 362.6 |
| 43.57 | 0.233 | 361.8 |
| 43.99 | 0.233 | 361.3 |
| 44.22 | 0.234 | 361.0 |
| 44.51 | 0.234 | 360.7 |
| 47.65 | 0.239 | 367.2 |
| 48.07 | 0.240 | 356.8 |
| 56.92 | 0.254 | 349.8 |
| 57.96 | 0.256 | 349.2 |
| 61.41 | 0.262 | 347.6 |
| 62.84 | 0.264 | 347.1 |
| 65.27 | 0.268 | 346.3 |
| 66.23 | 0.270 | 346.1 |
| 67.49 | 0.272 | 345.9 |
| 78.37 | 0.291 | 346.7 |
| 79.57 | 0.293 | 347.1 |
| 79.71 | 0.293 | 347.1 |
| | average | 359.9 |

# USE OF FOURIER DECONVOLUTION FOR THE DETERMINATION OF THE PURE DIFFRACTION BREADTH

According to the superposition theorem as presented by R. C. Spencer[12],[13], the profile of the observed peak, $h(\nu)$, is the convolution of the pure diffraction profile, $f(\nu)$, and the weight function of the apparatus, $g(\nu)$:

$$h(\nu) = \int_{-\infty}^{+\infty} g(\zeta) f(\nu - \zeta)\, d\zeta \tag{10}$$

In the present case, we can say that $h(\nu)$ is the profile of the peaks of the sample of interest, i.e., the sample of fine grain size; $g(\nu)$ is the profile of the peaks of the "standard sample", i.e., the sample of grain size > 1,000Å; and $f(\nu)$ is the profile of the peak which is responsible for the peak broadening due to the small grain size effect. Thus $h(\nu)$ is the "fold" of $g(\nu)$ and $f(\nu)$, and (10) can be written with equal validity as

$$h(\nu) = \int_{-\infty}^{+\infty} f(\zeta) g(\nu - \zeta)\, d\zeta \tag{11}$$

By using the Fourier transform method, the desired function $f(\nu)$ can be **deconvoluted** from the measurable functions $h(\nu)$ and $g(\nu)$.[14],[15],[16]

Let the functions be expanded into Fourier integrals:

$$
\begin{aligned}
f(\nu) &= \frac{1}{\sqrt{2\pi}}\int_{-\infty}^{+\infty} F(\zeta)\,e^{-2\pi i\nu\zeta}\,d\zeta \\
g(\nu) &= \frac{1}{\sqrt{2\pi}}\int_{-\infty}^{+\infty} G(\zeta)\,e^{-2\pi i\nu\zeta}\,d\zeta \\
h(\nu) &= \frac{1}{\sqrt{2\pi}}\int_{-\infty}^{+\infty} H(\zeta)\,e^{-2\pi i\nu\zeta}\,d\zeta
\end{aligned}
\tag{12}
$$

where the Fourier coefficient $F$ is the Fourier transform of $f$, $G$ of $g$, and $H$ of $h$ respectively, and have the forms

$$
\begin{aligned}
F(\zeta) &= \frac{1}{\sqrt{2\pi}}\int_{-\infty}^{+\infty} f(\nu)\,e^{2\pi i\nu\zeta}\,d\nu \\
G(\zeta) &= \frac{1}{\sqrt{2\pi}}\int_{-\infty}^{+\infty} g(\nu)\,e^{2\pi i\nu\zeta}\,d\nu \\
H(\zeta) &= \frac{1}{\sqrt{2\pi}}\int_{-\infty}^{+\infty} h(\nu)\,e^{2\pi i\nu\zeta}\,d\nu
\end{aligned}
\tag{13}
$$

The relevant theorem in Fourier transform shows that

$$H(\zeta) = G(\zeta)\cdot F(\zeta)$$

and therefore

$$F(\zeta) = \frac{H(\zeta)}{G(\zeta)} \tag{14}$$

The first equation of equation set (12) can now be written as

$$f(\nu) = \frac{1}{\sqrt{2\pi}}\int_{-\infty}^{+\infty} \frac{H(\zeta)}{G(\zeta)}\,e^{-2\pi i\nu\zeta}\,d\zeta \tag{15}$$

which is the profile of the desired "pure" peak exhibiting the peak broadening due to the small grain size effect.

In the present work, a fast Fourier transform (FFT) technique[17] has been employed in a deconvolution computer program for grain size determination. The profiles recorded experimentally are discrete data points. Thus, in practice the integrations for both forward and backward Fourier transform are changed to summations; the integral elements $d\nu$ and $d\zeta$ to $\Delta\nu$ and $\Delta\zeta$, with $\Delta$ being the step size of the recorded pattern; and the integral limits $\pm\infty$ to finite numbers $\pm N$. $N$ is required by the FFT technique to be a power of 2, i.e., $2^{m}$, and ideally $2^{m}-1 < N_p < 2^{m}$, where $N_p$ is the number of data points involved in the Fourier transform. Equations (13) and (15) become

$$
\begin{aligned}
F(\zeta) &= \frac{1}{\sqrt{2\pi}} \sum_{-N}^{+N} f(\nu)\, e^{\frac{2\pi i\nu\zeta}{2N+1}} \Delta\nu \\
G(\zeta) &= \frac{1}{\sqrt{2\pi}} \sum_{-N}^{+N} g(\nu)\, e^{\frac{2\pi i\nu\zeta}{2N+1}} \Delta\nu \\
H(\zeta) &= \frac{1}{\sqrt{2\pi}} \sum_{-N}^{+N} h(\nu)\, e^{\frac{2\pi i\nu\zeta}{2N+1}} \Delta\nu
\end{aligned}
\tag{16}
$$

and

$$
f(\nu) = \frac{1}{\sqrt{2\pi}} \sum_{-N}^{+N} \frac{H(\zeta)}{(2N+1)\,G(\zeta)}\, e^{-\frac{2\pi i\nu\zeta}{2N+1}} \Delta\zeta \tag{17}
$$

However, a first attempt to simply employ the above formula in computerizing the problem resulted in an $f(\nu)$ that looked like that shown in Fig. I .7, no matter whether $h(\nu)$ and $g(\nu)$ were the whole patterns on Fig. I .5 and Fig. I .6, or isolated peaks, say those on ~ 27°, from these patterns. Problems were even found using a "very well behaved" Gaussian profiles (Fig. I.8 and Fig. I.9) generated by my own program.

The reason for the failure appears to be due to the noise and/or the discontinuities that have been introduced into the recorded or the theoretically generated patterns. For example, in the "ideal" Gaussian cases, $h(\nu)$ and $g(\nu)$ vanish only at $+\infty$ or $-\infty$. The $h(\nu)$ and $g(\nu)$ profiles used in practice are truncated within a finite range. In carrying out the forward Fourier transformation to obtain the coefficients $H(\zeta)$ and $G(\zeta)$ according to (16), the non-zero background wings of the profiles $h(\nu)$ and $g(\nu)$ accumulate during the summation, making the background wings of $H(\zeta)$ and $G(\zeta)$ non-zero, although very small in value (Fig. I.10–I.11). When the deconvolution and the backward Fourier transformation proceed, according to (17), the small values in the background wings of $H(\zeta)$ and $G(\zeta)$ exaggerate the noise. That can be especially true when $G(\zeta)$ is very small, since it is in the denominator.

To alleviate this problem one can --

a) lessen the noise pertaining to the recorded $h(\nu)$ and $g(\nu)$ patterns. A least squares smoothing technique based on a seven-point-polynomial could be used to smooth the raw data, but since it takes the weighted average of the adjacent data values for an individual data point, it depresses and broadens the peaks; it is just the latter that is a main concern of this work. Instead, a least squares spline smoothing technique[18] was selected.

Figure I.7 A noisy pattern of the *f*(v) profile obtained in the deconvolution of *g*(v) profile from the *h*(v) profile.

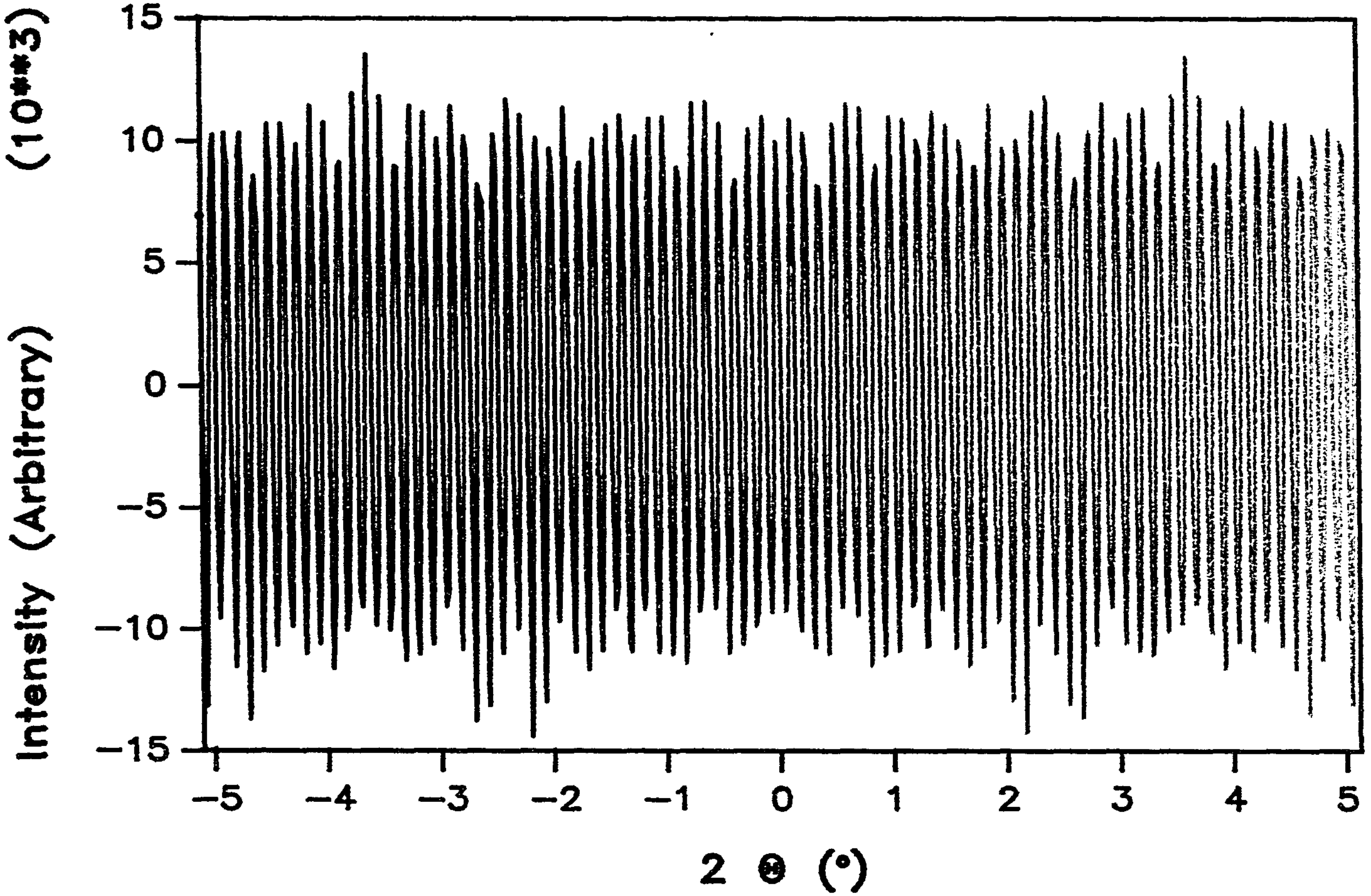

Figure I.8 A generated Gaussian *h*(ν) profile.

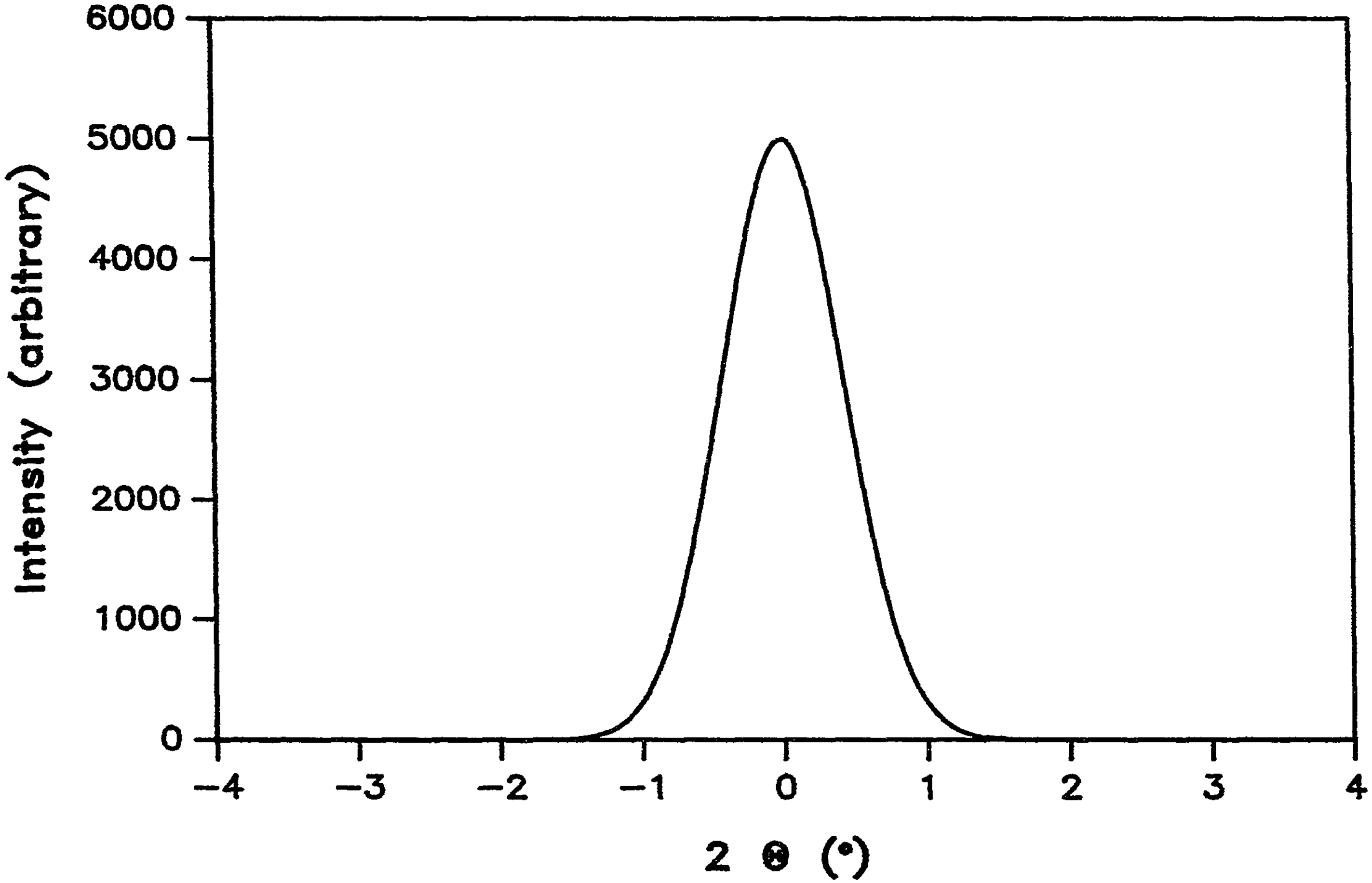

Figure I.9 A generated Gaussian $g(\nu)$ profile.

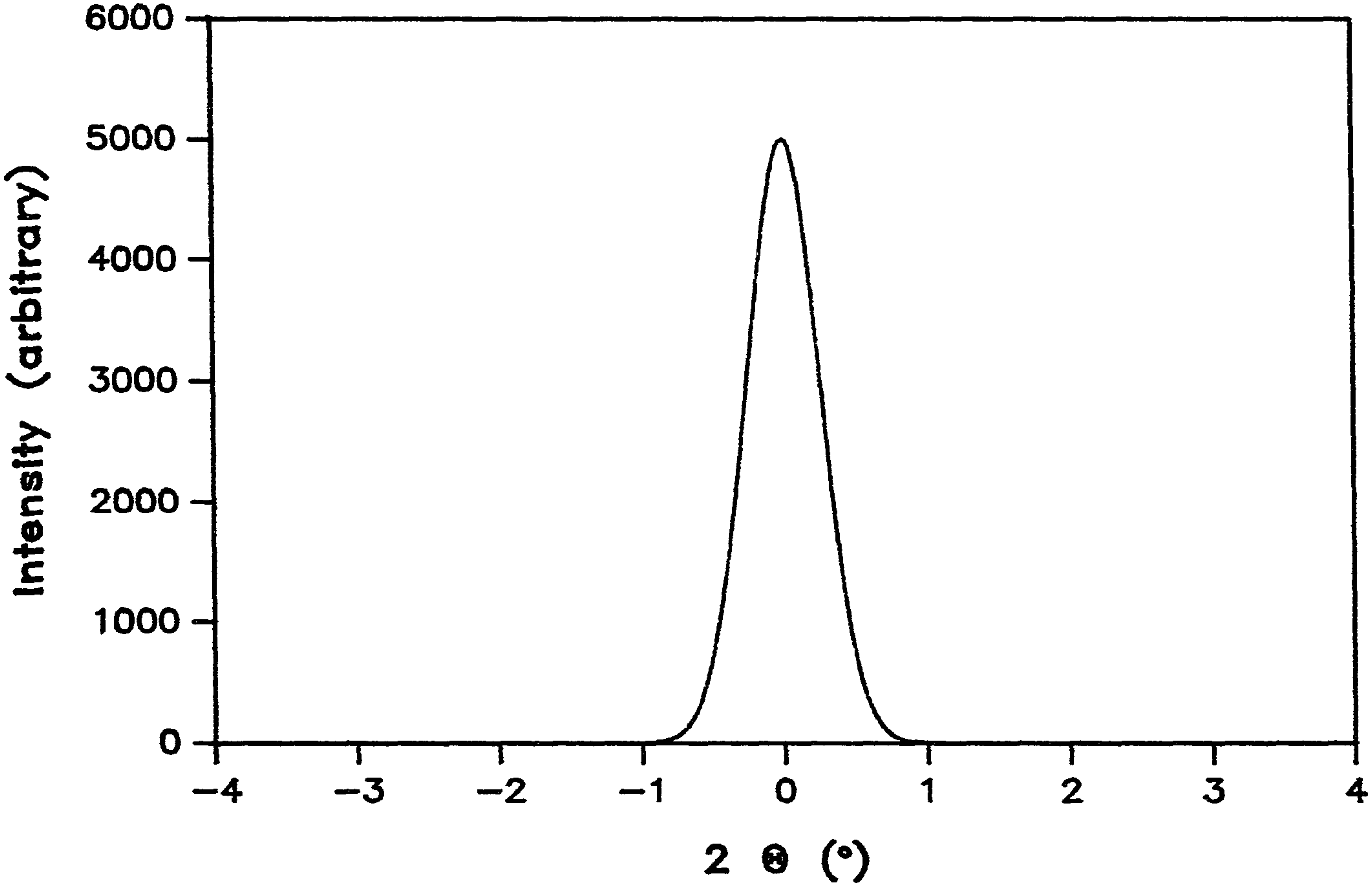

b) modify the results of the forward transform, $H(\zeta)$ and $G(\zeta)$ profiles, to minimize the accumulated noise on their background wings.

Figure I.10 A Fourier transformed Gaussian $|H(\zeta)|^2$ profile.

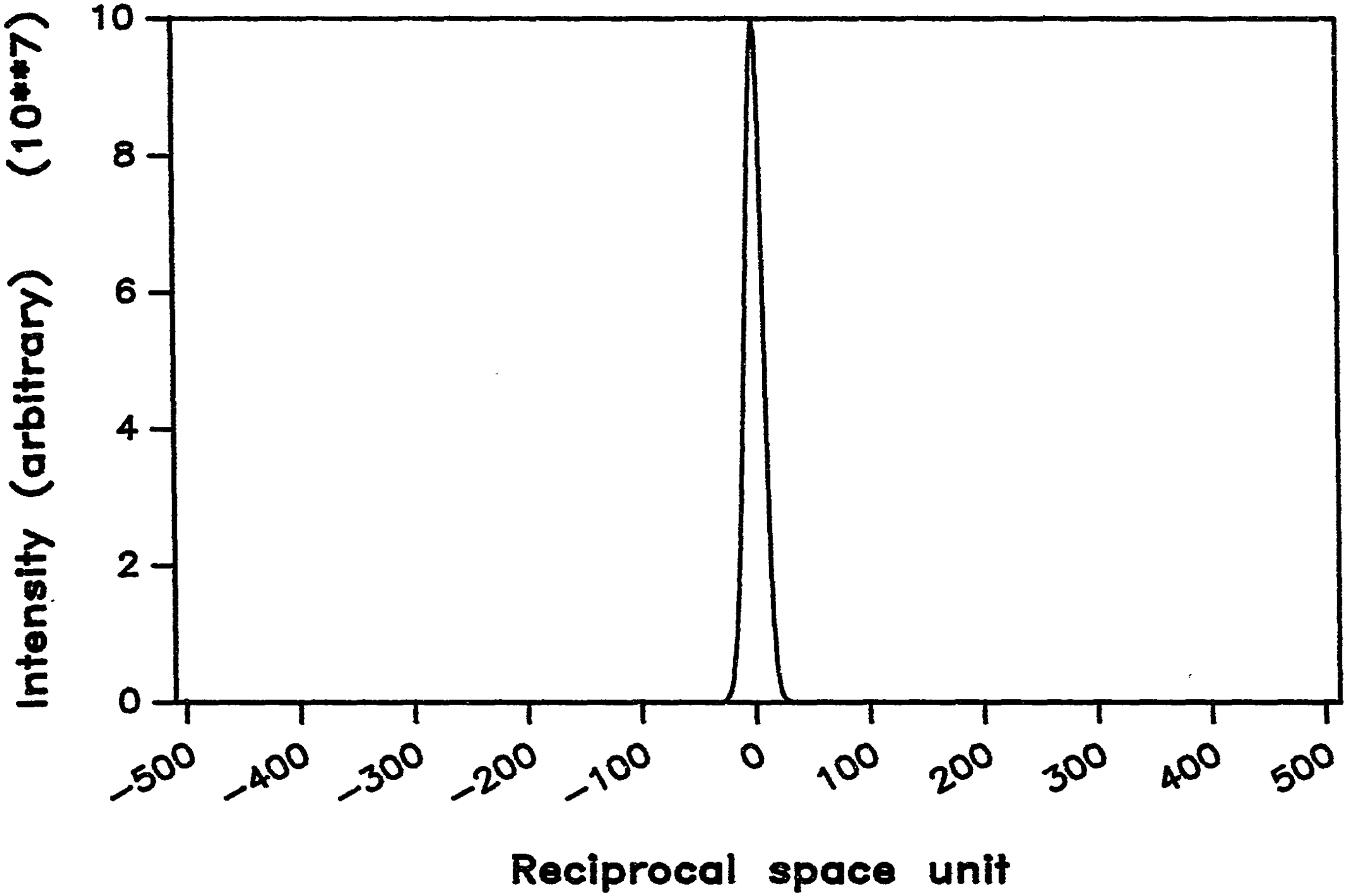

Figure I .10 (Continued) The Gaussian character of the $|H(\zeta)|^2$ profile is easier to see, after choosing a smaller range on the abscissa.

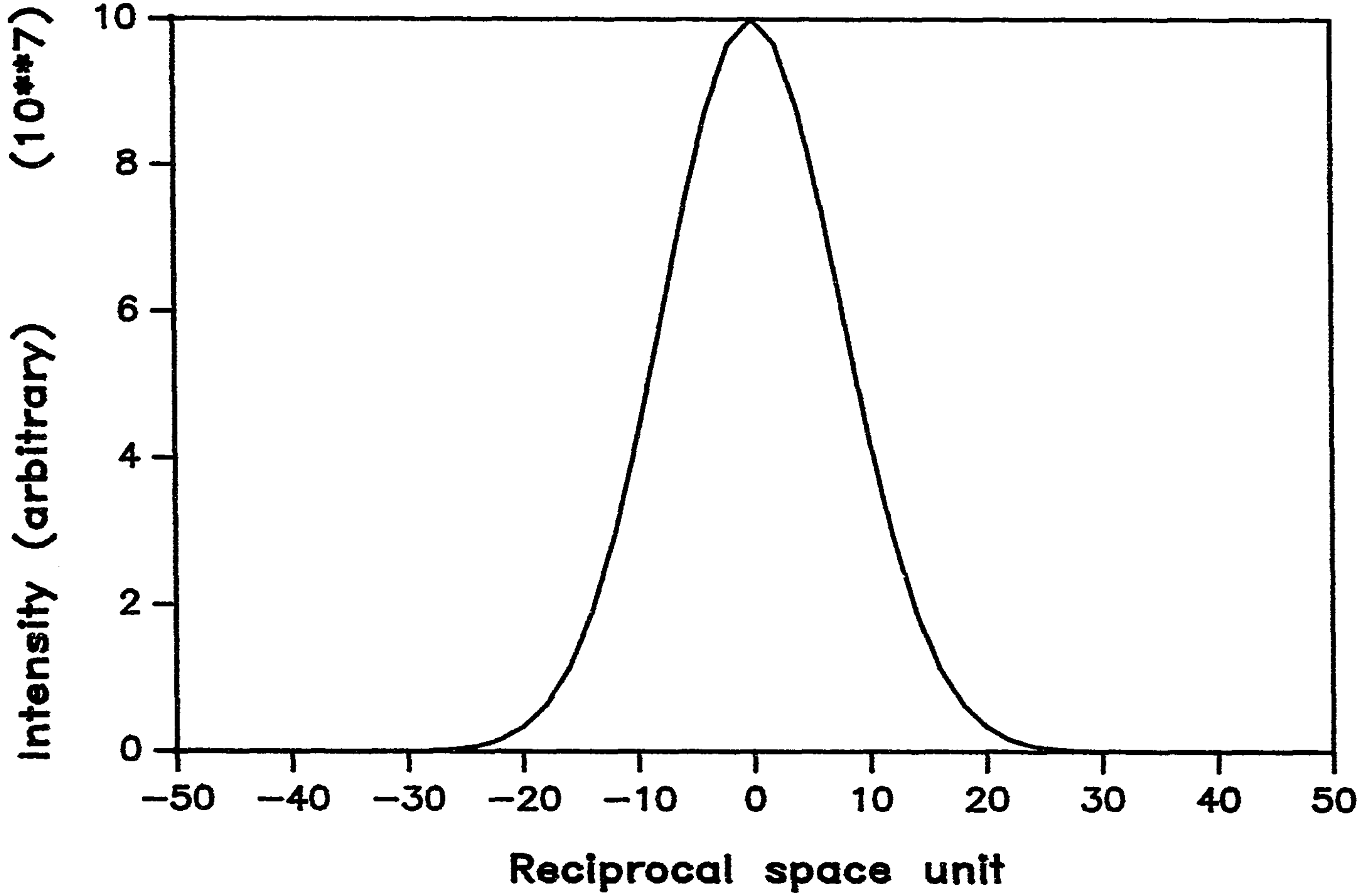

Figure I.10 (Continued) The noise associated with the $|H(\zeta)|^2$ profile when a smaller range is chosen for the ordinate.

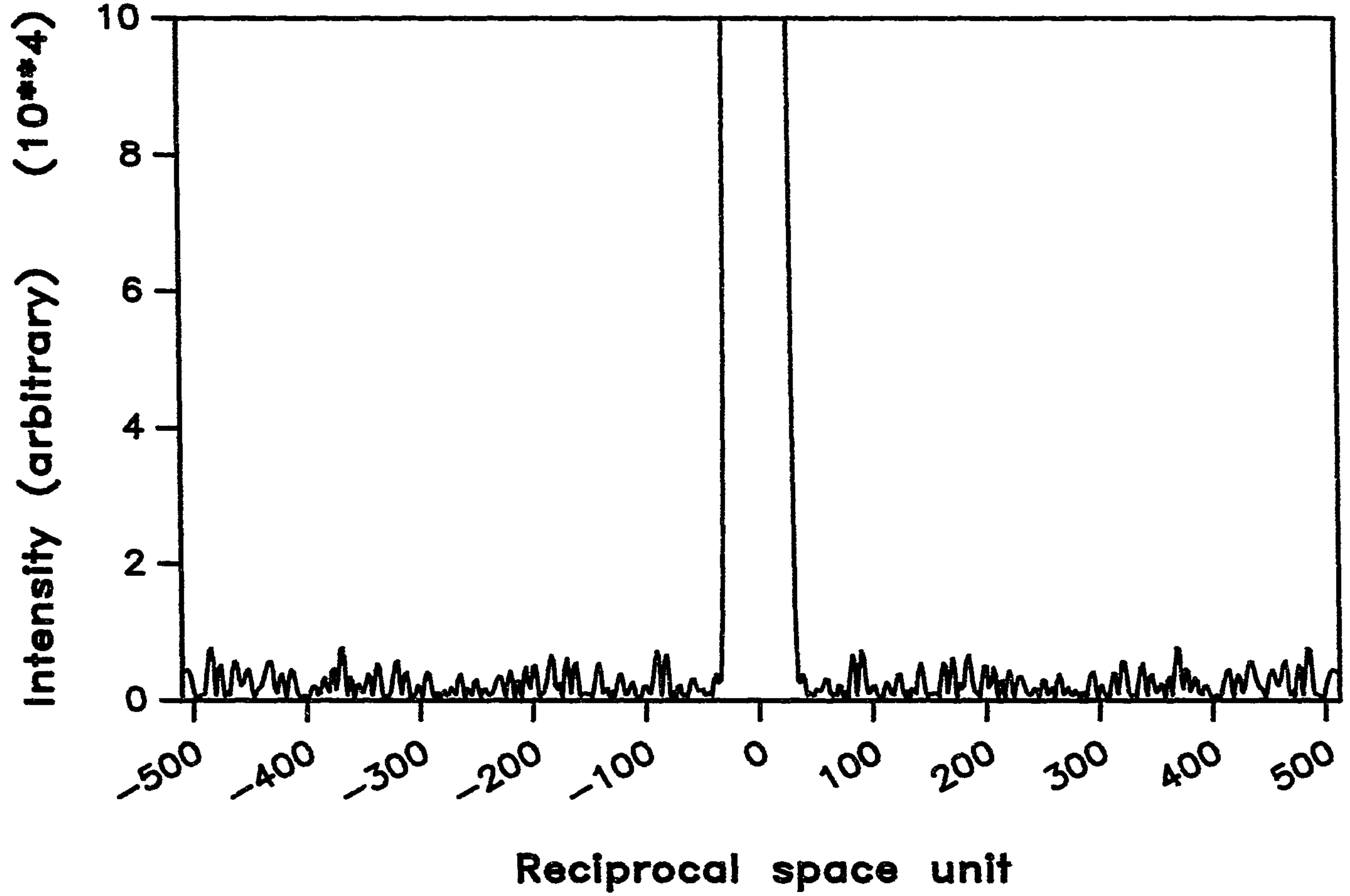

Figure I.11 A Fourier transformed Gaussian $|G(\zeta)|^2$ profile.

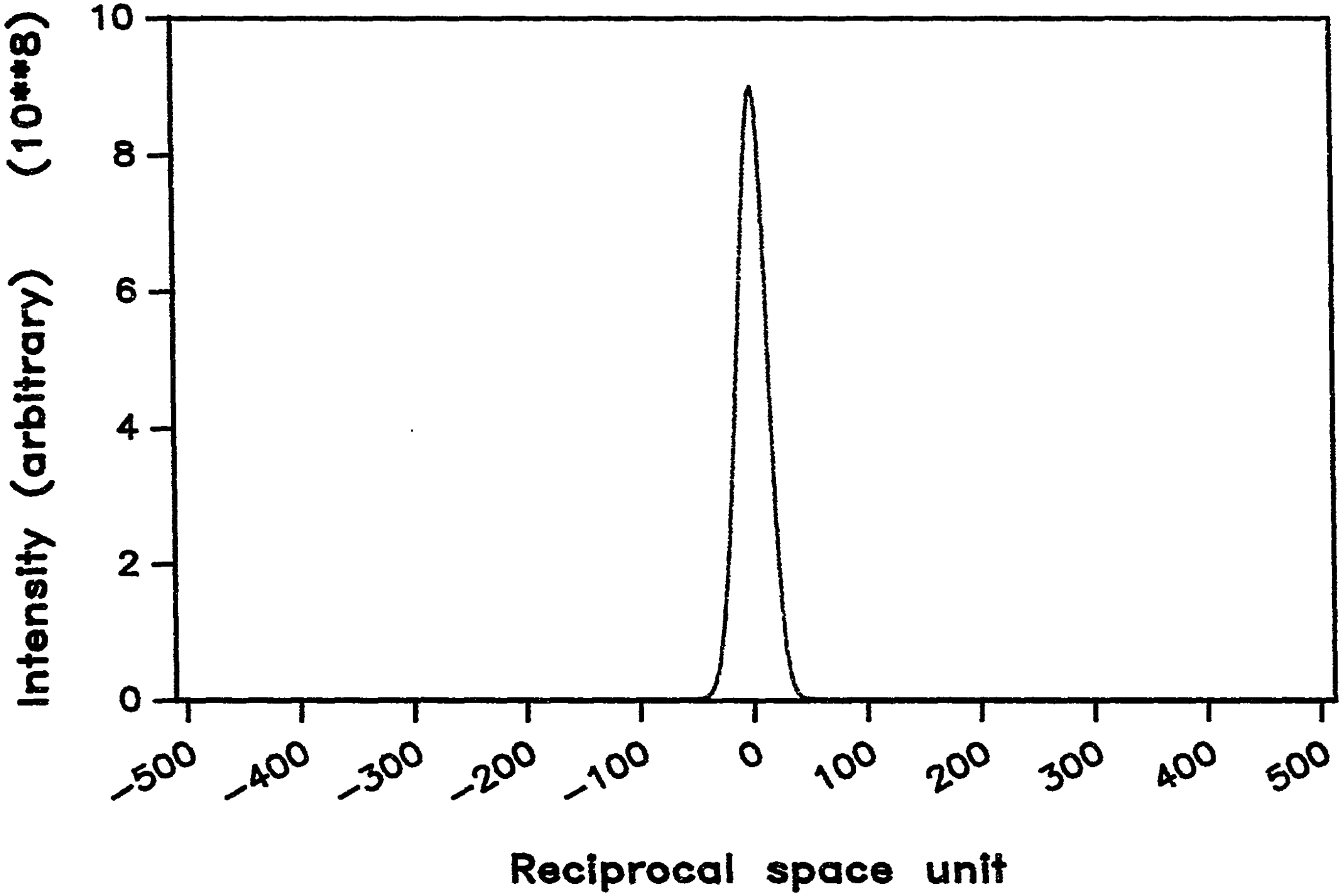

Figure I.11 (Continued) The Gaussian character of the $|G(\zeta)|^2$ profile is easier to see, after choosing a smaller range on the abscissa.

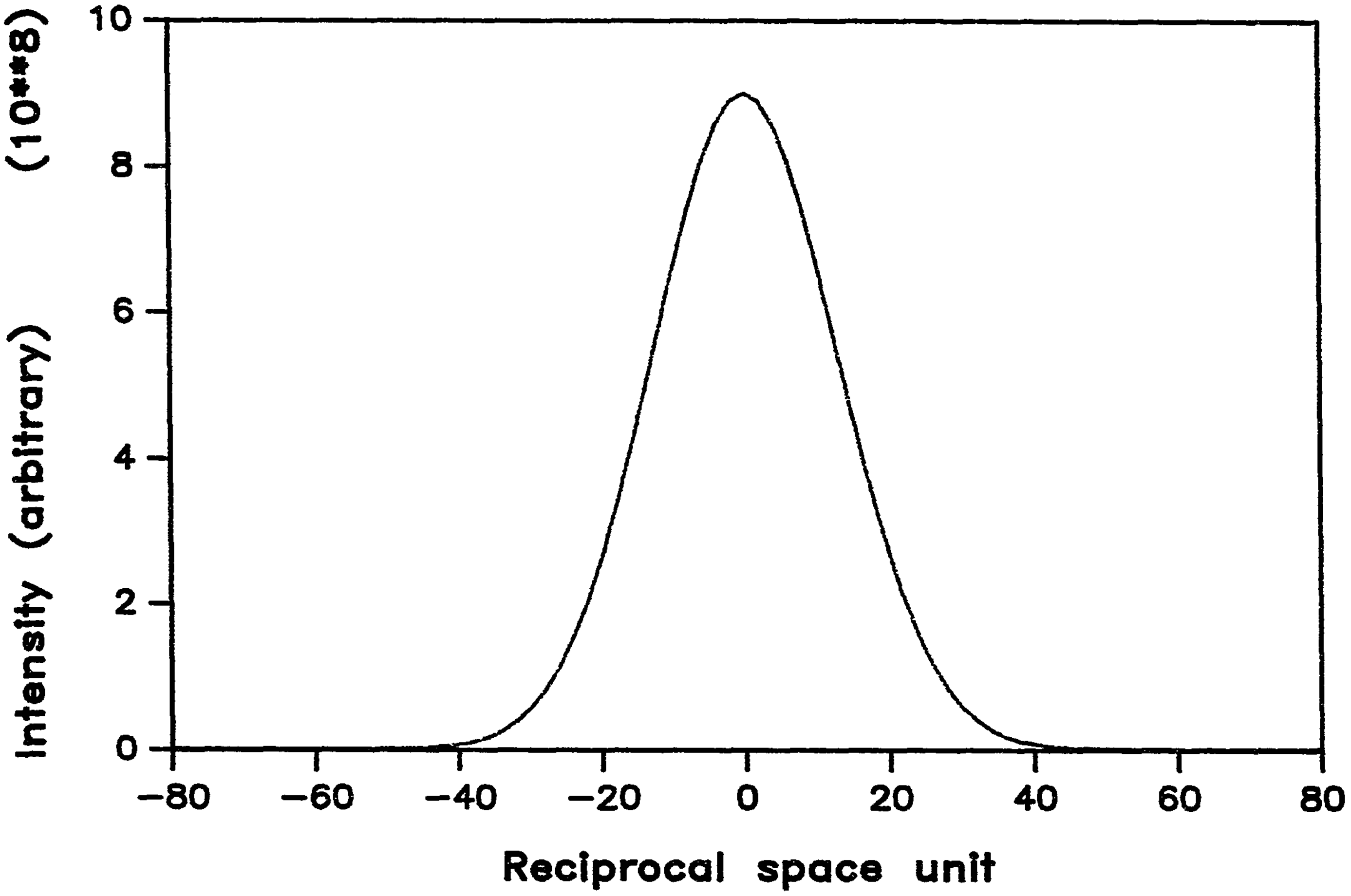

Figure I.11 (Continued) The noise associated with the $|G(\zeta)|^2$ profile when a smaller range is chosen for the ordinate.

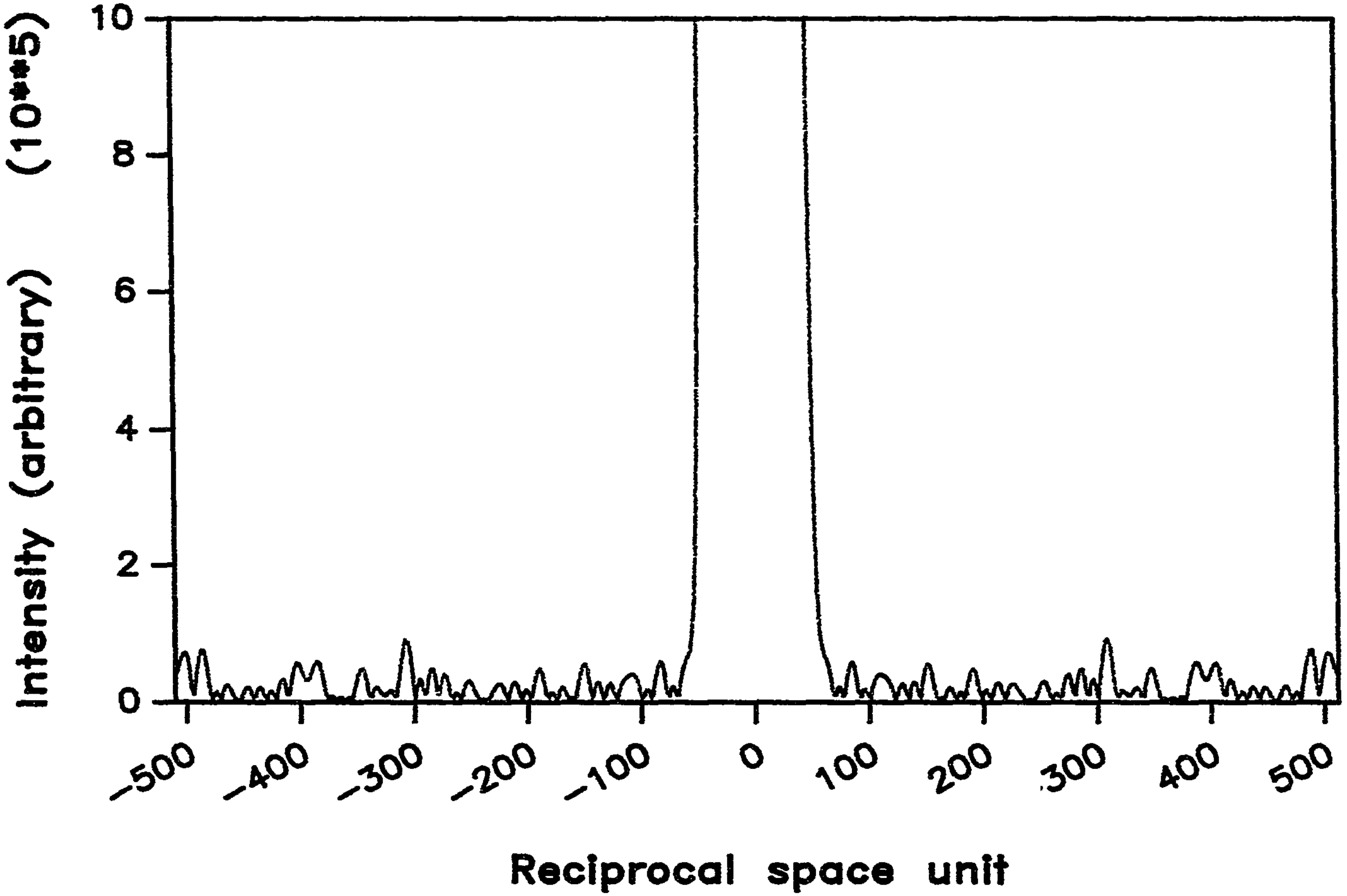

## Least Squares Spline Smoothing of the Recorded Patterns

In industry, in order to enlarge the designs of high speed airplanes or ship bodies with high precision, splines have been used to obtain smoothed curves. Splines are pieces of elastic, steel or soft wooden stripes that were put among the nails, which were located on the desired positions of the object material, such that the nails prevent the stripes stretching away from the nails; and the connections between two adjacent splines were realized by letting the splines share a common nail, and by the end segment adjacent to this common nail of the spline pressing the starting segment of the other spline against the nail (Fig. I .12). This would guarantee that the smoothness obtained is valid up to a continuous second derivative.

In the spline approximation, the function consisting of the data points is approximated by a set of polynomials, where each polynomial is determined by two consecutive data points which were chosen and designated as knots, and when two polynomials join at a common knot, not only are their functional values at this point equal, but also their first derivatives and the second derivatives at this point are respectively equal as well, in order that all the polynomials join smoothly.

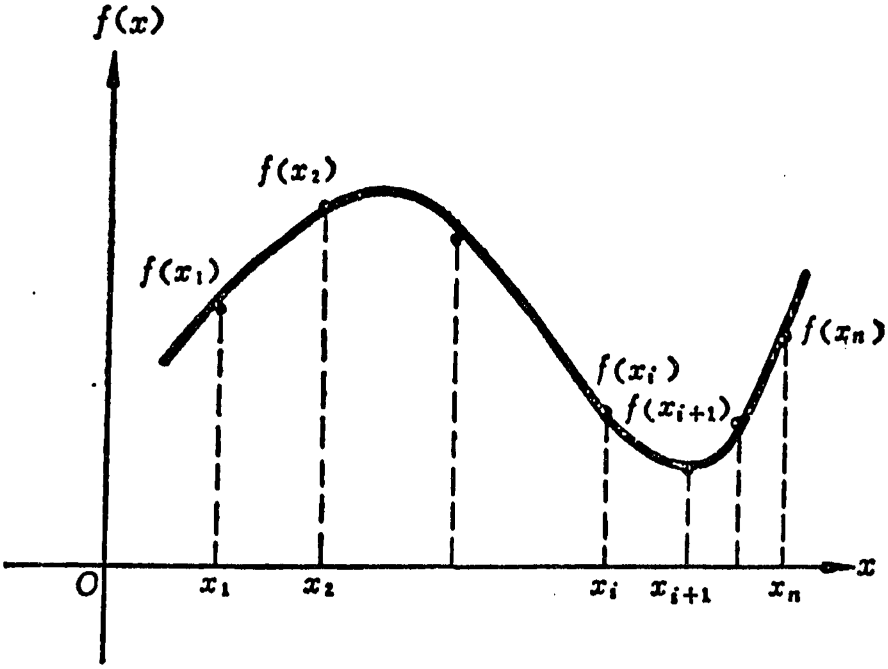

Fig. I. 12 Spline approximation of $f(x)$.

Spline materials (thick curve) are positioned among the nails (solid circles), which are designated as **knots**. Cubic spline approximation is to determine in $[x_i, x_{i+1}]$ a polynomial $P_i(x)$ to the power of 3, based on the values $x_{i-1}$, $x_i$, $x_{i+1}$, $f(x_{i-1})$, $f(x_i)$, and $f(x_{i+1})$.

Referring to Fig. I .12, for knots $x_1, x_2, \ldots, x_n$ with data values $f(x_1)$, $f(x_2), \ldots, f(x_n)$, there are $n-1$ corresponding polynomials $P_1(x), P_2(x), \ldots, P_{n-1}(x)$ to be determined with the following conditions:

a) at each pair of knots, $x_i$ and $x_{i+1}$, the values of the corresponding polynomials $P_i(x_i)$ and $P_i(x_{i+1})$, equal the data values $f(x_1)$, and $f(x_2)$

$$\begin{aligned} P_i(x_i) &= f(x_i) \\ P_i(x_{i+1}) &= f(x_{i+1}) \end{aligned} \qquad i = 1, 2, \ldots, n-1$$

b) at each knot, the values of the first and second derivatives of the polynomials sharing the same knot must be equal respectively

$$\begin{aligned} P_i'(x_i) &= P_{i-1}'(x_i) \\ P_i''(x_i) &= P_{i-1}''(x_i) \end{aligned} \qquad i = 2, 3, \ldots, n-1$$

c) at both end knots, the splines are 'free'. Their curvatures are zero

$$P_1''(x_1) = 0$$

$$P_{n-1}''(x_n) = 0$$

According to the properties of the spline materials, each $P_i''(x)$ is a linear function of $x$. If one denotes

$$f_i \equiv f(x_i)$$

$$h_i \equiv x_{i+1} - x_i$$

$$\phi_i \equiv P''_{i-1}(x_i) = P''_i(x_i)$$

one can obtain the equation for $P_i''(x)$ in the interval $[x_i, x_{i+1}]$ using the values $\phi_i$ and $\phi_{i+1}$

$$P_i''(x) = \frac{x_{i+1} - x}{h_i}\phi_i + \frac{x - x_i}{h_i}\phi_{i+1}$$

therefore $P_i(x)$ can be obtained by simply integrating $P_i''(x)$ twice.

$$\begin{aligned} P_i(x) &= \frac{\phi_i}{6h_i}(x_{i+1} - x)^3 + \frac{\phi_{i+1}}{6h_i}(x - x_i)^3 \\ &+ \left(\frac{f_{i+1}}{h_i} - \frac{h_i\phi_{i+1}}{6}\right)(x - x_i) \\ &+ \left(\frac{f_i}{h_i} - \frac{h_i\phi_i}{6}\right)(x_{i+1} - x) \qquad i = 2,3 \ldots, n-1 \end{aligned}$$

where each $\phi_i$ can be obtained by differentiation of $P_i(x)$ above and using the condition $P_i'(x_i) = P_{i-1}'(x_i)$

$$\frac{h_{i-1}}{h_i}\phi_{i-1} + 2\left(1 + \frac{h_{i-1}}{h_i}\right) + \phi_{i+1}$$

$$= \frac{6}{h_i}\left(\frac{f_{i+1} - f_i}{h_i} - \frac{f_i - f_{i-1}}{h_{i-1}}\right)$$

$$i = 2, 3, \dots, n-1$$

while "end conditions" still hold, yielding $\phi_1 = \phi_n = 0$

Cubic least squares spline smoothing[18] is based on the above general spline approximation. First, the approximate data values for data points $x_1$, $x_2$, ..., $x_n$, were determined by the polynomial $P(x_i)$'s

$$f(x_i) = P(x_i) + \epsilon_i$$

then if an estimate $\delta f(x_i)$ of the variance in $f(x_i)$ is given, one can recover $P(x)$ from these data by constructing a function $g(\zeta)$, which minimizes

$$\xi \sum_{i=1}^{n} \left(\frac{f(x_i) - g(x_i)}{\delta f(x_i)}\right)^2 + (1-\xi)\int_{x_1}^{x_n} [g''(t)]^2 \, dt$$

over all $g(\xi)$ together with the three derivatives, where $\xi$ is within $[0, 1]$ and can be chosen according to the desire of the user regarding the closeness of the fit of the function to the given data and how smooth the function is to be.

Fig. I.13-I.17 show the raw peaks, picked out from different portion of the $h(\nu)$ and $g(\nu)$ patterns, and their least squares spline smoothing results.

Figure I.13 *h*(v) and *g*(v) patterns at ~27° of the samples, and their least squares spline smoothed results. The patterns have not been corrected for zero points.

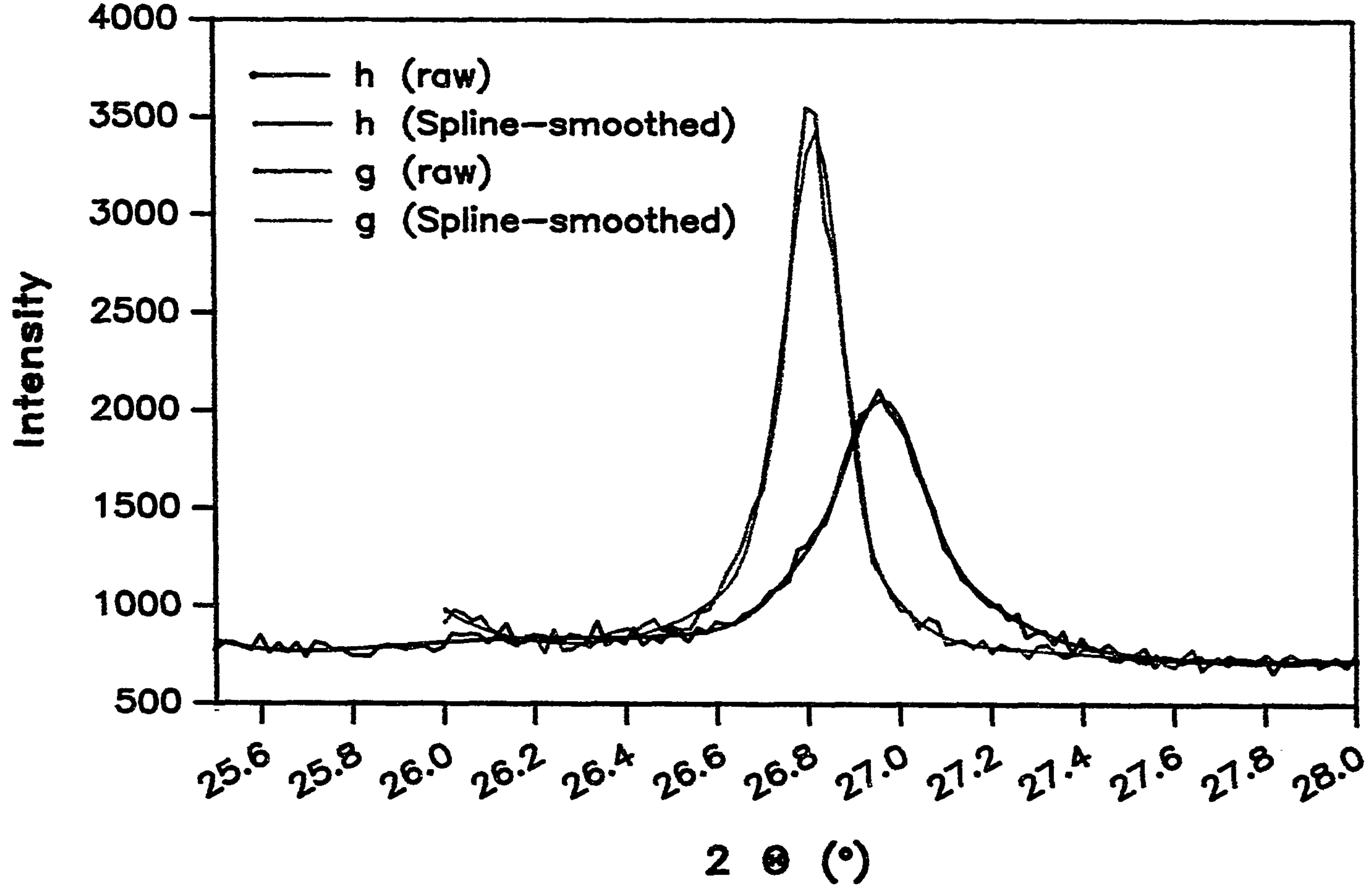

Figure I.14 Multiple peak $h(\nu)$ and $g(\nu)$ patterns at 35° - 40° range, and their least squares spline smoothed results. The patterns have not been corrected for zero points.

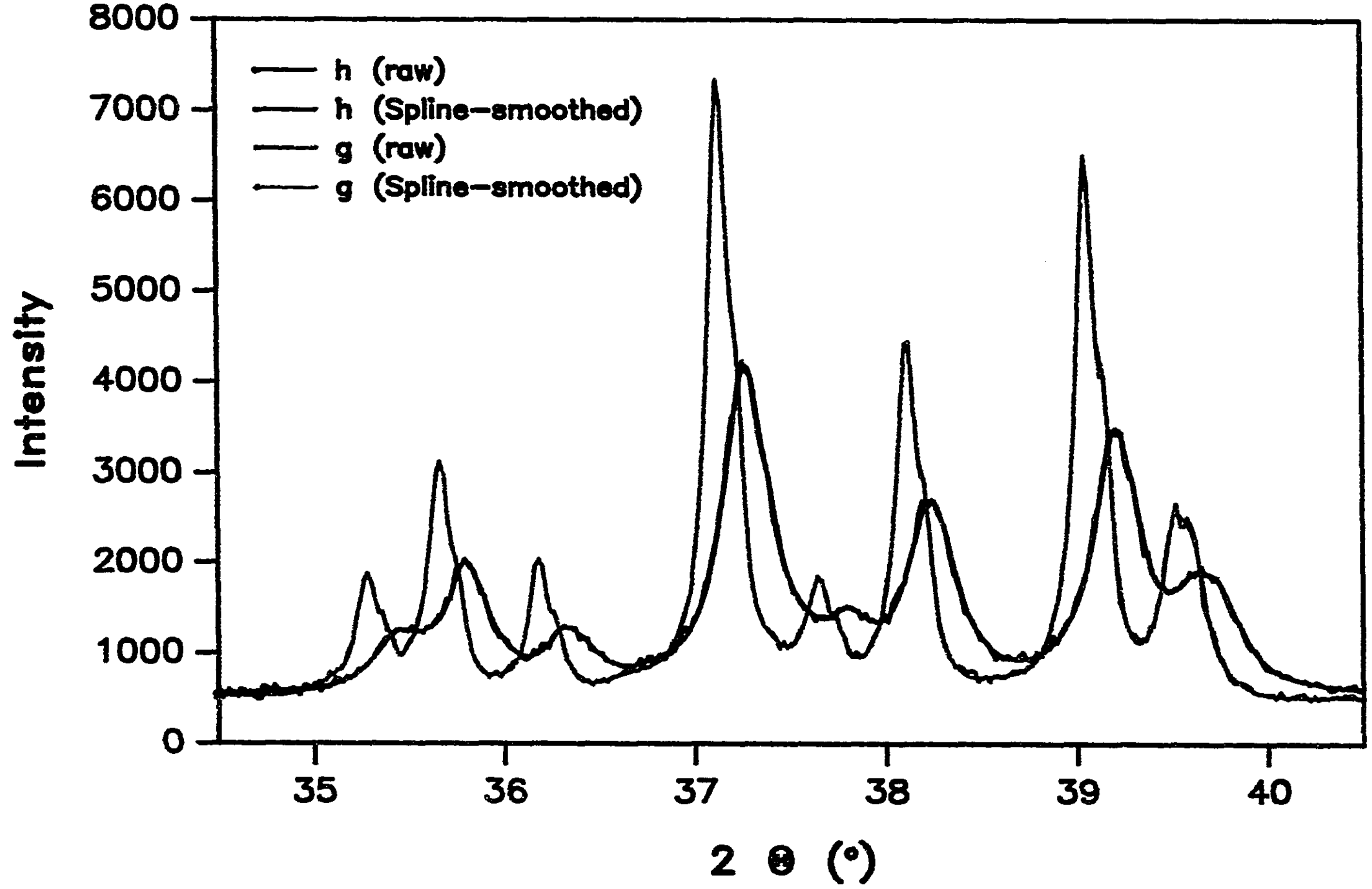

Figure I.15 Multiple peak $h(\nu)$ and $g(\nu)$ patterns at 41° - 45° range, and their least squares spline smoothed results. The patterns have not been corrected for zero points.

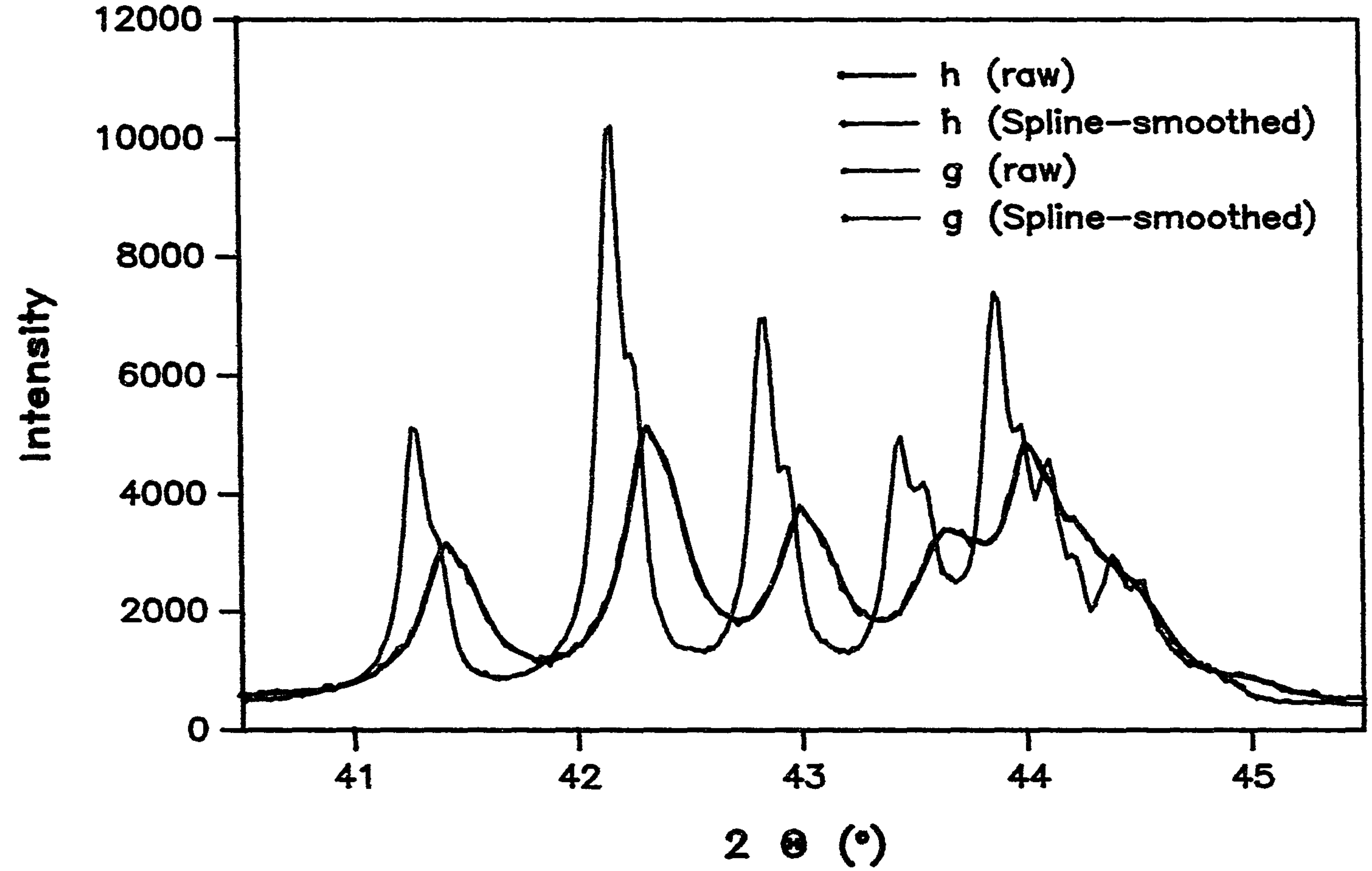

Figure I.16 Multiple peak *h*(v) and *g*(v) patterns at 55° - 60° range, and their least squares spline smoothed results. The patterns have not been corrected for zero points.

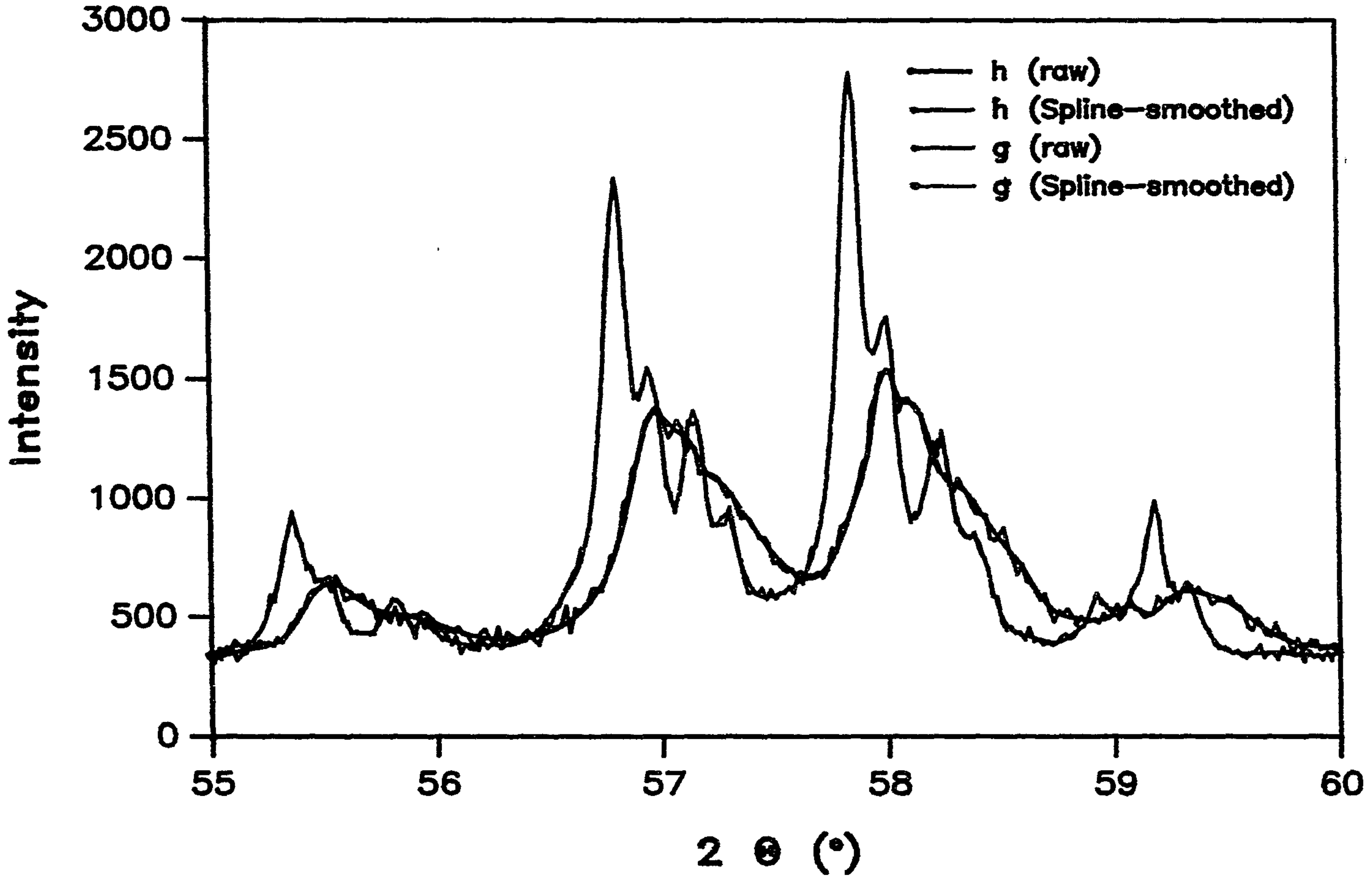

Figure I.17 $h(v)$ and $g(v)$ patterns at ~62° of the samples, and their least squares spline smoothed results. The patterns have not been corrected for zero points.

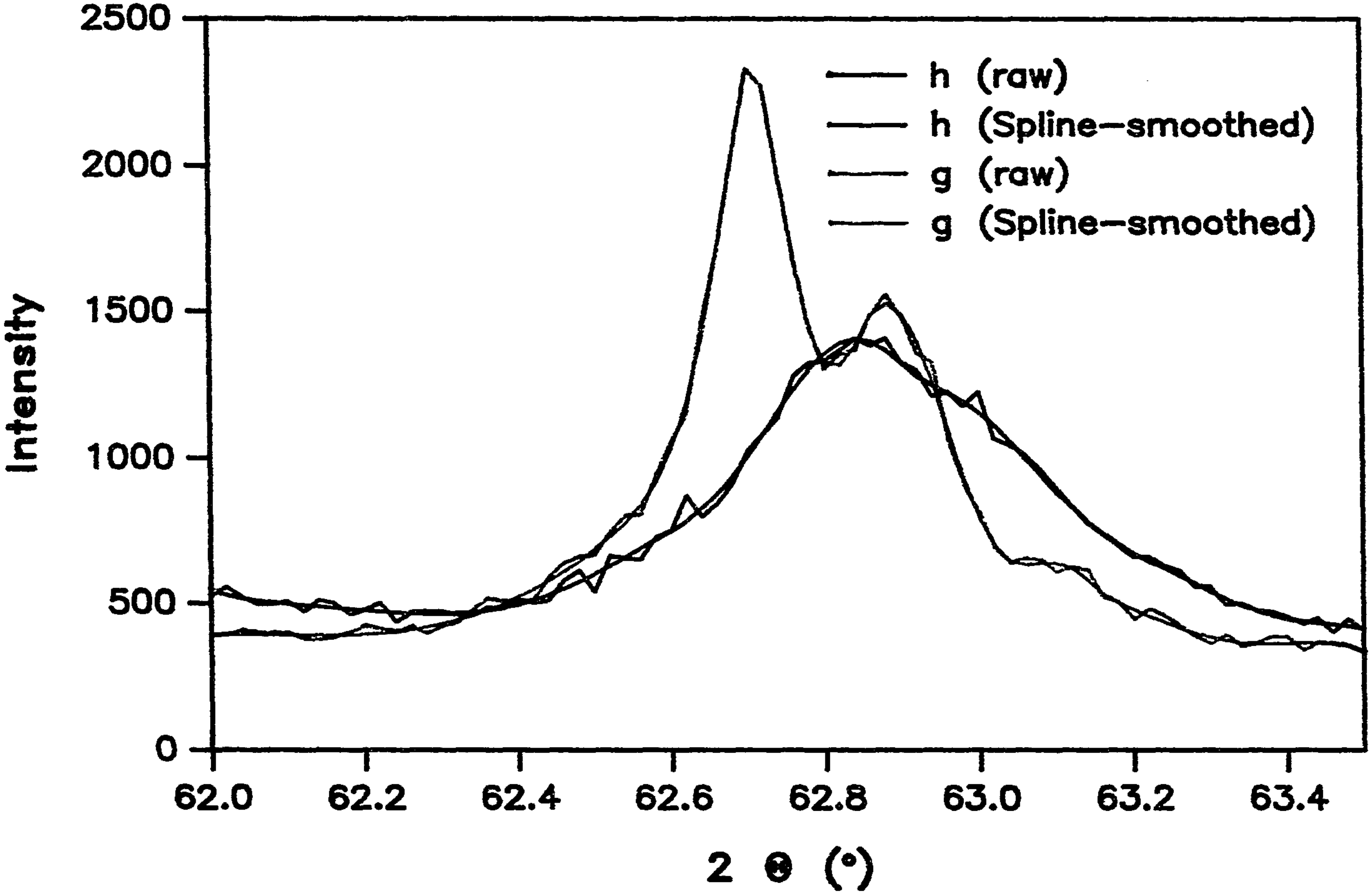

It should be mentioned that although least squares spline smoothing maintains the main features of the raw data profiles, choosing the individual data points as the knots to obtain a good smooth result is challenging and tedious work. I do wish I had a graphical editor to choose from raw data points shown on the screen via a mouse-like operation, to have all the points so chosen read as the knots into the least squares spline smoothing program, and have the result shown on the screen for inspection. This process could then be repeated until the best result has been found.

## Elimination of Accumulated Discontinuities of the Resulted Profiles after the Forward Transform

By close investigation of the failed backward Fourier transform of the deconvoluted $F(\zeta)$ of the "well behaved" Gaussian function, which resulted in an above mentioned "noise-like" pattern of $f(\nu)$, it was found that accumulated discontinuities played an important role.

This is seen in Fig. I .18a-I .18c where the Gaussian $|F(\zeta)|^2$ is plotted. Since $F(\zeta)$ as calculated by (14) is a complex function, the modulus is more readily plotted and examined:

$$|F(\zeta)|^2 = F_r^2(\zeta) + F_i^2(\zeta)$$

where, using

$$H(\zeta) = H_r(\zeta) + iH_i(\zeta)$$

$$G(\zeta) = G_r(\zeta) + iG_i(\zeta)$$

and thus, according to (14)

$$F(\zeta) = \frac{H_r + iH_i}{G_r + iG_i}$$

$$= \frac{(H_r + iH_i)(G_r - iG_i)}{G_r^2 + G_i^2}$$

such that the real and the imaginary components of $F(\zeta)$ are

$$F_r = \frac{H_r G_r + H_i G_i}{G_r^2 + G_i^2}$$

and

$$F_i = \frac{H_i G_r - H_r G_i}{G_r^2 + G_i^2}$$

In Fig. I .18a, $|F(\zeta)|^2$ should maintain the Gaussian feature. However, the discontinuities accumulated on the wings of $H(\zeta)$ and $G(\zeta)$ make the noise on the wings of $F(\zeta)$ so high that the main peak, which is located between *ca.* - 35 and + 35 reciprocal space units, has low intensity compared to the two noise peaks at - 170 and + 170, and thus almost can not be seen.

Figure I.18 A Gaussian $|F(\zeta)|^2$ profile obtained according to equation (14). The noise associated with the Gaussian $H(\zeta)$ and $G(\zeta)$ profile make the main peak almost invisible.

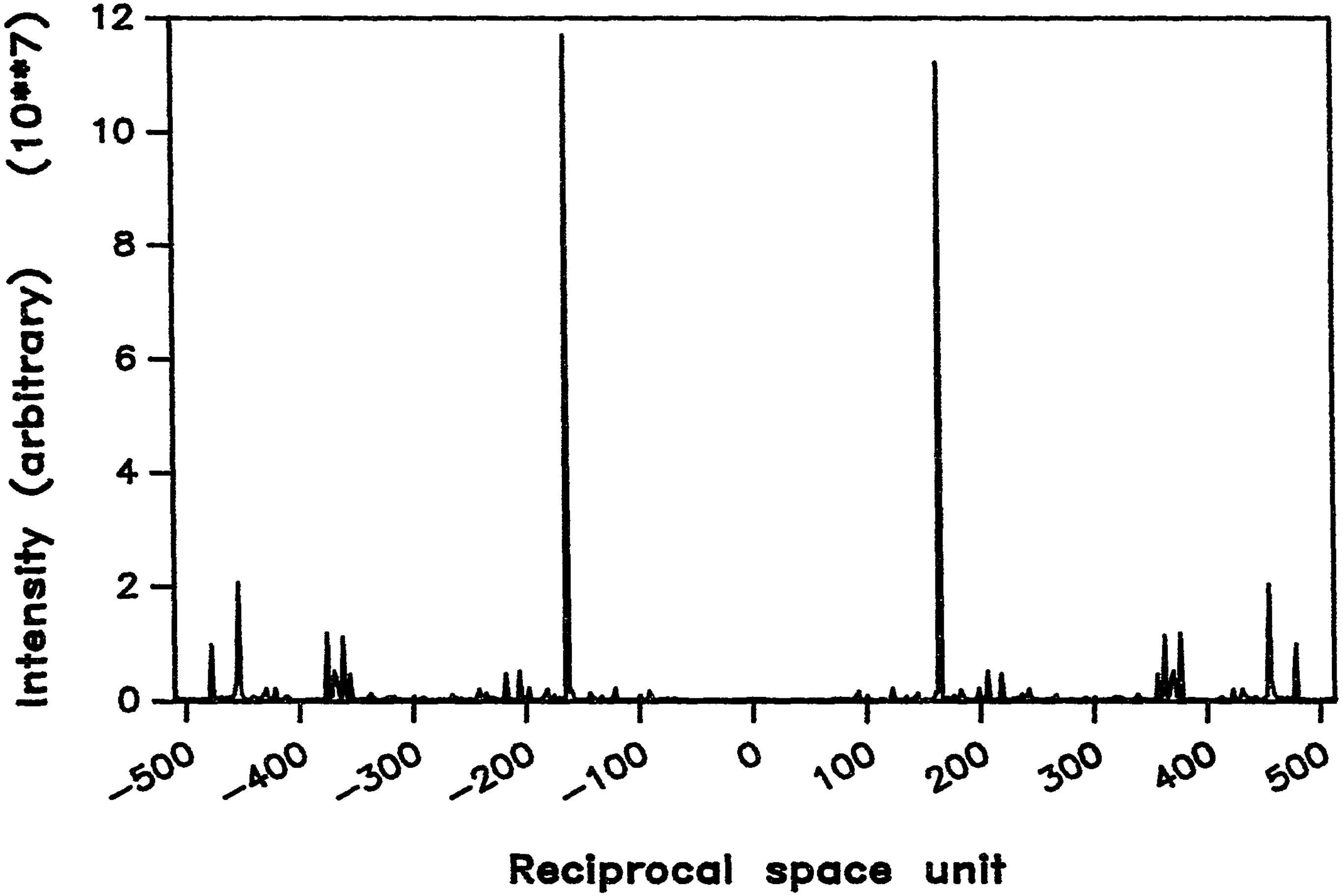

Figure I.18 (Continued) The main peak of the $|F(\zeta)|^2$ profile shows up after choosing a smaller range on the ordinate.

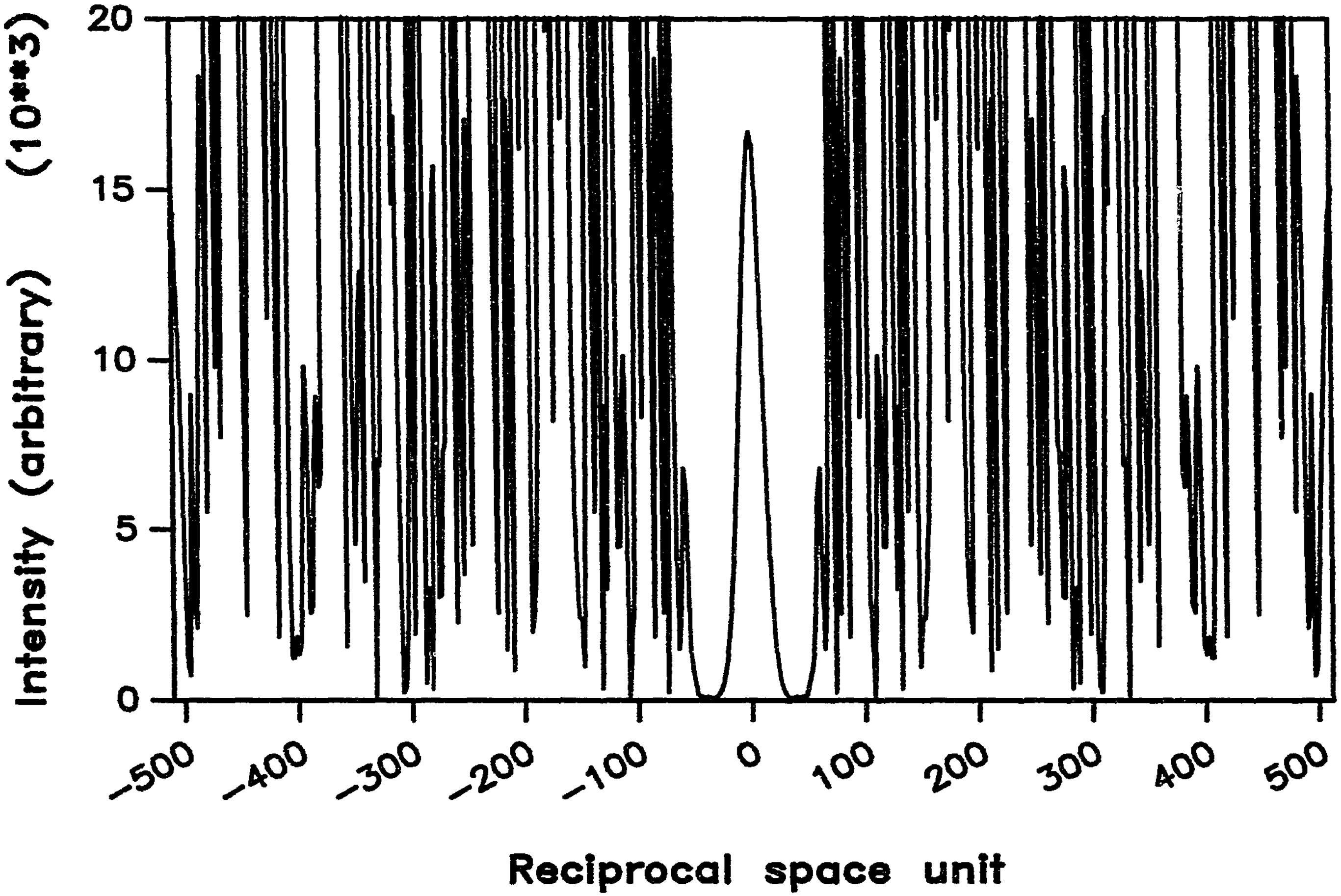

Figure I.18 (Continued) The Gaussian character of the $|F(\zeta)|^2$ profile is easier to see, after choosing a smaller range on the abscissa.

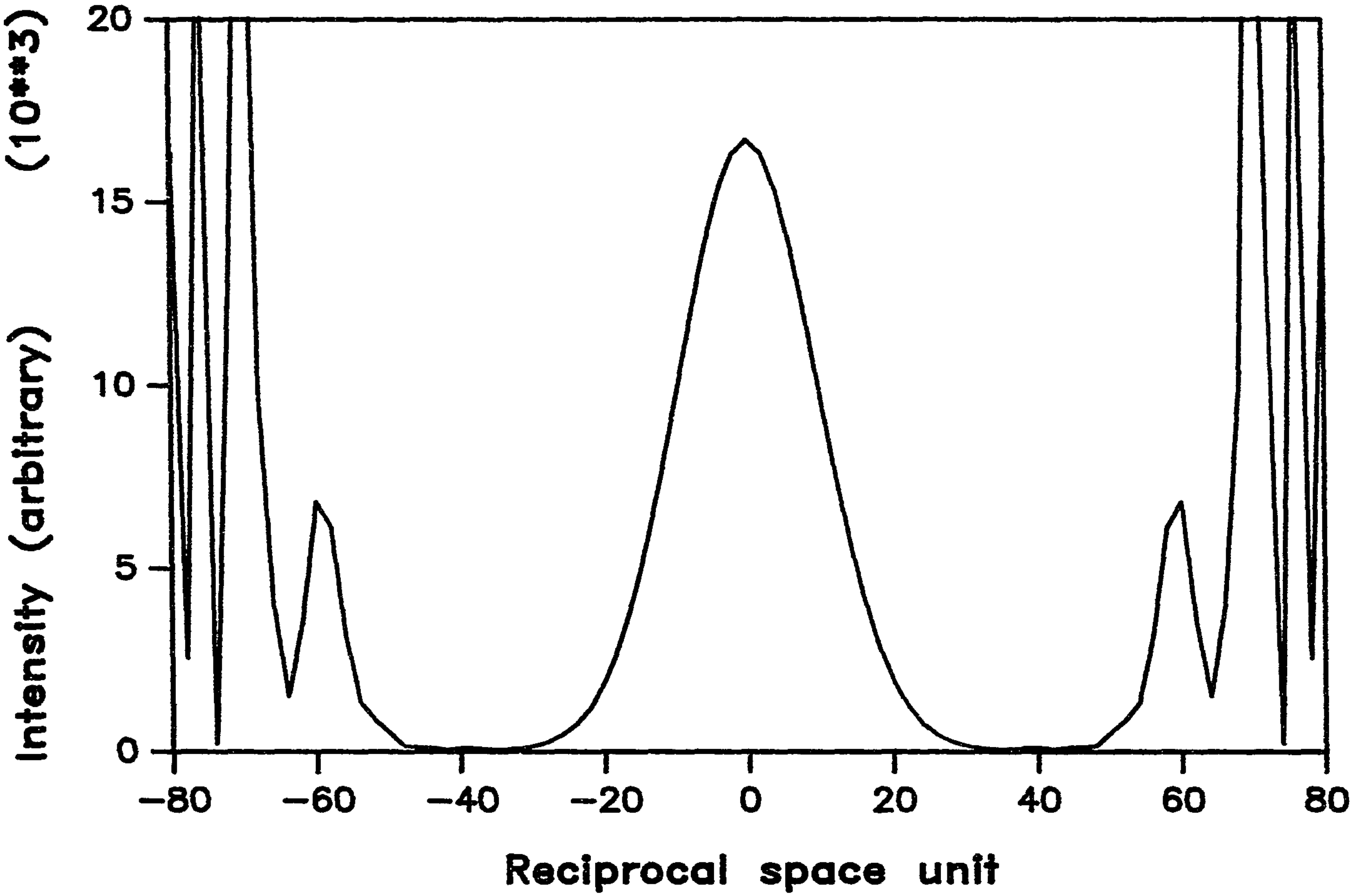

After choosing a smaller range on the abscissa and change the scale of the ordinate, the Gaussian feature of $|F(\zeta)|^2$ can be revealed (Fig. I.18c) and since the main peak of $|F(\zeta)|^2$ is free of noise, it guarantees that the backward Fourier transform, after truncating the wings of the $F(\zeta)$ profile beyond - 35 and + 35 reciprocal space units, will be successful.

In practice, it is not appropriate to modify the $|F(\zeta)|^2$ file before the backward Fourier transformation, due to the fact that the recorded $h(\nu)$ and $g(\nu)$, as well as the resultant $f(\nu)$ profiles, are not necessarily symmetrical peaks, in contrast to a true Gaussian peak or a Lorentzian peak; hence the imaginary parts of the transform are non-zero. If the $|F(\zeta)|^2$ file were truncated, and the $F(\zeta)$ file were recovered by simply taking the square root of the $|F(\zeta)|^2$ file for the backward Fourier transform, the "phase" of the originally complex file $F(\zeta)$ would be lost, and features of the resulting $f(\nu)$ file would be distorted.

In the present work, the elimination of the accumulated discontinuities was done immediately after the forward Fourier transform on both $H(\zeta)$ and $G(\zeta)$ profiles by recognizing the starting points of the background on the corresponding $|H(\zeta)|^2$ and $|G(\zeta)|^2$ files, then nullifying the $H(\zeta)$ and $G(\zeta)$ files beyond their corresponding background points. The background points were determined by finding the first region having a length, say, one fifth of that of the array, away from the center of the $|H(\zeta)|^2$ and $|G(\zeta)|^2$ files, for which the average "intensity" is less than ~ 2% of the "intensity" of the apex. The first points of such a region were taken as the background points.

Fig. I.19 shows $f(\nu)$ which resulted from the deconvolution of Gaussian $g(\nu)$ from $h(\nu)$. The $f(\nu)$ profile appears to be Gaussian and this is confirmed by noting that the measured FWHM's obey the relationship corresponding to that of Gaussian functions: $f^2 = h^2 - g^2$.

Fig. I.20 is that for a Lorentzian $f(\nu)$. It also has the Lorentzian characteristics that the measured FWHM's obey the relation of that of Lorentzian functions: $f = h - g$.

On comparison of Fig. I.19 to Fig. I.20, one finds that the background wings of the Lorentzian $f(\nu)$ are much "noisier" than those of the Gaussian $f(\nu)$. This is reasonable because the Gaussian functions $g(\nu)$ and $h(\nu)$ converge more quickly than the Lorentzian functions $g(\nu)$ and $h(\nu)$ do. Hence when the profiles were truncated within the same range, the discontinuities associated with the Gaussian $g(\nu)$ and $h(\nu)$ profiles are less serious, and the "starting points" of background of both the $|H(\zeta)|^2$ and $|G(\zeta)|^2$ profiles are closer to zero than are those of the Lorentzian counterparts. Since the discontinuities not only merge into the background wings but also the bodies of the $H(\zeta)$ and $G(\zeta)$ profiles during the forward Fourier transform, the body of the Lorentzian $f(\nu)$ profile is not as smooth as that of the Gaussian $f(\nu)$ either.

Figure I.19 A deconvoluted *f*(v) profile (FWHM 0.8°) obtained after the truncation on the Gaussian *G*(v) profile and the *H*(v) profile, to get rid of the associated noise. The Gaussian profiles *h*(v) (FWHM 1.0°) and *g*(v) (FWHM 0.6°) in Fig I.8 and I.9 are included for comparison.

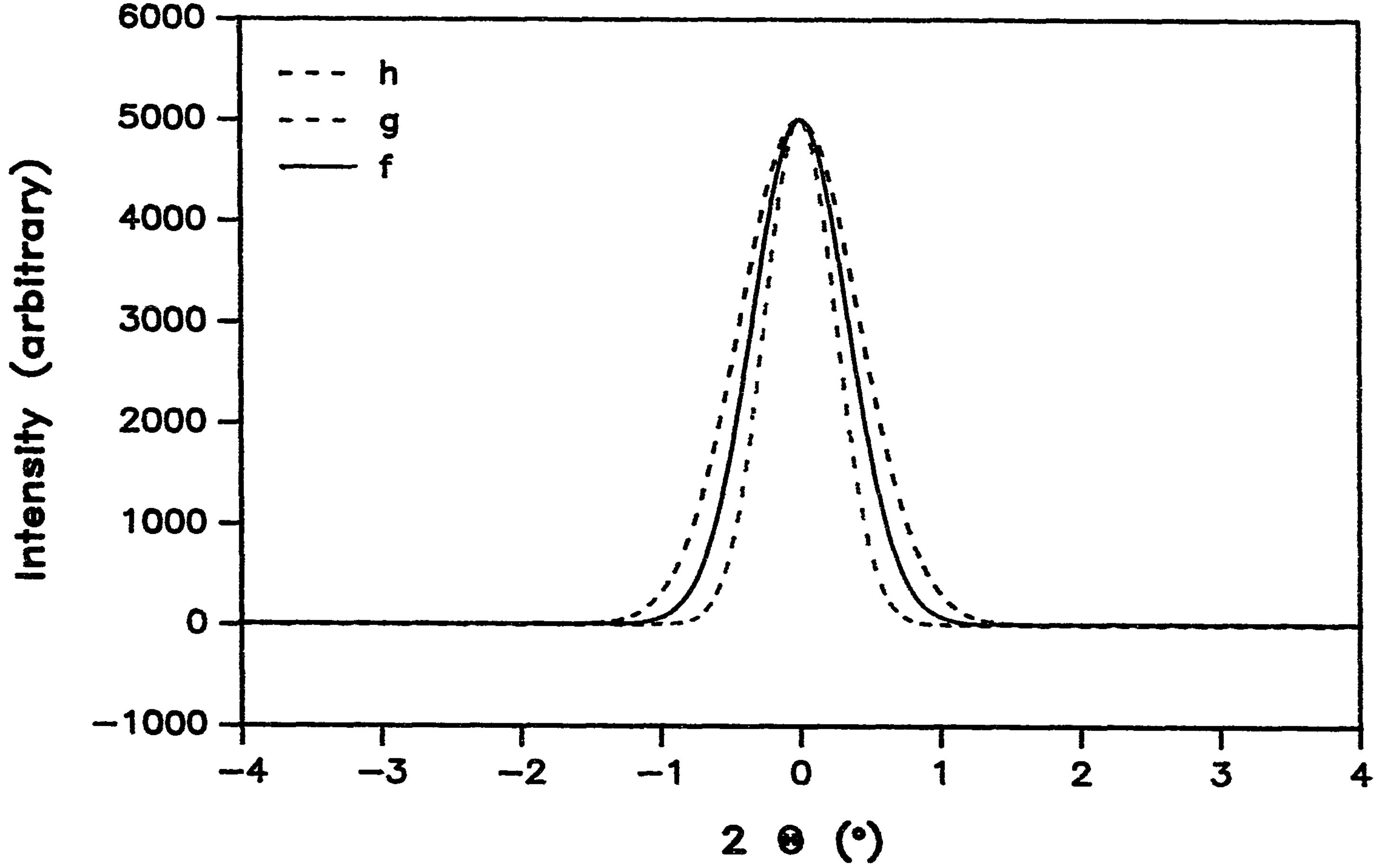

Figure I.20 A deconvoluted $f(v)$ profile (FWHM 0.4°) obtained after the truncation on the Lorentzian $G(v)$ profile and the $H(v)$ profile, to get rid of the associated noise. The Lorentzian profiles $h(v)$ (FWHM 1.0°) and $g(v)$ (FWHM 0.6°) are included for comparison.

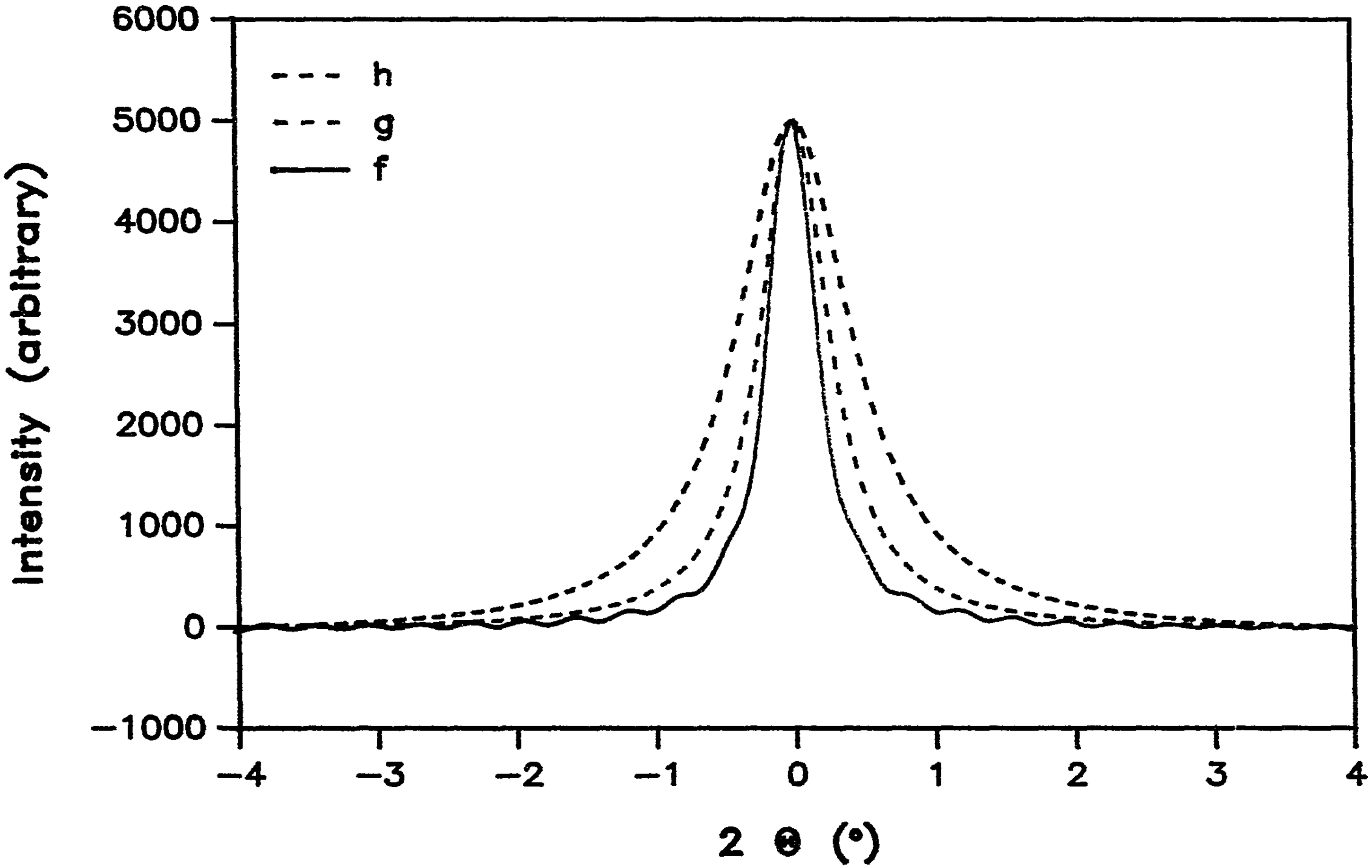

However, even in the Lorentzian case, which had noisier background wings than the Gaussian, it still seems valid to measure the peak width at half intensity of the apex with respect of the averaged base line of these multiple-peak profiles.

There is another function termed a Pseudo Voigt function, which is essentially a linear combination of a Gaussian function and a Lorentzian function. If one gradually mixes a Lorentzian function into a Gaussian function such that the resulting Pseudo Voigtian $g(\nu)$ and $h(\nu)$ functions changes, the extent of the noisy background wings of the deconvoluted Pseudo Voigtian $f(\nu)$ will increase. This can be readily seen on Fig. I .21 to Fig. I .29.

All of this can serve as a ***reductio ad absurdum*** supporting the above statement that the discontinuities play a key role in the failure of the backward Fourier transform.

Figure I.21 Deconvolution of the Pseudo Voigt (component: 0.1 Gaussian + 0.9 Lorentzian) *g*(v) profile from the *h*(v) profile to obtain an *f*(v) profile.

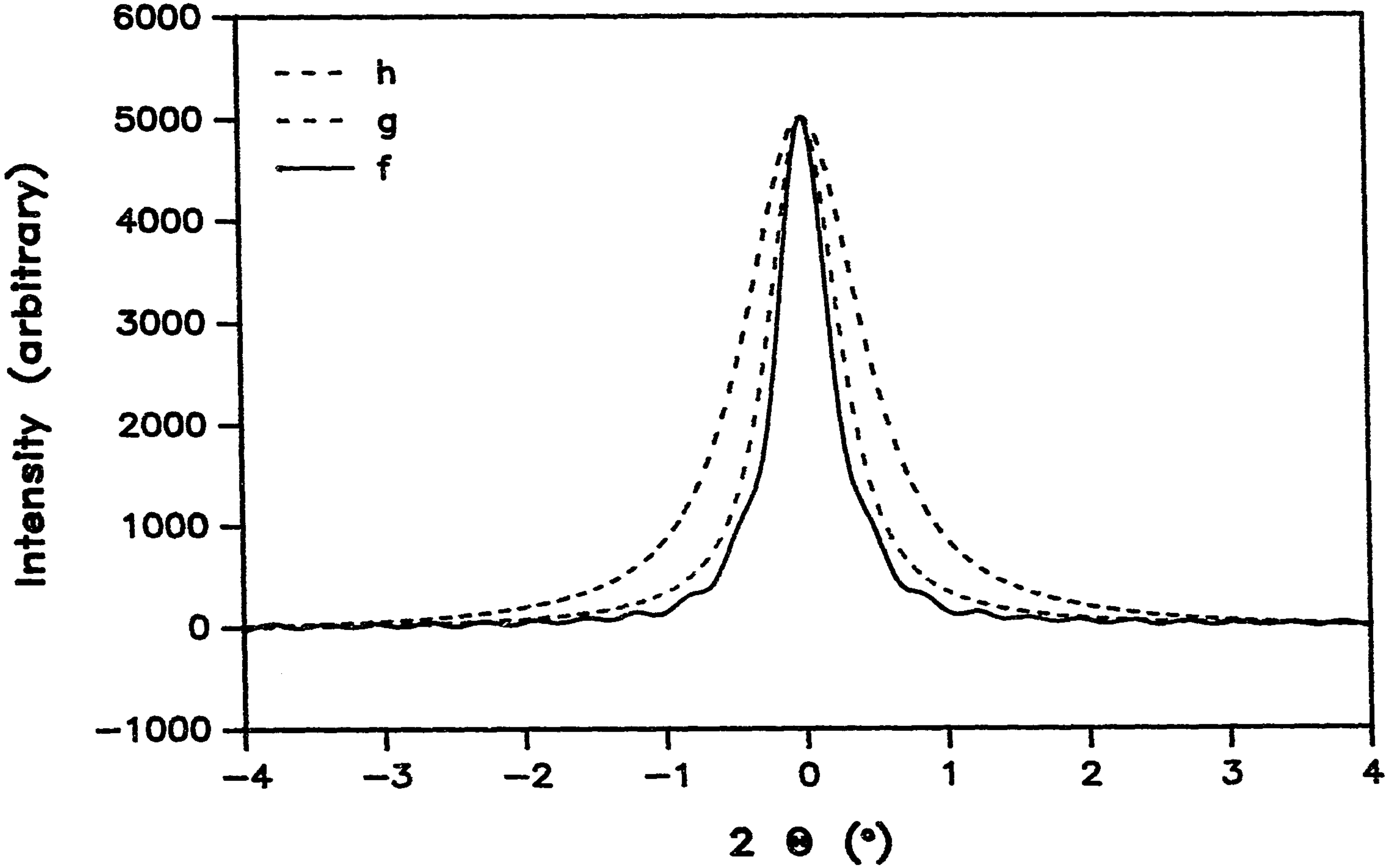

Figure I.22 Deconvolution of the Pseudo Voigt (component: 0.2 Gaussian + 0.8 Lorentzian) $g(\nu)$ profile from the $h(\nu)$ profile to obtain an $f(\nu)$ profile.

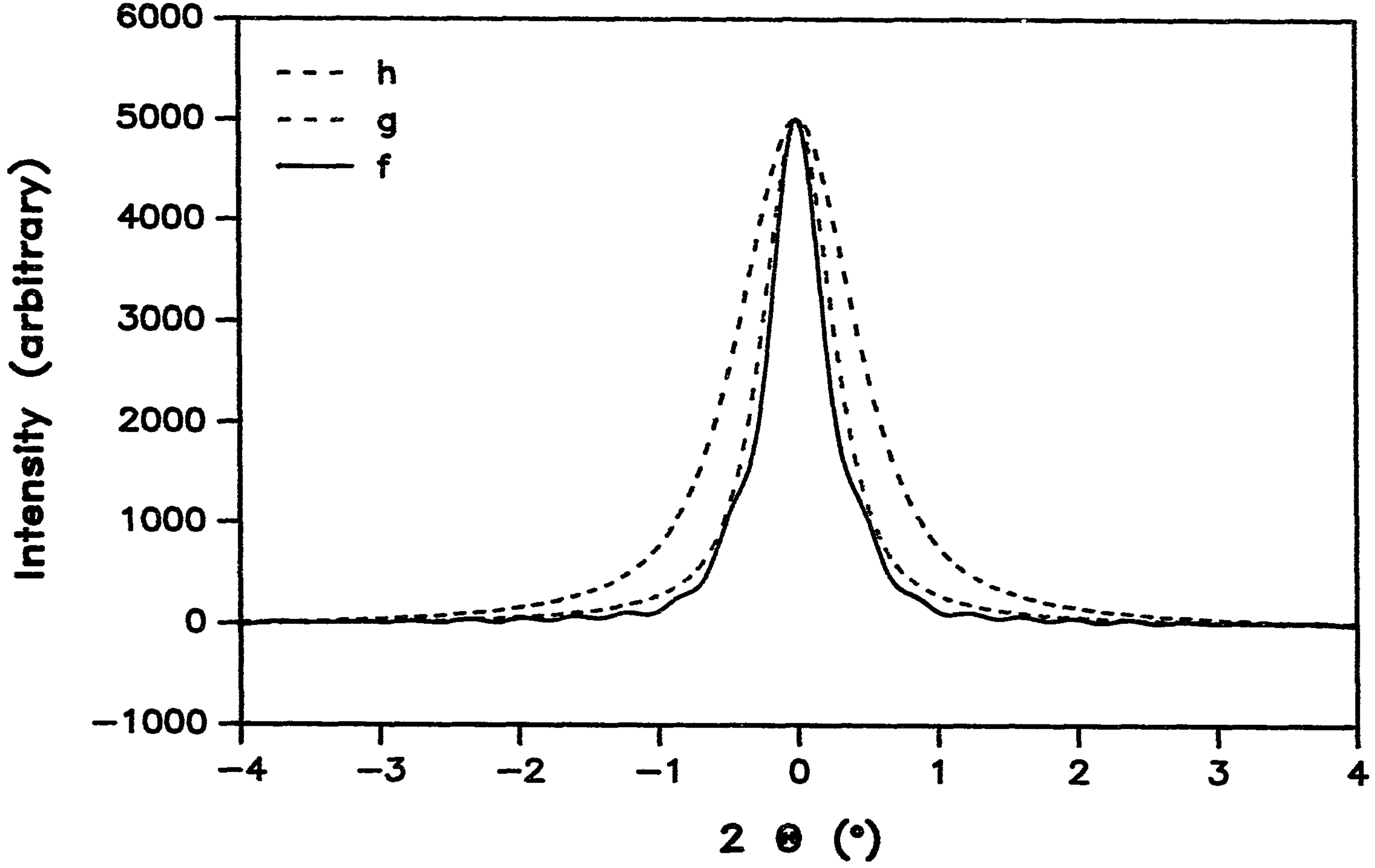

Figure I.23 Deconvolution of the Pseudo Voigt (component: 0.3 Gaussian + 0.7 Lorentzian) *g*(v) profile from the *h*(v) profile to obtain an *f*(v) profile.

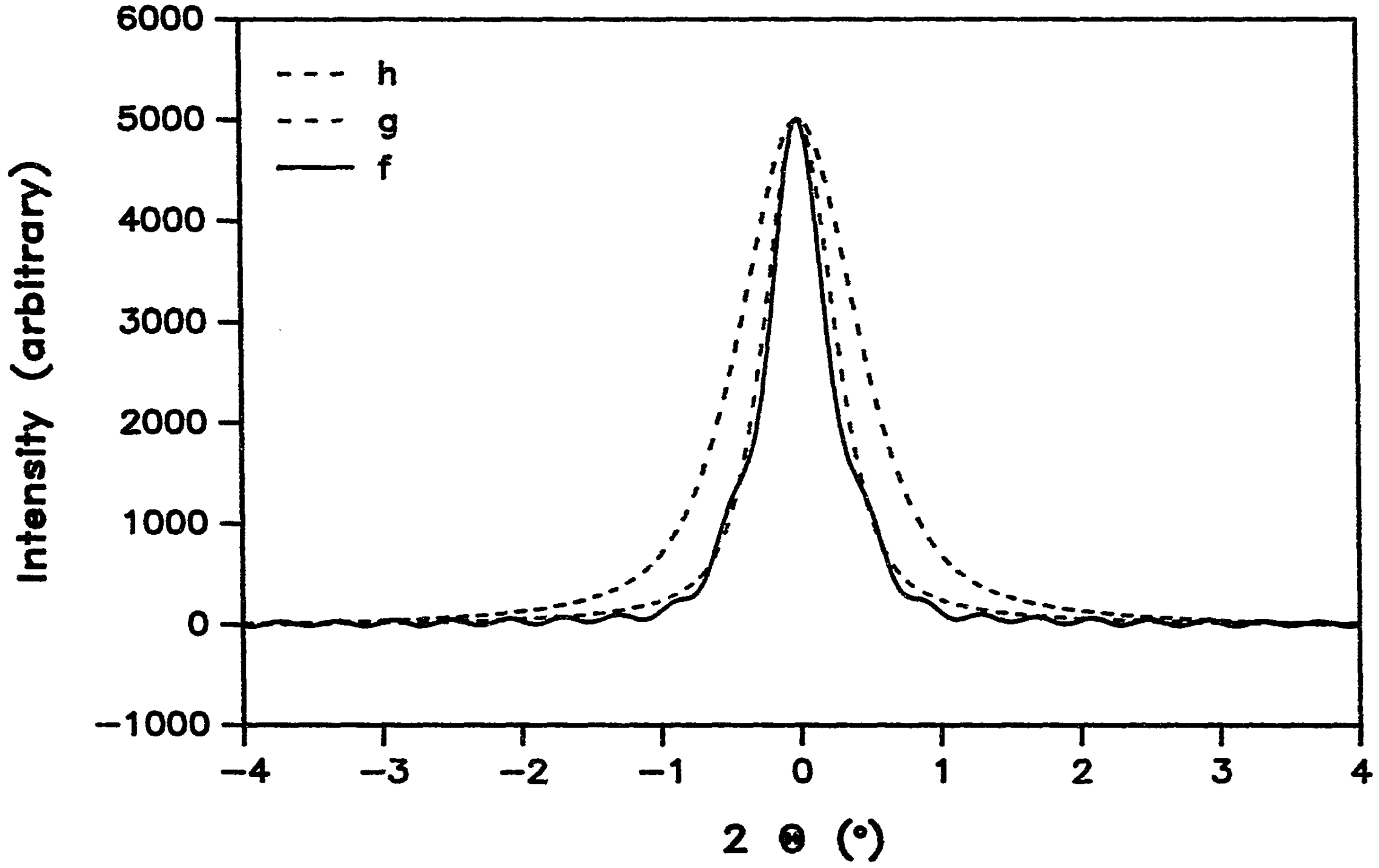

Figure I.24 Deconvolution of the Pseudo Voigt (component: 0.4 Gaussian + 0.6 Lorentzian) *g*(v) profile from the *h*(v) profile to obtain an *f*(v) profile.

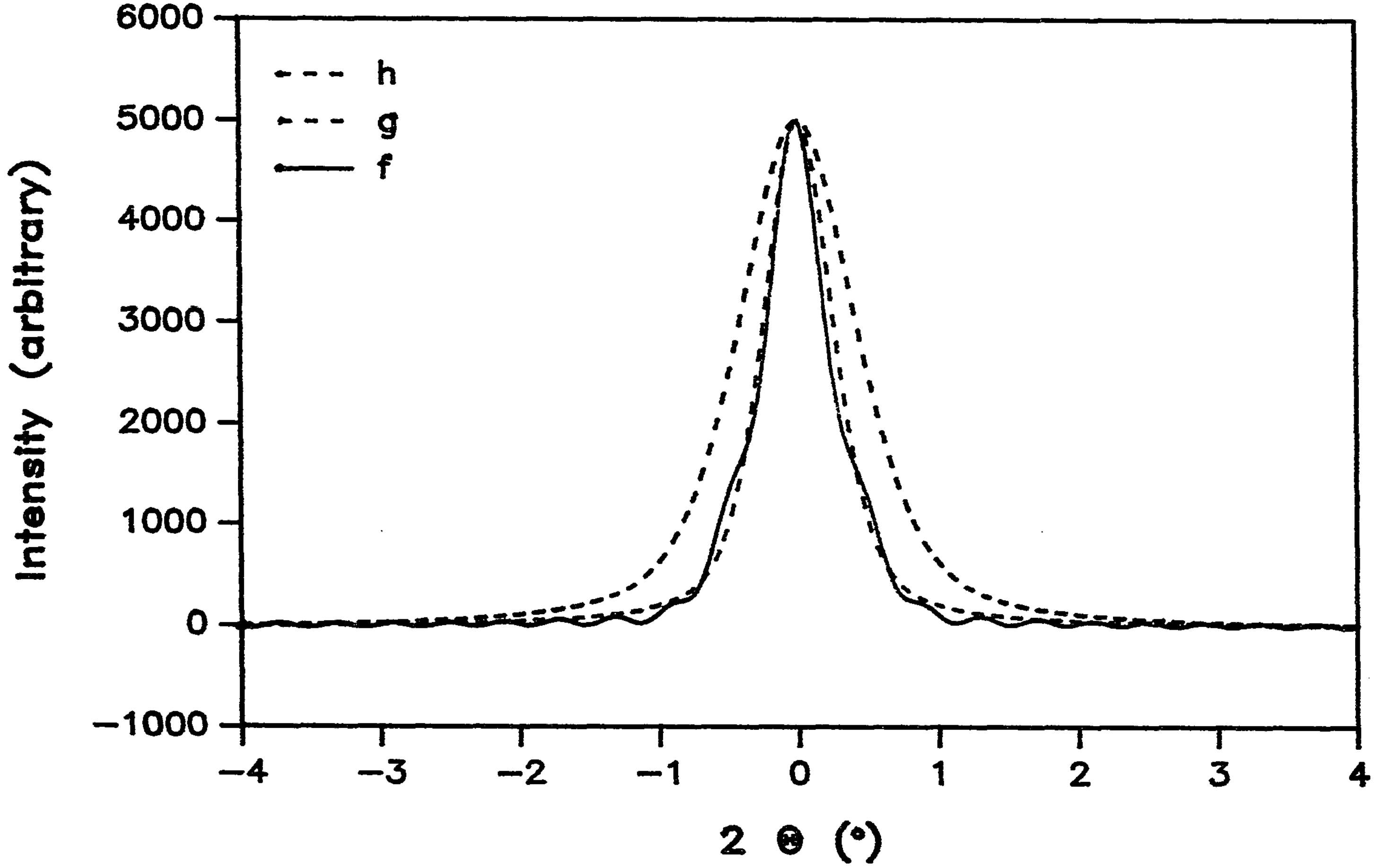

Figure I.25 Deconvolution of the Pseudo Voigt (component: 0.5 Gaussian + 0.5 Lorentzian) $g(v)$ profile from the $h(v)$ profile to obtain an $f(v)$ profile.

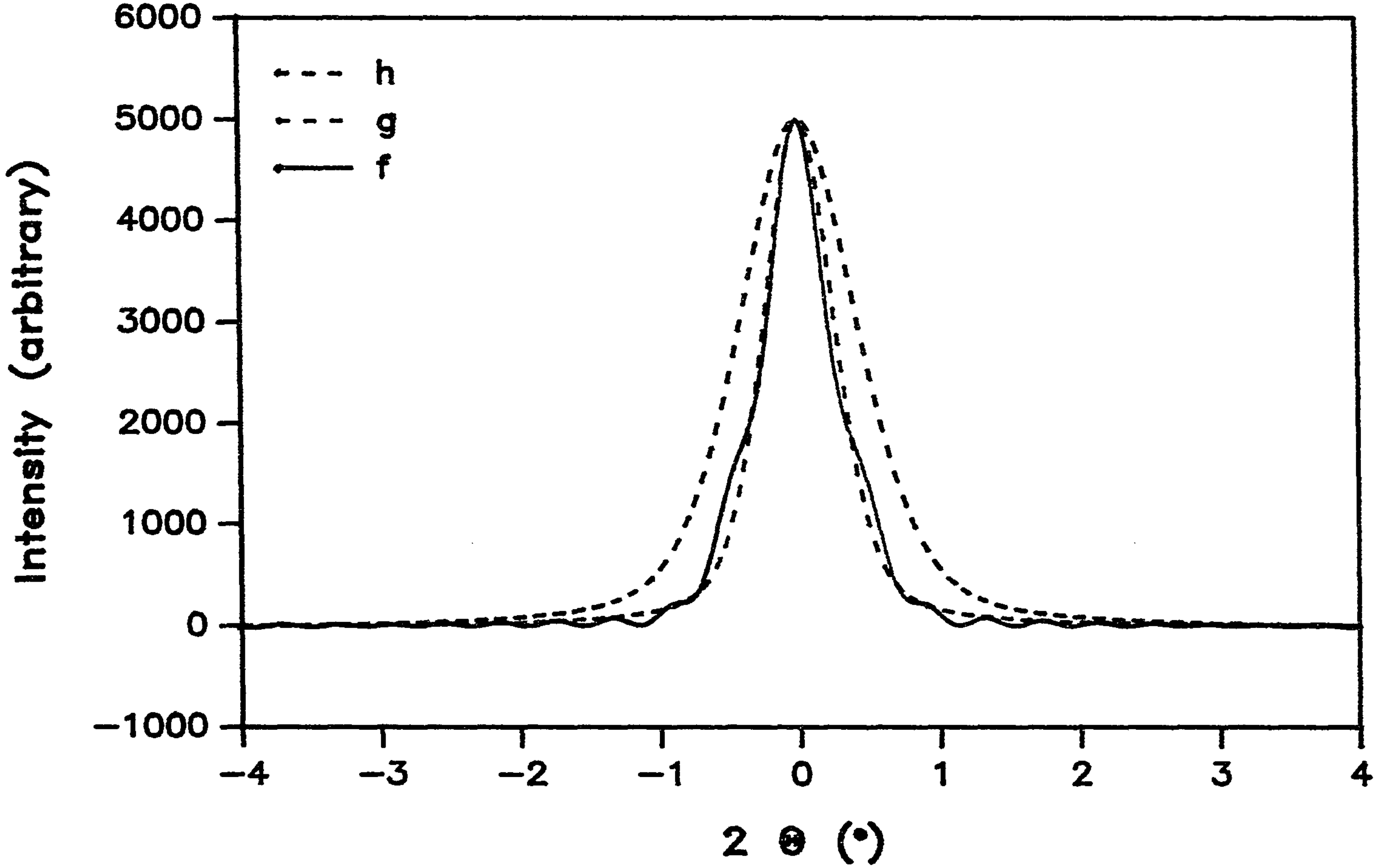

Figure I.26 Deconvolution of the Pseudo Voigt (component: 0.6 Gaussian + 0.4 Lorentzian) $g(v)$ profile from the $h(v)$ profile to obtain an $f(v)$ profile.

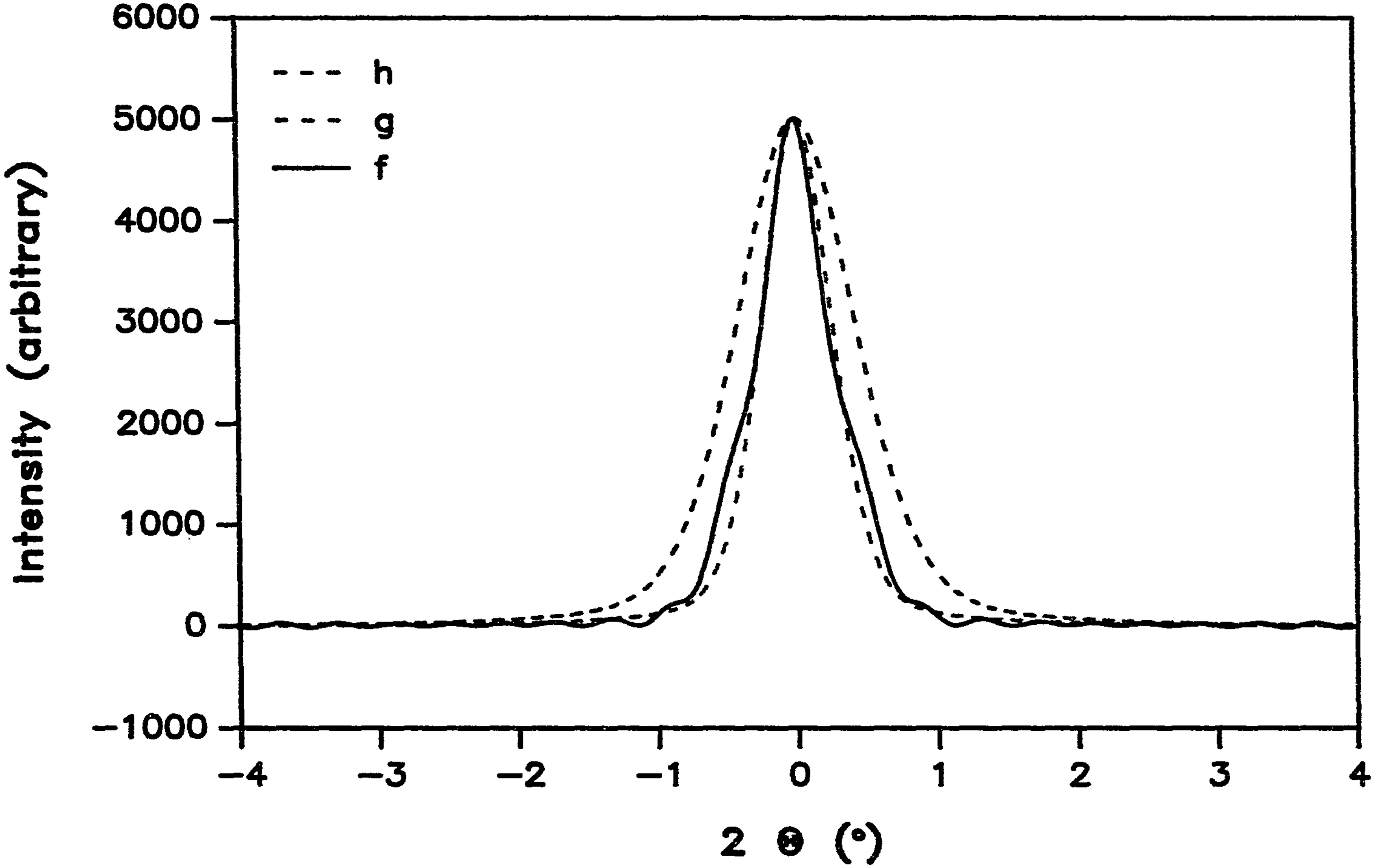

Figure I.27 Deconvolution of the Pseudo Voigt (component: 0.7 Gaussian + 0.3 Lorentzian) $g(\nu)$ profile from the $h(\nu)$ profile to obtain an $f(\nu)$ profile.

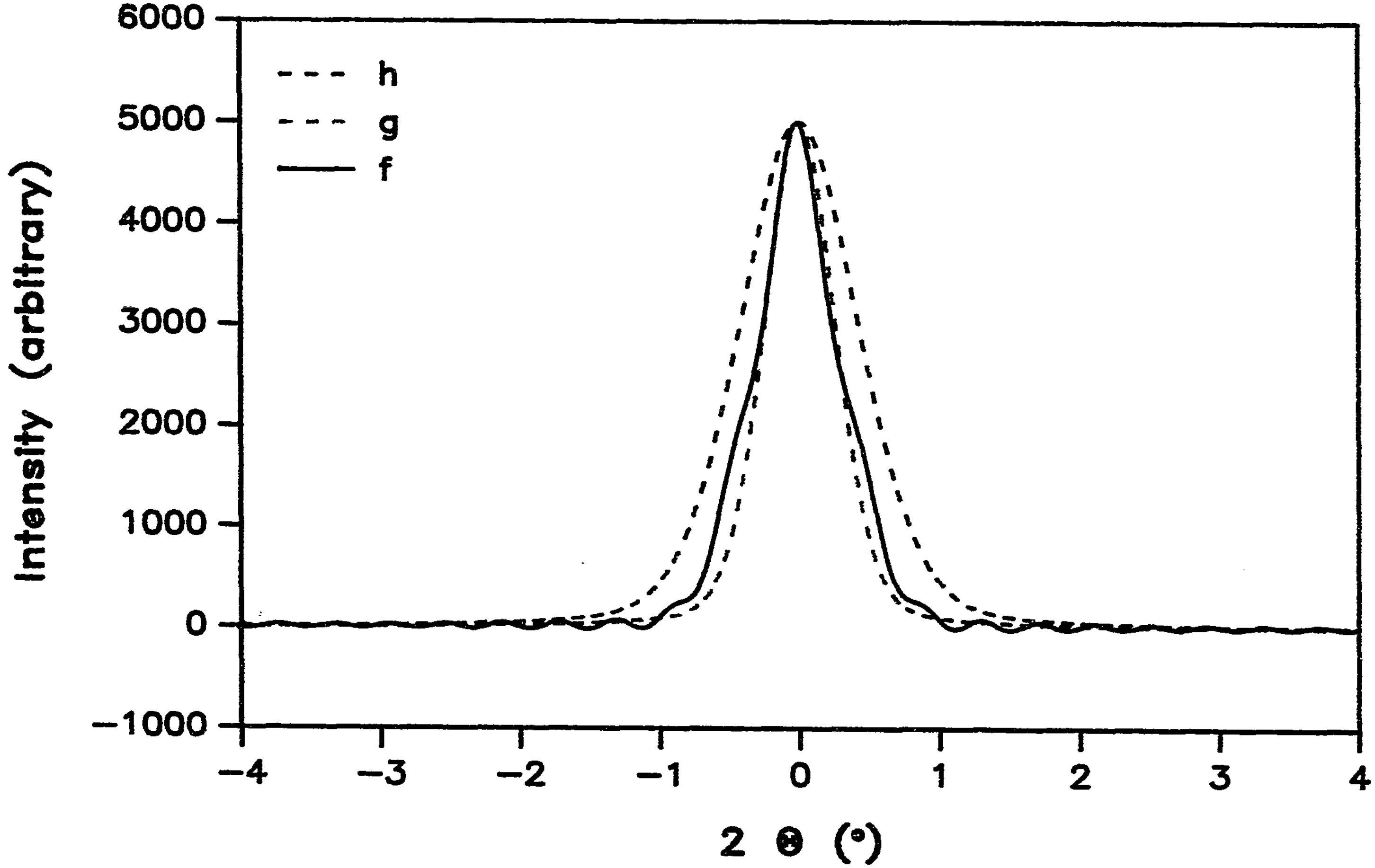

Figure I.28 Deconvolution of the Pseudo Voigt (component: 0.8 Gaussian + 0.2 Lorentzian) *g*(v) profile from the *h*(v) profile to obtain an *f*(v) profile.

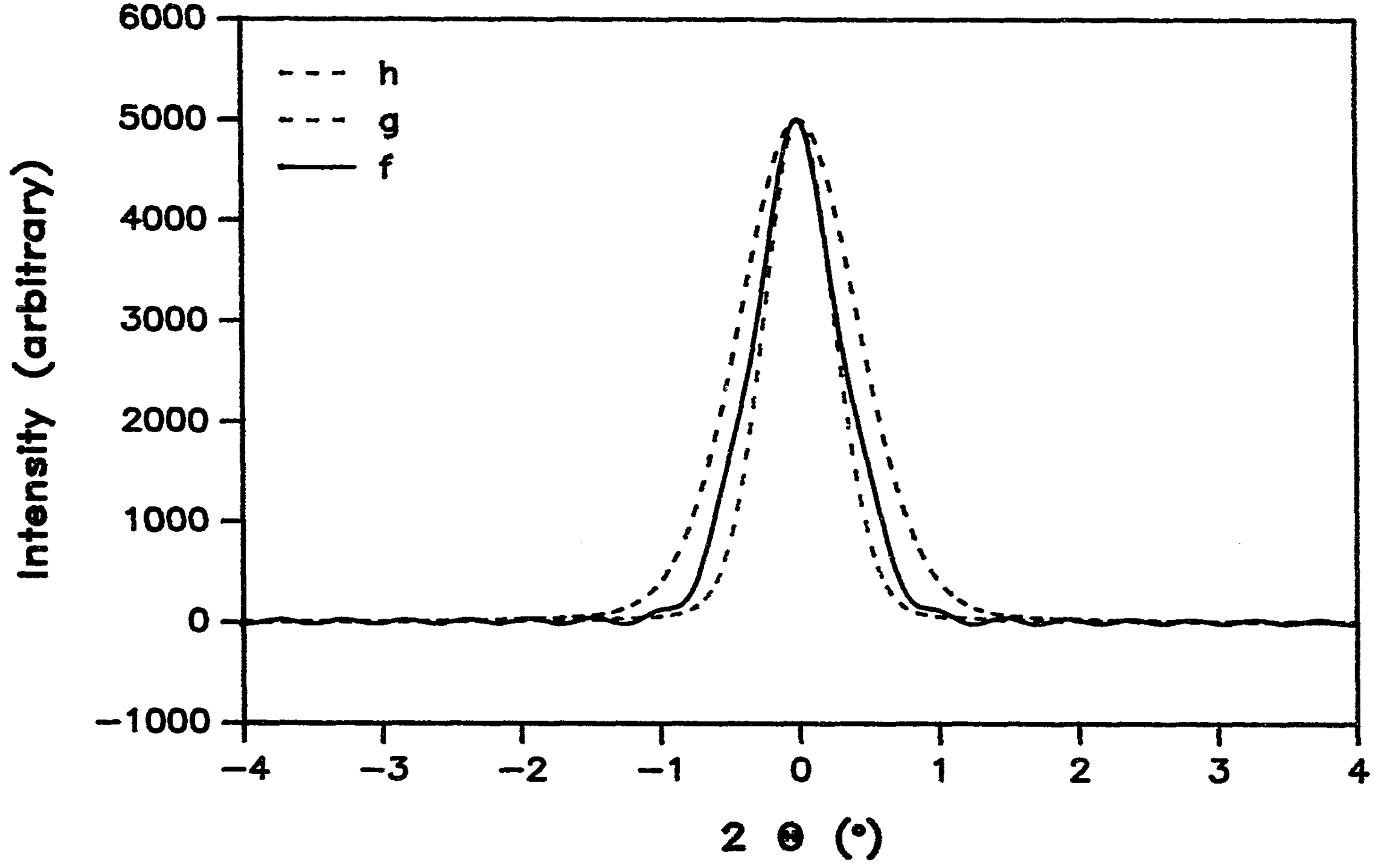

Figure I.29 Deconvolution of the Pseudo Voigt (component: 0.9 Gaussian + 0.1 Lorentzian) *g*(v) profile from the *h*(v) profile to obtain an *f*(v) profile.

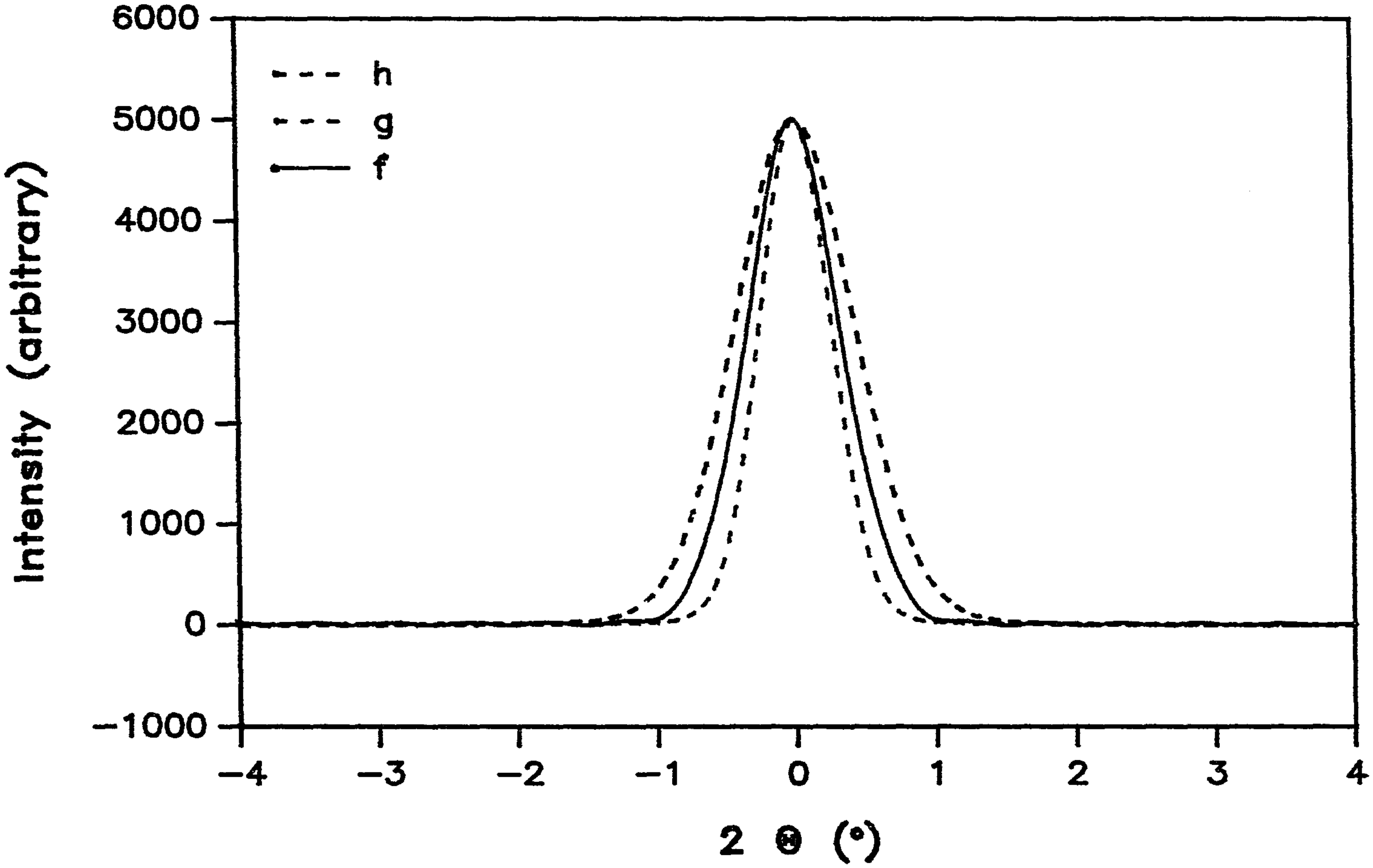

# RESULTS AND DISCUSSION

The $f(\nu)$ profiles resulting from the deconvolution of $g(\nu)$ from $h(\nu)$ for $Nd_2Fe_{14}B$ Ribbon, using either isolated peaks at 27° and 63°, or multiple peaks at 35° - 40°, 41° - 45° and 55° - 60° are shown on Fig. I .30 - I .34. It can be seen that the $f(\nu)$ profiles of the single peaks have less noisy background wings than those of the multiple peaks. This is understandable because the latter have wider ranges covered, thus more noise is merged in the patterns, and the least square spline smoothing for both $g(\nu)$ and $h(\nu)$ profiles might not have filtered the noise intrinsic in them to the degree that was attained in the single $g(\nu)$ and $h(\nu)$ profiles.

In order to confirm whether the $f(\nu)$ profile thus obtained accurately models the pure peak broadening contribution, a Fourier convolution of the $f(\nu)$ profile into the corresponding spline smoothed $g(\nu)$ profile to form a convoluted $h'(\nu)$ profile for a peak at 27° has been done. The result is shown on Fig. I .35. In terms of FWHM, the convoluted $h'(\nu)$ profile is in excellent agreement with the spline smoothed $h(\nu)$ profile. The slight difference between them is believed due to the selection of the truncating points on both the $H(\zeta)$ and $G(\zeta)$ profiles.

The grain size determinated according to the FWHM of each $f(\nu)$ profile as the pure peak broadening, $B$, in Scherrer's equation is shown on Table I .2. The peak position of each $f(\nu)$ profile refers to either the peak position of the single peak or that

Figure I.30 A deconvoluted $f(v)$ profile (FWHM 0.145°) obtained from peaks $h(v)$ and $g(v)$ at ~27° of the samples.

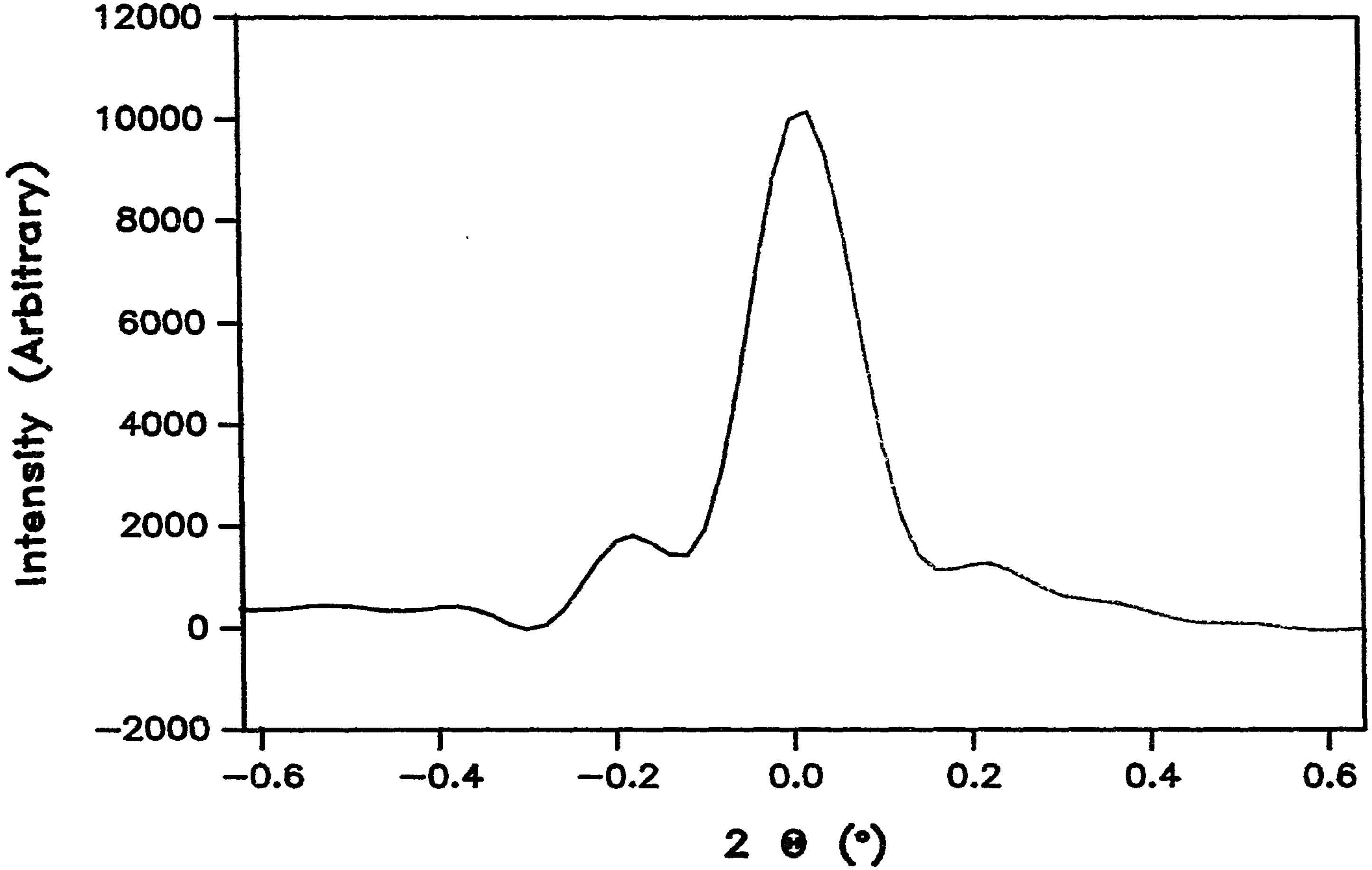

Figure I.31 A deconvoluted $f(v)$ profile (FWHM 0.137°) obtained from multiple peaks $h(v)$ and $g(v)$ at 35° - 40° of the samples.

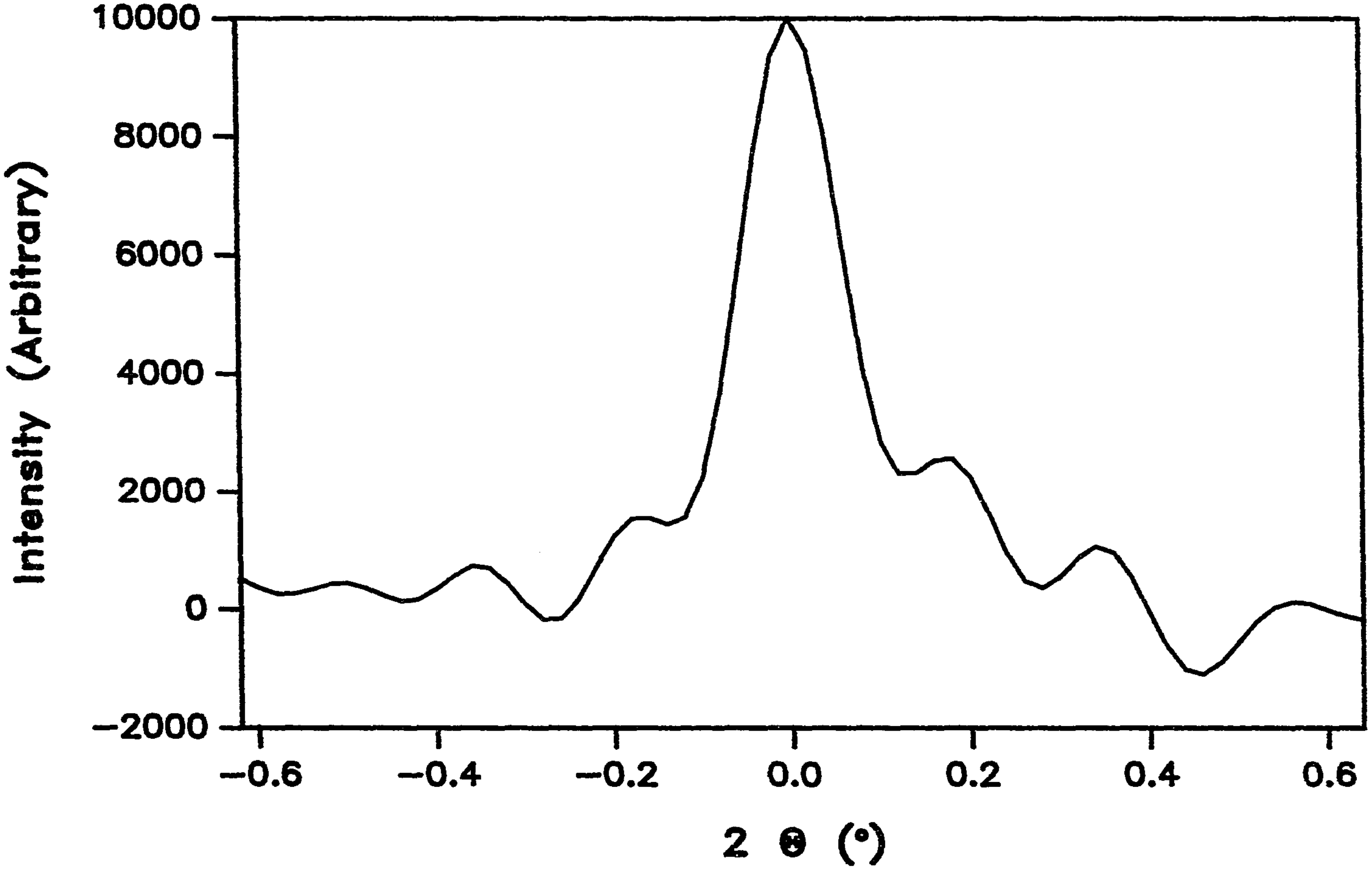

Figure I.32 A deconvoluted *f*(v) profile (FWHM 0.139°) obtained from multiple peaks *h*(v) and *g*(v) at 41° - 45° of the samples.

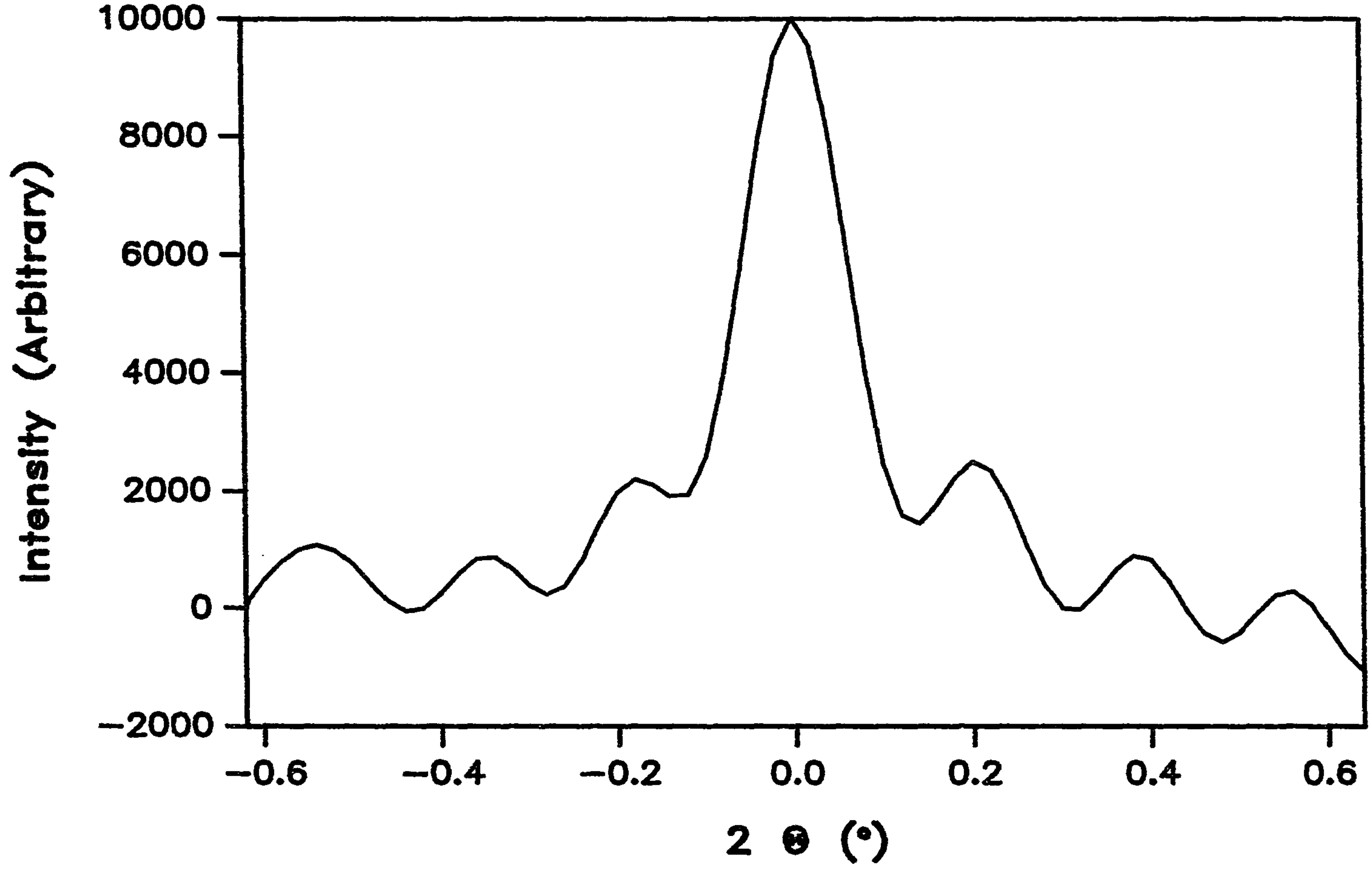

Figure I.33 A deconvoluted *f*(v) profile (FWHM 0.149°) obtained from multiple peaks *h*(v) and *g*(v) at 55° - 60° of the samples.

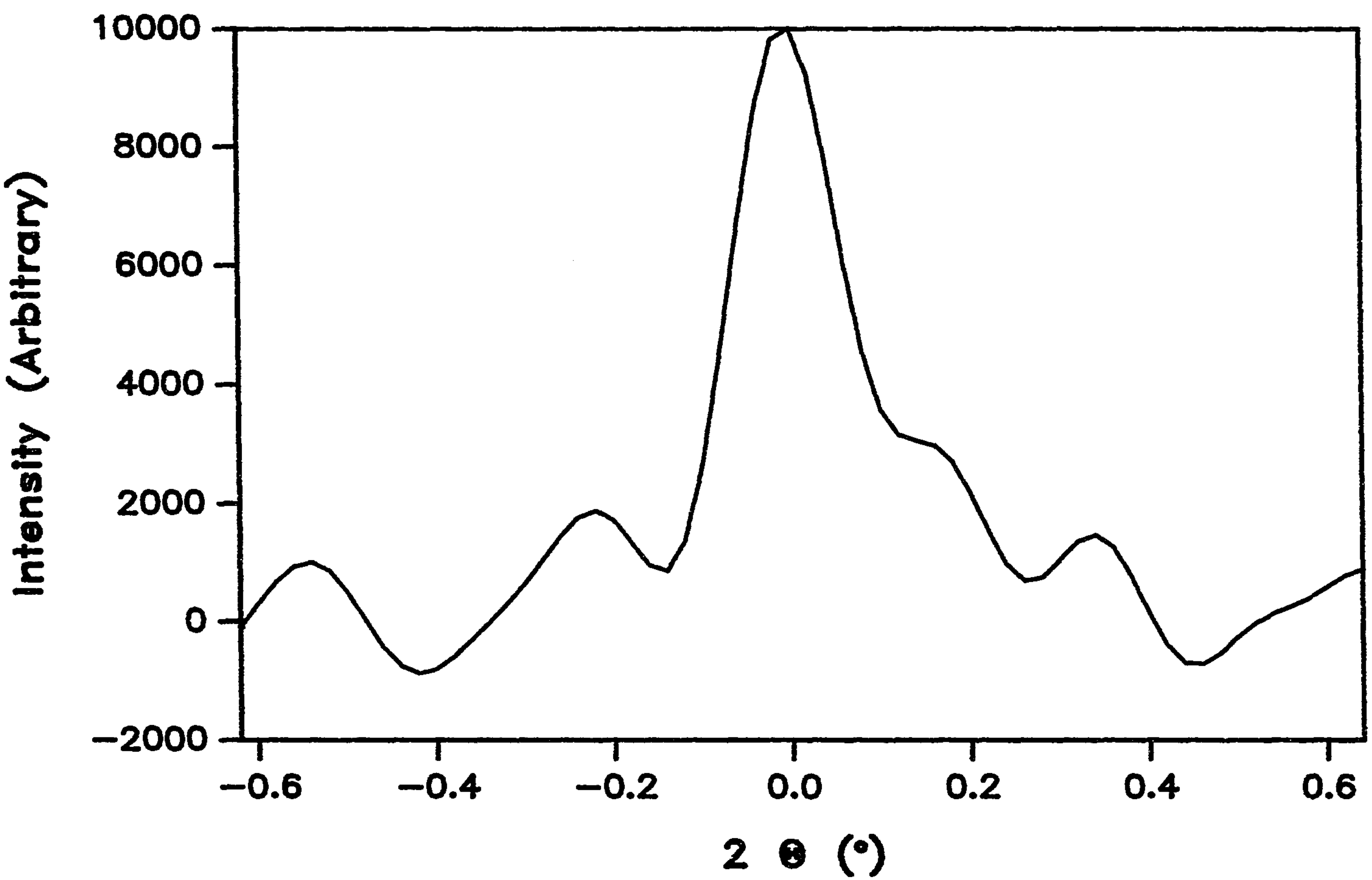

Figure I.34 A deconvoluted *f*(v) profile (FWHM 0.159°) obtained from peaks *h*(v) and *g*(v) at ~62° of the samples.

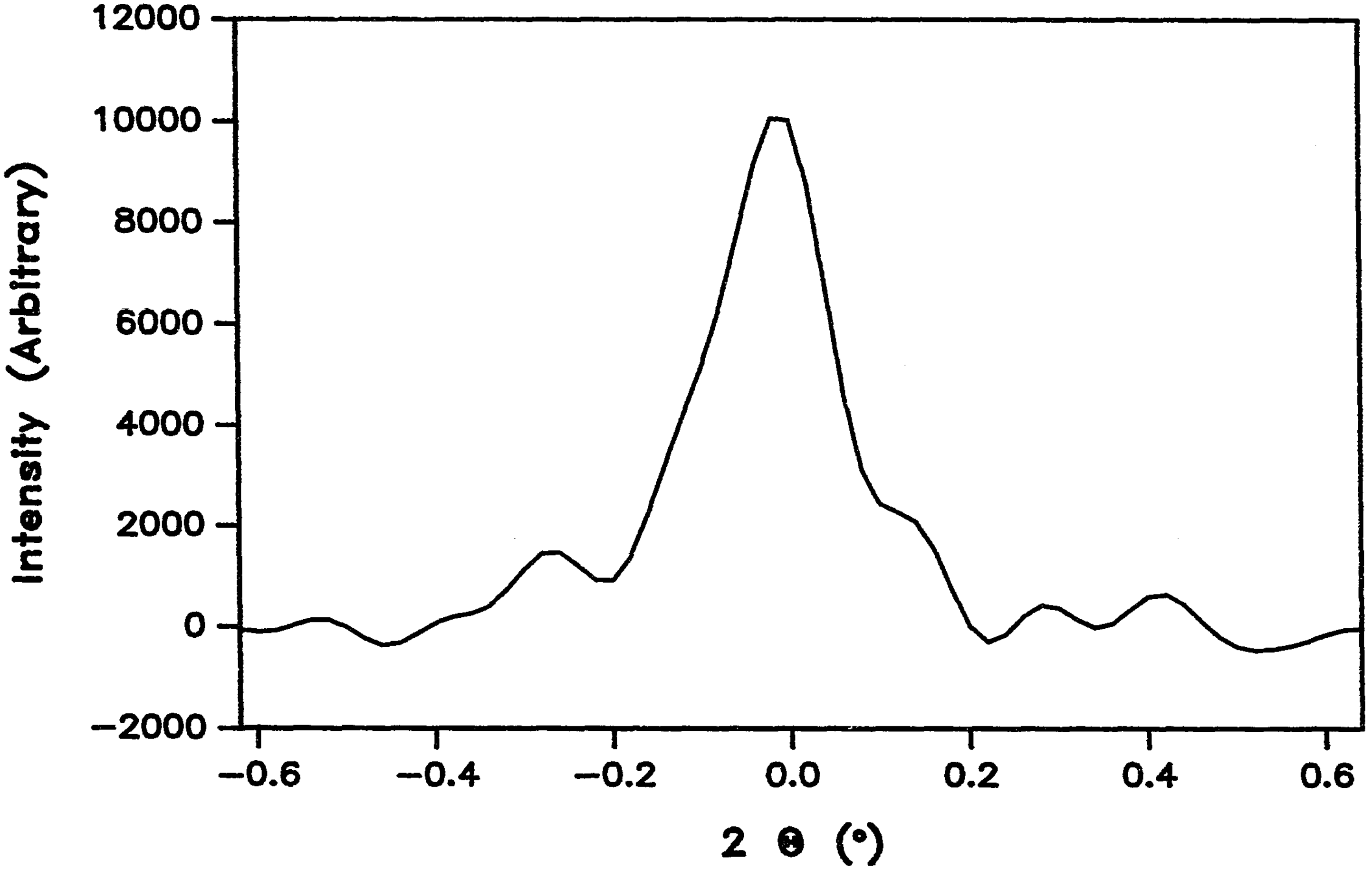

Figure I.35 Comparison of the convoluted *h*'(v) profile with the input least squares spline smoothed *h*(v) profile. The *h*'(v) profile is obtained by the convolution of the least squares spline smoothed *g*(v) profile at ~27° of the sample pattern and the *f*(v) profile shown on Fig I.30.

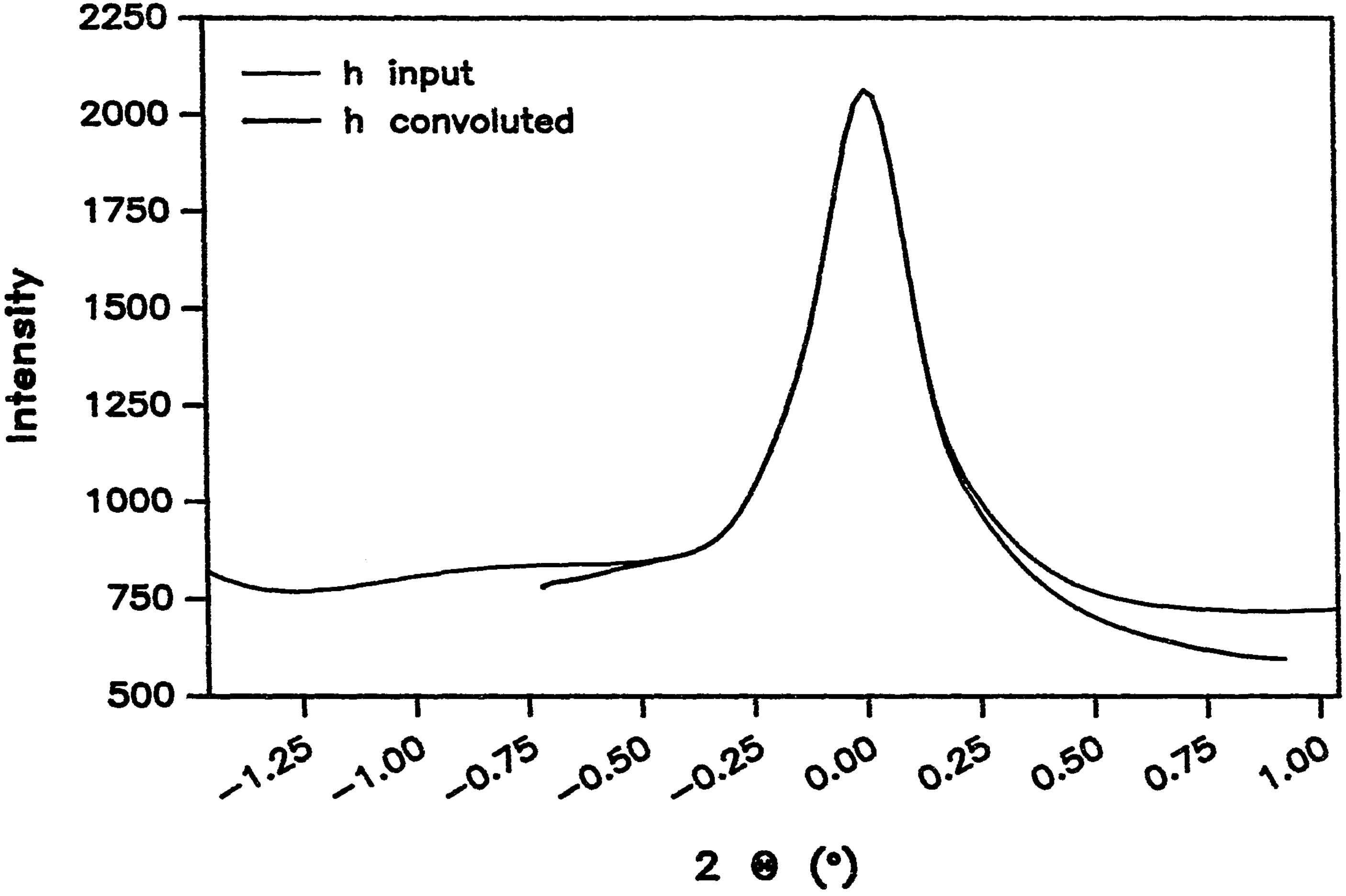

of the highest peak of the peak clusters.

Table I.2 Grain Size Determination for $Nd_2Fe_{14}B$ Ribbon by Fourier Deconvolution

| Two theta (degree) | Peak Broadening (degree) | Grain Size (Angstrom) |
|---|---|---|
| 26.96 | 0.145 | 359.9 |
| 37.26 | 0.137 | 391.0 |
| 42.32 | 0.139 | 391.6 |
| 58.00 | 0.149 | 389.5 |
| 62.84 | 0.159 | 374.0 |
| average |  | 381.2 |

# CONCLUSION

Of the numerous methods for determining the grain size of a powdered sample, the Fourier deconvolution is the most powerful technique, as it can be used regardless of the functional nature of the profile of the recorded patterns. The FWHM of the deconvoluted $f(\nu)$ can be directly measured and used in Scherrer's formula, instead of having to be calculated by either $B^2 = B_H^2 - B_g^2$ or $B = B_h - B_g$ depending on the mathematical functional nature of the peak. The method will also work whether the peaks in question are symmetrical or not.

The grain size determined by Fourier deconvolution is in excellent agreement with that observed by the transmission electron microscope and comparable with that determined by Rietveld refinement.

The truncation of the $H(\zeta)$ and $G(\zeta)$ files, i.e., the nullifying the $H(\zeta)$ and $G(\zeta)$ files beyond their corresponding background points in order to eliminate the accumulated discontinuities associated with them, is crucial for the success of the backward Fourier transform. General speaking, the $H(\zeta)$ and $G(\zeta)$ files are the reciprocal $\zeta$ space expressions of the $g(\nu)$ and $h(\nu)$ profiles in the $\nu$ space. The wider the $H(\zeta)$ and $G(\zeta)$ files are after truncation, the narrower the $f(\nu)$ profile will be after the backward Fourier transform, but also the more noise and discontinuities which will remain.

On the other hand, if one truncates the $H(\zeta)$ and $G(\zeta)$ files too much, one will end up with a "wide" $f(\nu)$ profile which might not accurately model the pure peak broadening contribution.

The method used to determine the points in the $H(\zeta)$ and $G(\zeta)$ files for the starting points of the backgrounds appears reasonable but is not necessarily the best approach and needs further study in the future work. A simplex optimization technique[19] could be employed to carry out this task. Different truncating points could be chosen on the $H(\zeta)$ and $G(\zeta)$ files to obtain different $f(\nu)$ profiles, which could subsequently be convoluted into the spline smoothed $g(\nu)$ profile to obtain different $h'(\nu)$ profiles. A simplex minimization of the difference between the convoluted $h'(\nu)$ profiles and the originally spline smoothed $h(\nu)$ profile, could find out the best combination of the truncating point on the $H(\zeta)$ file with that on the $G(\zeta)$ file, to yield the best $f(\nu)$ profile.

One of the advantages of the simplex optimization is that, in contrast to the commonly used least squares optimization which works with derivatives, it does not mathematically require an analytical relation of the truncating point to the difference between the $h'(\nu)$ profile and the $h(\nu)$ profile. Also, it guarantees convergency.

## REFERENCES

[1] H. P. Klug and L. E. Alexander, *X-ray Diffraction Procedures for Polycrystalline and Amorphous Materials.* Chapter 5. (Wiley, New York, 1974.)

[2] *ibid*, page 500.

[3] I. E. Anderson, B. K. Lograsso and W. M. McCallum, *Powder Processing of Rare Earth Iron Permanent Magnets.* Presentation in ASM **International Materials Week 1990, Program : Magnetic Material, Session IV : Physical Metallurgy of Magnetic Materials.** Detroit, Oct 7 - 11, 1990.

[4] C. M. Hsu and R. W. McCallum, *Crystallization and Grain Growth of* $Nd_2Fe_{14}B$ *from an Amorphous Precursor.* Ames Laboratory and the Department of Material Science and Engineering, Iowa State University (to be published).

[5] P. Scherrer, *Göttinger Nachrichten,* 2, 98 (1918).

[6] L. Bragg, *The Crystalline State, Vol. I., A General Survey.* page 189. (G. Bell and Sons, London, 1919).

[7] A. Schuster and J. W. Nicholson, *An Introduction to the Theory of Optics.* page 11. (Edward Arnold and Co., London, third edition, 1942).

[8] B. E. Warren and J. Biscoe, *J. Am. Ceram. Soc.,* 21, 49 (1938).

[9] B. E. Warren, *J. Appl. Phys.,* 12, 375 (1947).

[10] D. B. Wiles, A. Sakthivel and R. A. Young, *Program DBW3.2S for Rietveld Analysis of X-ray and Neutron Diffraction Patterns, Version 8840.* (School of Physics, Georgia Institute of Technology, Atlanta, GA 1988).

[11] R. A. Young, *Crystallite Size Broadening.* Presentation in the $2^{nd}$ GSAS Users Meeting, Los Alamos National Laboratory, Feb 27 - March 1, 1991.

[12] R. C. Spencer, *Phys. Rev.,* 55, 239 (1939).

[13] R. C. Spencer, *J. Appl. Phys.,* 20, 413 (1949).

[14] A. R. Stokes, *Proc. Phys. Soc. (London)*, 61, 382 (1948).

[15] C. G. Shull, *Phys. Rev.,* 70, 679 (1946).

[16] M. S. Paterson, *Phys. Soc. (London)*, 63A, 477 (1950).

[17] W. H. Press, B. P. Flannery, S. A. Teukolsky and W. T. Vetterling, *Numerical Recipes,* page 390 and references thereof. (Cambridge University Press, Cambridge, 1986).

[18] C. DeBoor, *A Practical Guide to Spline*, (Springer-Verlag, New York, Inc. 1978).

[19] J. A. Nelder and R. Mead, *Comput. J.,* 7, 308 (1965).

# SECTION II

# STRUCTURE DETERMINATION OF SELECTED SULFUR-CONTAINING ORGANOMETALLIC COMPOUNDS BY X-RAY DIFFRACTION AND MOLECULAR MECHANICS METHODS

# INTRODUCTION

Benzo-[2,3]-4-methyl-thiophene and dibenzothiophene are two compounds which are important in petroleum industry. These sulfur containing compounds decompose during the crude oil heat treating procedure and give out sulfur which will poison the catalyst. Thus with the concern in the oil industry pertaining to efficiency and to the environment, it is of significance to carry out research on various aspects of these compounds.

As a part of such research, an attempt was made in Dr. Angelici's group of the Department of Chemistry, ISU to synthesize neutral complexes from 4-methyl-benzo-[2,3]-thiophene and dibenzothiophene, by reducing their cationic pentamethylcyclopentadienyl complexes of iridium with an aluminum hydride. The products were expected as **I** : $C_9H_{10}S\text{-}Ir\text{-}[C_5(CH_3)_5]$ and **II** : $C_{12}H_{10}S\text{-}Ir\text{-}[C_5(CH_3)_5]$. They were expected to form by the association of the Ir *d*-orbitals with the whole *p*-system of the complexing benzo-group, hence implying that all carbon atoms in this group would remain aromatic, i.e., have $sp^2$ character.

However, X-ray diffraction results indicated that for both **I** and **II** the solid state products formed can be best described in terms of complexes in which two carbon atoms of a benzo - group of the ligand have been converted from $sp^2$ to $sp^3$ character, due possibly to over reduction of the complexes.

In order to confirm the X-ray structural results, molecular mechanics calculations were employed to generate the corresponding $sp^2$ and $sp^3$ configurations of both complexes and compare their minimized total energies.

# X-RAY STRUCTURE DETERMINATIONS

The complexes **I** and **II** were repeatedly recrystallized from hexane solution (with trace amount of dimethylchloride); the final crystallization was carried out at low temperature (- 80°C) with slow evaporation of the solvent. Yellow, transparent, parallelepipedonal crystals of complex **I** formed, while the crystals of complex **II** formed as prisms.

For each complex, a crystal of approximate dimensions 0.3 × 0.4 × 0.5 mm was mounted on a glass fiber. As the complexes are not very stable, a thin layer of epoxy coating was spread over the entire surface of the crystal, isolating it from the atmosphere. Then the fiber was attached to a goniometer head and the whole assembly was put into a refrigerator until the epoxy had firmly hardened.

All measurements were made at low temperature, - 80°C, on a RIGAKU AFC6 diffractometer with graphite - monochromated Mo $K\alpha$ radiation and a 12KW rotating anode generator. Using a search procedure, 25 reflections were selected within the range of $14° < 2\theta < 50°$ and centered carefully. Indices for these reflections were obtained from an automatic indexing program INDEX and cell parameters were determined using 13 high angle $(25° < 2\theta < 35°)$ reflections and their Friedel counterparts.

5715 reflections were measured for complex **I** and 6223 for complex **II** using the $\omega$ - $2\theta$ scan technique. 2740 out of the measured 5715 reflections for complex **I**, and 4000 out of 6223 for complex **II**, were considered to be "observed" reflections with $I > 3\sigma(I)$. After averaging, 2585 reflections for complex **I** and 3632 reflections for complex **II** remained and were used for subsequent structure determination. The space group was uniquely determined to be **I** : $P2_1/a$ and **II** : $P2_1/n$, from conditions limiting possible reflections: **I** : (h0l, h=2n; 0k0, k=2n) and **II** : (h0l, h+l=2n; 0k0, k=2n). Further experimental details are given in Tables II .1 and II .2.

The structures were solved by direct methods and refined by full matrix least square refinement to a conventional residual indices of $R = 5.1\%$, $R_w = 6.8\%$ for **I** and $R = 5.3\%$, $R_w = 7.1\%$ for **II** respectively, which are defined as

$$R = \frac{\sum_{i=1}^{n} \left| |F_o| - |F_c| \right|}{\sum_{i=1}^{n} |F_o|} \quad ; \qquad R_w = \sqrt{\frac{\sum_{i=1}^{n} w(|F_o| - |F_c|)^2}{\sum_{i=1}^{n} w|F_o|^2}}$$

$$where \quad w = \frac{1}{\sigma^2(|F_o|)}$$

The final positional and equivalent isotropic thermal parameters, the bond distances and the bond angles are given in Tables II .3-II .8; The ORTEP[1] drawings of the molecules are shown in Fig. II .1 and Fig. II .2. Tables II .9 and II .10 contain the anisotropic temperature factors for the atoms.

TABLE II.1 Crystallographic Data for Complex I.

| | |
|---|---|
| Empirical Formula | $C_{19}H_{25}S$ Ir |
| Formula Weight | 477.67 |
| Crystal System | Monoclinic |
| Lattice Parameters: | a = 10.786 (4)Å |
| | b = 10.039 (10)Å |
| | c = 15.214 (4)Å |
| | $\beta$ = 100.26° (2) |
| | V = 1782 (2) $Å^3$ |
| Space Group | P $2_1$/a (#14) |
| Z value | 4 |
| $D_{calc}$ | 1.77 $g/cm^3$ |
| $F_{000}$ | 920 |
| $\mu$ (Mo K$\alpha$) | 80.49 $cm^{-1}$ (correction applied) |
| Diffractometer | Rigaku AFC6 |
| Radiation | Mo K$\alpha$ ($\lambda$ = 0.71069Å) Graphite monochromated |
| Temperature | - 80°C |
| $2\theta_{max}$ | 60.0° |
| No. Observations | 2585 ($I > 3.00\sigma(I)$) |
| No. Variables | 190 |
| Residuals: R; $R_w$[§] | 0.051; 0.068 |
| Goodness of Fit Indicator[†] | 1.57 |
| Max. Shift in Final Cycle | 0.02 |

§ definition of R and $R_w$, see text.

† goodness of fit indicator is defined as:

$$\sqrt{\frac{\sum_{i=1}^{n} w(|F_o| - |F_c|)^2}{(N_{observed} - N_{parameters})}} ; \qquad where\ w = \frac{1}{\sigma^2(|F_o|)}$$

TABLE II .2 Crystallographic Data for Complex **II**.

| | |
|---|---|
| Empirical Formula | $C_{22}H_{25}S$ Ir |
| Formula Weight | 513.70 |
| Crystal System | Monoclinic |
| Lattice Parameters: | a = 8.62 (7)Å |
| | b = 10.37 (2)Å |
| | c = 20.954 (8)Å |
| | $\beta$ = 92.6° (1) |
| | V = 1872 (13)$Å^3$ |
| Space Group | P $2_1$/n (#14) |
| Z value | 4 |
| $D_{calc}$ | 1.82 $g/cm^3$ |
| $F_{000}$ | 992 |
| $\mu$ (Mo K$\alpha$) | 76.73 $cm^{-1}$ (correction applied) |
| Diffractometer | Rigaku AFC6 |
| Radiation | Mo K$\alpha$ ($\lambda$ = 0.71069Å) Graphite monochromated |
| Temperature | - 80°C |
| $2\theta_{max}$ | 60.0° |
| No. Observations | 3632 ($I > 3.00\sigma(I)$) |
| No. Variables | 217 |
| Residuals: R; $R_w$[§] | 0.053; 0.071 |
| Goodness of Fit Indicator[†] | 2.05 |
| Max. Shift in Final Cycle | 0.01 |

---

[§] definition of R and $R_w$, see text.

[†] definition of goodness of fit indicator, see Table II. 1.

TABLE II .3 Positional parameters (xyz) and equivalent isotropic thermal parameters $B_{eq}$† (Å$^2$) for complex **I.**

| z | Beq | atom | x | y |
|---|---|---|---|---|
| Ir | 0.27632(5) | 0.01186(4) | 0.78330(4) | 3.12(2) |
| S | 0.4470(5) | 0.0191(4) | 0.6116(3) | 5.8(2) |
| C1 | 0.305(2) | -0.169(2) | 0.625(1) | 4.8(8) |
| C2 | 0.344(2) | -0.093(2) | 0.567(1) | 5.6(9) |
| C3 | 0.330(2) | -0.174(1) | 0.803(1) | 5.4(8) |
| C4 | 0.401(2) | -0.114(2) | 0.874(1) | 8.0(10) |
| C5 | 0.532(2) | -0.077(2) | 0.875(1) | 7.0(10) |
| C6 | 0.557(2) | -0.016(2) | 0.792(2) | 8.0(10) |
| C7 | 0.438(1) | -0.026(1) | 0.721(1) | 4.2(6) |
| C8 | 0.357(1) | -0.134(1) | 0.717(1) | 3.9(6) |
| C9 | 0.210(2) | -0.267(2) | 0.605(1) | 7.0(10) |
| C10 | 0.146(1) | 0.096(1) | 0.859(1) | 3.5(6) |
| C11 | 0.136(2) | 0.070(2) | 0.955(1) | 5.8(9) |
| C12 | 0.227(1) | 0.187(1) | 0.8309(8) | 3.1(5) |
| C13 | 0.312(2) | 0.273(1) | 0.891(1) | 5.6(8) |
| C14 | 0.202(1) | 0.190(1) | 0.7357(8) | 3.0(5) |
| C15 | 0.264(2) | 0.277(1) | 0.678(1) | 5.4(9) |
| C16 | 0.105(1) | 0.103(1) | 0.706(1) | 4.5(7) |
| C17 | 0.053(2) | 0.081(2) | 0.609(1) | 7.0(10) |
| C18 | 0.072(1) | 0.045(1) | 0.786(1) | 4.7(7) |
| C19 | -0.025(2) | -0.054(2) | 0.786(2) | 9.0(10) |
| H5A(C5) | 0.5578 | -0.0165 | 0.9287 | 4.0 |
| H5B(C5) | 0.5892 | -0.1545 | 0.8858 | 4.0 |
| H6A(C6) | 0.5799 | 0.0755 | 0.8055 | 4.0 |
| H6B(C6) | 0.6327 | -0.0591 | 0.7696 | 4.0 |

† $B_{eq} = \frac{8\pi^2}{3}\sum_{i=1}^{3}\sum_{j=1}^{3} U_{ij}a_i^* a_j^* (\vec{a}_i \cdot \vec{a}_j)$

Where the coefficients $U_{ij}$ of the anisotropic temperature factor $B_{aniso}$ expression are defined as:

$$B_{aniso} = e^{-2\pi^2(a^{*2}U_{11}h^2 + b^{*2}U_{22}k^2 + c^{*2}U_{33}l^3 + 2a^*b^*U_{12}hk + 2a^*c^*U_{13}hl + 2b^*c^*U_{23}kl)}$$

TABLE II .4 Positional parameters (xyz) and equivalent isotropic thermal parameters $B_{eq}{}^{\S}$ ($Å^2$) for complex **II**.

| atom | x | y | z | Beq |
|---|---|---|---|---|
| Ir | 0.92877(5) | 0.31468(4) | 0.65025(2) | 1.82(2) |
| S | 0.8969(5) | -0.0122(3) | 0.6317(2) | 3.3(1) |
| C1 | 0.943(1) | 0.118(1) | 0.6858(5) | 2.3(5) |
| C2 | 0.793(1) | 0.182(1) | 0.6996(5) | 2.3(4) |
| C3 | 0.815(1) | 0.296(1) | 0.7386(5) | 2.5(5) |
| C4 | 0.974(1) | 0.324(1) | 0.7504(5) | 2.7(5) |
| C5 | 1.090(2) | 0.221(1) | 0.7746(7) | 3.4(6) |
| C6 | 1.059(1) | 0.094(1) | 0.7390(7) | 3.3(6) |
| C7 | 0.696(2) | 0.020(1) | 0.6275(6) | 3.2(6) |
| C8 | 0.657(2) | 0.123(1) | 0.6675(6) | 3.0(6) |
| C9 | 0.503(2) | 0.161(1) | 0.6699(6) | 3.1(6) |
| C10 | 0.389(2) | 0.097(2) | 0.6326(8) | 4.6(8) |
| C11 | 0.428(2) | -0.005(2) | 0.5947(7) | 4.3(7) |
| C12 | 0.585(2) | -0.045(1) | 0.5901(7) | 4.1(7) |
| C13 | 0.995(2) | 0.323(1) | 0.5500(5) | 2.6(5) |
| C14 | 1.064(2) | 0.215(1) | 0.5136(6) | 4.2(7) |
| C15 | 1.087(1) | 0.413(1) | 0.5884(5) | 2.1(4) |
| C16 | 1.261(1) | 0.425(1) | 0.5948(7) | 3.8(6) |
| C17 | 0.980(2) | 0.508(1) | 0.6110(6) | 2.7(5) |
| C18 | 1.021(2) | 0.622(1) | 0.6550(6) | 3.2(6) |
| C19 | 0.827(1) | 0.473(1) | 0.5875(6) | 2.5(5) |
| C20 | 0.680(1) | 0.547(2) | 0.5995(7) | 3.8(7) |
| C21 | 0.836(1) | 0.360(1) | 0.5520(6) | 2.8(5) |
| C22 | 0.709(2) | 0.287(1) | 0.5162(7) | 4.1(7) |
| H3(C5) | 0.2039 | 0.2520 | 0.7666 | 4.0 |
| H4(C5) | 0.0787 | 0.2065 | 0.8237 | 4.0 |
| H5(C6) | 0.0154 | 0.0252 | 0.7705 | 4.0 |
| H6(C6) | 0.1625 | 0.0591 | 0.7207 | 4.0 |

§ $B_{eq}$ definition, see Table II .3.

TABLE II .5 Selected Bond Distances (Å)[†] for Complex I.

| atom | atom | distance | atom | atom | distance |
|---|---|---|---|---|---|
| Ir | C3 | 2.14(1) | Ir | C8 | 2.16(1) |
| Ir | C7 | 2.16(2) | Ir | C12 | 2.16(1) |
| Ir | C10 | 2.18(1) | Ir | C14 | 2.20(1) |
| Ir | C4 | 2.23(2) | Ir | C16 | 2.24(1) |
| Ir | C18 | 2.24(1) | S | C2 | 1.72(2) |
| S | C7 | 1.76(2) | C1 | C2 | 1.34(2) |
| C1 | C8 | 1.47(2) | C1 | C9 | 1.49(2) |
| C3 | C4 | 1.37(3) | C3 | C8 | 1.45(2) |
| C4 | C5 | 1.47(3) | C5 | C6 | 1.49(3) |
| C6 | C7 | 1.53(3) | C7 | C8 | 1.47(2) |
| C10 | C11 | 1.50(2) | C10 | C18 | 1.38(2) |
| C10 | C12 | 1.45(2) | C12 | C14 | 1.43(2) |
| C12 | C13 | 1.51(2) | C14 | C16 | 1.43(2) |
| C14 | C15 | 1.53(2) | C14 | C18 | 2.35(2) |
| C16 | C18 | 1.47(2) | C16 | C17 | 1.51(2) |
| C18 | C19 | 1.51(2) | | | |

† Estimated standard deviations in the least significant figure are given in parentheses.

### TABLE II.6 Selected Bond Distances (Å)[†] for Complex II.

| atom | atom | distance | atom | atom | distance |
|---|---|---|---|---|---|
| Ir | C1 | 2.18(1) | Ir | C2 | 2.11(1) |
| Ir | C3 | 2.14(1) | Ir | C4 | 2.12(1) |
| Ir | C13 | 2.20(1) | Ir | C15 | 2.18(1) |
| Ir | C17 | 2.22(1) | Ir | C19 | 2.26(1) |
| Ir | C21 | 2.22(1) | S | C1 | 1.79(1) |
| S | C7 | 1.76(2) | C1 | C2 | 1.49(2) |
| C1 | C6 | 1.48(2) | C2 | C3 | 1.44(2) |
| C2 | C8 | 1.46(2) | C3 | C4 | 1.42(2) |
| C4 | C5 | 1.54(2) | C5 | C6 | 1.53(2) |
| C7 | C8 | 1.41(2) | C7 | C12 | 1.39(2) |
| C8 | C9 | 1.38(2) | C9 | C10 | 1.40(2) |
| C10 | C11 | 1.37(2) | C11 | C12 | 1.42(3) |
| C13 | C14 | 1.50(2) | C13 | C15 | 1.45(2) |
| C13 | C21 | 1.43(2) | C15 | C16 | 1.50(2) |
| C15 | C17 | 1.45(2) | C17 | C18 | 1.53(2) |
| C17 | C19 | 1.43(2) | C19 | C20 | 1.51(2) |
| C19 | C21 | 1.39(2) | C21 | C22 | 1.51(2) |

---

[†] Estimated standard deviations in the least significant figure are given in parentheses.

TABLE II .7 Selected Bond Angles (°)[§] for Complex I.

| atom | atom | atom | angle | atom | atom | atom | angle |
|---|---|---|---|---|---|---|---|
| C2 | S | C7 | 91.8(8) | C2 | C1 | C8 | 111(2) |
| C1 | C2 | S | 117(1) | C4 | C3 | C8 | 113(2) |
| C3 | C4 | C5 | 123(2) | C4 | C5 | C6 | 116(2) |
| C5 | C6 | C7 | 108(2) | C8 | C7 | C6 | 120(1) |
| C8 | C7 | S | 109(1) | C6 | C7 | S | 118(1) |
| C3 | C8 | C1 | 133(2) | C3 | C8 | C7 | 115(1) |
| C1 | C8 | C7 | 112(1) | C18 | C10 | C12 | 110(1) |
| C14 | C12 | C10 | 108(1) | C12 | C14 | C16 | 107(1) |
| C14 | C16 | C18 | 108(1) | C10 | C18 | C16 | 107(1) |

[§] Estimated standard deviations in the least significant figure are given in parentheses.

TABLE II.8 Selected Bond Angles (°) § for Complex **II.**

| atom | atom | atom | angle | atom | atom | atom | angle |
|---|---|---|---|---|---|---|---|
| C7 | S | C1 | 94.5(6) | C6 | C1 | C2 | 119(1) |
| C6 | C1 | S | 118(1) | C2 | C1 | S | 107(1) |
| C3 | C2 | C8 | 133(1) | C3 | C2 | C1 | 113(1) |
| C8 | C2 | C1 | 114(1) | C4 | C3 | C2 | 112(1) |
| C6 | C5 | C4 | 110(1) | C1 | C6 | C5 | 109(1) |
| C12 | C7 | C8 | 122(1) | C12 | C7 | S | 126(1) |
| C8 | C7 | S | 112(1) | C9 | C8 | C7 | 120(1) |
| C9 | C8 | C2 | 128(1) | C7 | C8 | C2 | 112(1) |
| C8 | C9 | C10 | 120(1) | C11 | C10 | C9 | 120(2) |
| C10 | C11 | C12 | 122(1) | C7 | C12 | C11 | 117(1) |
| C21 | C13 | C15 | 108(1) | C17 | C15 | C13 | 106(1) |
| C19 | C17 | C15 | 108(1) | C21 | C19 | C17 | 109(1) |
| C19 | C21 | C13 | 109(1) | | | | |

§ Estimated standard deviations in the least significant figure are given in parentheses.

Fig. II.1 ORTEP drawing of complex I.

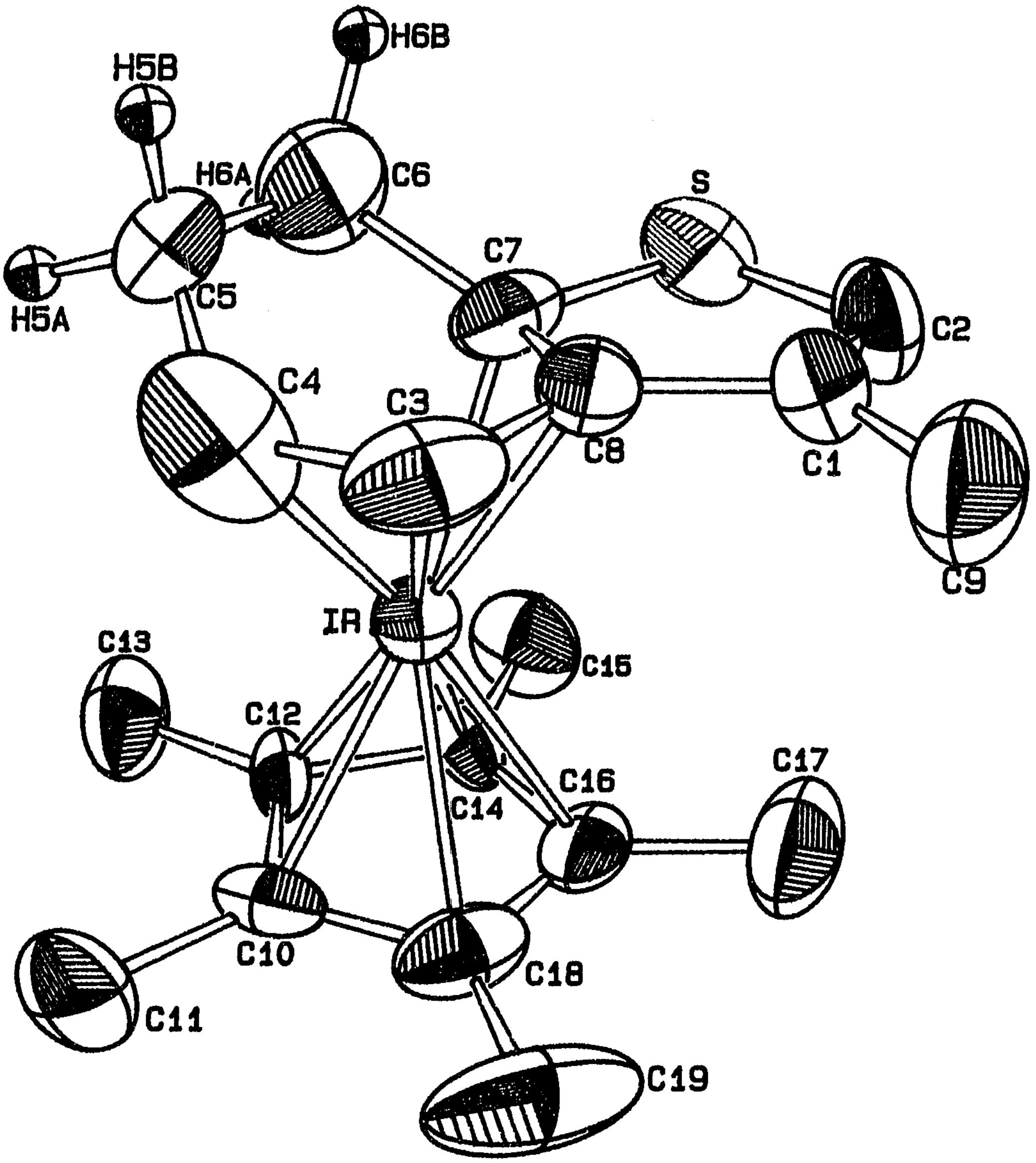

§ Other hydrogen atoms are omitted for clearness.

Fig. II .2 ORTEP drawing of complex **II**.

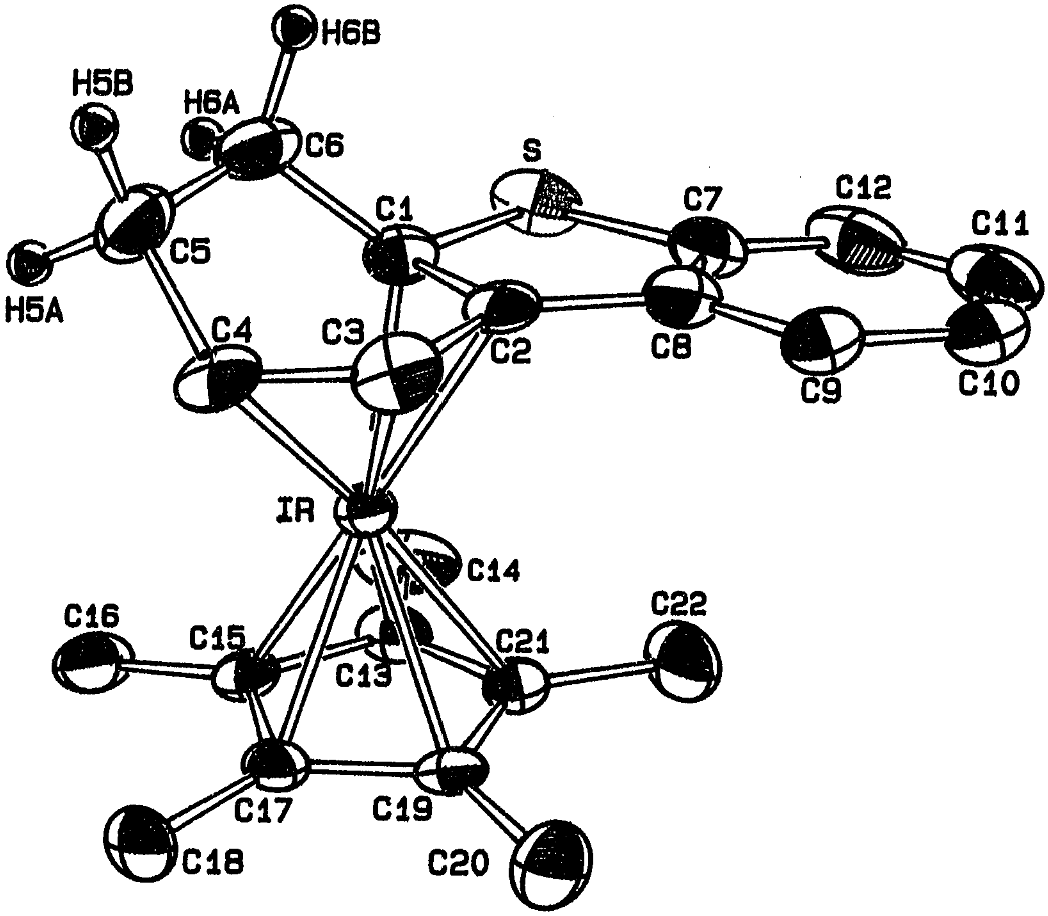

§ Other hydrogen atoms are omitted for clearness.

TABLE II .9 Anisotropic parameters $U_{ij}$ § for Complex I.

| atom | $U_{11}$ | $U_{22}$ | $U_{33}$ | $U_{12}$ | $U_{13}$ | $U_{23}$ |
|---|---|---|---|---|---|---|
| Ir | 0.0375(3) | 0.0445(3) | 0.0359(3) | 0.0067(3) | 0.0051(2) | -0.0020(3) |
| S | 0.071(3) | 0.095(3) | 0.060(3) | 0.002(3) | 0.029(2) | -0.002(3) |
| C1 | 0.034(7) | 0.055(9) | 0.07(1) | 0.006(6) | 0.001(7) | -0.001(7) |
| C2 | 0.05(1) | 0.050(8) | 0.05(1) | 0.014(7) | 0.005(7) | -0.008(7) |
| C3 | 0.06(1) | 0.040(8) | 0.11(2) | 0.018(7) | 0.01(1) | 0.007(9) |
| C4 | 0.12(2) | 0.08(1) | 0.10(2) | -0.04(1) | 0.05(1) | -0.02(1) |
| C5 | 0.05(1) | 0.16(2) | 0.06(1) | 0.03(1) | -0.01(1) | -0.02(1) |
| C6 | 0.06(1) | 0.15(2) | 0.09(2) | -0.03(1) | 0.01(1) | -0.03(1) |
| C7 | 0.08(1) | 0.10(1) | 0.031(8) | 0.02(1) | 0.002(8) | -0.010(9) |
| C8 | 0.06(1) | 0.08(1) | 0.05(1) | 0.010(8) | 0.004(8) | -0.020(8) |
| C9 | 0.09(1) | 0.08(1) | 0.07(1) | -0.01(1) | -0.01(1) | -0.03(1) |
| C13 | 0.045(8) | 0.055(8) | 0.018(6) | -0.003(6) | 0.001(5) | -0.001(5) |
| C14 | 0.09(1) | 0.07(1) | 0.05(1) | 0.00(1) | -0.00(1) | -0.018(8) |
| C15 | 0.036(8) | 0.049(8) | 0.05(1) | 0.009(6) | 0.024(7) | 0.007(7) |
| C16 | 0.08(1) | 0.09(1) | 0.05(1) | -0.00(1) | 0.03(1) | 0.02(1) |
| C17 | 0.036(8) | 0.043(8) | 0.10(1) | 0.005(6) | 0.007(9) | -0.010(8) |
| C18 | 0.05(1) | 0.07(1) | 0.23(3) | -0.02(1) | 0.04(2) | -0.02(2) |
| C19 | 0.036(8) | 0.07(1) | 0.06(1) | 0.024(7) | -0.006(7) | -0.026(8) |
| C20 | 0.08(1) | 0.10(1) | 0.09(1) | 0.02(1) | -0.02(1) | -0.04(1) |
| C21 | 0.054(9) | 0.043(7) | 0.021(6) | 0.002(6) | 0.014(6) | 0.005(5) |
| C22 | 0.08(1) | 0.07(1) | 0.06(1) | 0.00(1) | 0.03(1) | 0.019(9) |

§ The coefficients $U_{ij}$ of the anisotropic temperature factor $B_{aniso}$ expression are defined as:

$$B_{aniso} = e^{-2\pi^2 (a^{*2} U_{11} h^2 + b^{*2} U_{22} k^2 + c^{*2} U_{33} l^3 + 2a^* b^* U_{12} hk + 2a^* c^* U_{13} hl + 2b^* c^* U_{23} kl)}$$

TABLE II.10 Anisotropic parameters $U_{ij}$ § for Complex II.

| atom | $U_{11}$ | $U_{22}$ | $U_{33}$ | $U_{12}$ | $U_{13}$ | $U_{23}$ |
|---|---|---|---|---|---|---|
| Ir | 0.0270(2) | 0.0212(2) | 0.0209(2) | 0.0009(2) | -0.0002(1) | 0.0019(2) |
| S | 0.062(2) | 0.027(2) | 0.039(2) | 0.003(2) | 0.018(2) | -0.004(1) |
| C1 | 0.036(6) | 0.034(7) | 0.020(6) | 0.000(5) | 0.007(5) | 0.005(5) |
| C2 | 0.039(6) | 0.032(6) | 0.018(5) | -0.000(6) | 0.003(4) | 0.011(5) |
| C3 | 0.048(7) | 0.033(7) | 0.013(5) | 0.008(6) | 0.006(5) | -0.012(5) |
| C4 | 0.049(7) | 0.042(7) | 0.010(4) | 0.003(6) | 0.001(4) | 0.006(5) |
| C5 | 0.041(7) | 0.043(8) | 0.042(8) | 0.008(6) | -0.011(6) | 0.004(6) |
| C6 | 0.035(7) | 0.046(8) | 0.045(8) | 0.012(6) | 0.004(6) | 0.021(7) |
| C7 | 0.049(8) | 0.035(8) | 0.039(8) | -0.009(6) | 0.000(6) | 0.011(6) |
| C8 | 0.045(8) | 0.027(7) | 0.040(7) | -0.003(6) | -0.003(6) | 0.007(6) |
| C9 | 0.043(7) | 0.040(8) | 0.032(7) | -0.003(6) | -0.005(5) | 0.012(6) |
| C10 | 0.06(1) | 0.05(1) | 0.06(1) | -0.013(8) | -0.024(8) | 0.031(9) |
| C11 | 0.08(1) | 0.05(1) | 0.030(7) | -0.031(9) | -0.014(7) | 0.012(7) |
| C12 | 0.09(1) | 0.030(7) | 0.040(8) | -0.016(8) | 0.005(8) | -0.001(6) |
| C13 | 0.051(7) | 0.023(6) | 0.024(6) | 0.001(6) | 0.002(5) | -0.004(5) |
| C14 | 0.10(1) | 0.039(8) | 0.028(7) | 0.010(8) | 0.022(7) | 0.003(6) |
| C15 | 0.034(6) | 0.027(6) | 0.019(5) | 0.002(5) | 0.001(4) | 0.007(4) |
| C16 | 0.030(7) | 0.046(9) | 0.07(1) | 0.002(6) | 0.003(6) | 0.028(8) |
| C17 | 0.049(7) | 0.023(6) | 0.028(6) | -0.008(5) | -0.013(5) | 0.009(5) |
| C18 | 0.063(9) | 0.027(7) | 0.029(7) | -0.010(6) | -0.015(6) | -0.007(5) |
| C19 | 0.033(6) | 0.021(6) | 0.041(7) | 0.004(5) | -0.003(5) | 0.013(5) |
| C20 | 0.030(7) | 0.052(9) | 0.06(1) | 0.005(7) | 0.003(6) | 0.009(8) |
| C21 | 0.038(7) | 0.033(6) | 0.033(7) | -0.006(6) | -0.007(5) | 0.013(5) |
| C22 | 0.07(1) | 0.05(1) | 0.039(8) | -0.020(8) | -0.015(7) | -0.001(6) |

§ Definition for $U_{ij}$, see Table II.9

In structure **I**, the C4 - C5, C5 - C6 and C6 - C7 bond distances (1.52 ~ 1.55 Å), the bond angles at C5 and C6 (110°), and the deviation of C5 and C6 from the least squares plane defined by C3, C4, C7 and C8 (0.97 Å and 0.85 Å respectively, see Table II.11), all indicate that C5 and C6 are hydrogenated to be methylene carbons rather than phenyl carbons.

Similarly in structure **II**, the C4 - C5, C5 - C6 and C6 - C1 bond distances (1.48 ~ 1.45 Å), the bond angles at C5 and C6 (*ca.* 110°), and the deviation of C5 and C6 from the least squares plane defined by S, C1, C2, C3 and C4 (0.93 Å and 1.11 Å respectively, see Table II.12), also indicate the two carbon atoms, C5 and C6, are hydrogenated to be metylene carbons rather than phenyl carbons.

Solution $^1$H NMR spectra also showed that for **I** there were high-field multiplets (δ 1.74 and 1.56 ppm) in addition to the intermediate signals located at δ 2.76 and 4.77 ppm for the hydrogen atoms associated with the former phenyl ring carbons of the benzothiophene, which now apparently have a diene character; and the low-field signal (δ 6.19 ppm) for the hydrogen atoms associated to the carbon atoms of the thiophene which is uncoordinated with the Ir atom.

Also, for **II** there were high-field multiplets (δ 1.88 and 1.50 ppm) in addition to the intermediate signals located at δ 2.99 and 5.30 ppm for the hydrogen atoms associated with the carbons coordinated with the Ir atom; and the low-field quartet signals (δ 7.53, 7.39, 7.18 and 7.08 ppm) for the hydrogen atoms associated

| Atoms Defining Plane | Distance(Å) | esd(Å) |
|---|---|---|
| C7 | - 0.0178 | 0.0139 |
| C8 | 0.0342 | 0.0139 |
| C3 | - 0.0475 | 0.0164 |
| C4 | 0.0438 | 0.0212 |

(Mean deviation from plane is 0.0358 Å)

| Additional Atoms | Distance (Å) |
|---|---|
| C5 | 0.9031 |
| C6 | 0.8253 |

Table II.12 A Least - Squares Plane in Complex II.

| Atoms Defining Plane | Distance(Å) | esd(Å) |
|---|---|---|
| S | 0.0074 | 0.0037 |
| C1 | - 0.1076 | 0.0119 |
| C2 | - 0.0225 | 0.0117 |
| C3 | 0.0099 | 0.0120 |
| C4 | 0.0526 | 0.0127 |

(Mean deviation from plane is 0.0400 Å)

| Additional Atoms | Distance (Å) |
|---|---|
| C5 | - 0.9290 |
| C6 | - 1.1070 |

with the carbon atoms of the other aromatic ring in the dibenzothiophene which is uncoordinated with the Ir atom.

These high-field signals indicated that there were carbon atoms in the benzothiophene or dibenzothiophene group which have a different chemical environment from those of the other carbon atoms in the compounds.

Although in both cases, it was not possible from a difference electron density map to verify the presence of two hydrogen atoms attached to each of these carbons, it was found that, in both structures, an elimination of one hydrogen atom from C5 and C6 respectively caused the R - factor to increase by *ca.* 0.1% after least squares refinement, which also indicated that C5 and C6 are methylene carbons.

In order to obtain additional evidence for the reasonableness of the postulate that the benzo-groups of both I and II were over reduced such that the two carbon atoms, C5 and C6, had been converted from $sp^2$ to $sp^3$ character, as the above evidences had suggested, molecular mechanics calculations were carried out.

# MOLECULAR MECHANICS MODELING

## General Description

Molecular mechanics[2] is a calculational method designed to give accurate *a priori* structures and energies for molecules. It is based on the ideas that there are bonds between atoms in molecules and there are Van der Waals forces between non-bonded atoms, that bonds have "natural" lengths and angles, and that molecules will adjust their geometries so as to take up these values of bond lengths and angles in simple cases. It also employs the fundamental formulations of vibrational spectroscopy.

In practice, molecular mechanics calculations employ an empirically derived set of equations for the Born-Oppenheimer surface, which is the multi-dimensional "surface" that describes the energy of the molecule in terms of the nuclear positions. This set of potential functions is called the **force field** and contains adjustable parameters that are optimized to obtain the best fit of calculated and experimental properties of the molecules, such as geometries, conformational energies, heats of formation, or other properties. It is also assumed that corresponding parameters and force constants may be transferred from one molecule to another, i.e., these quantities are evaluated for a set of compounds and thereafter the values are fixed and can be used for other similar compounds. In the ordinary case, the force field is established by certain sets of equations, and the adjustable parameters are optimized.

Simple molecular mechanics force fields include bond stretching, angle bending, torsion, and Van de Waals interactions in their make-up,

$$V = \sum V_{stretch} + \sum V_{bend} + \sum V_{torsion} + \sum V_{VdW} \tag{1}$$

where the summations extend over all bonds, bond angles, torsion angles, and non-bonded interactions between all atoms not bound to each other or to a common atom (i.e., 1,4-interactions and higher).

When a molecule with $n$ atoms, which are defined in terms of $3n$ coordinates $x_i$, is deformed from its geometry of minimum potential energy $V_0$, and coordinates $x_0$ , the potential energy may be written in a Taylor series expansion as:

$$\begin{aligned} V_{potential} = V_0 + \sum_{i=1}^{3n} \left( \frac{\partial V}{\partial x_i} \right)_0 \Delta x_i + \frac{1}{2!} \sum_{i,j=1}^{3n} \left( \frac{\partial^2 V}{\partial x_i \partial x_j} \right)_0 \Delta x_i \Delta x_j \\ + \frac{1}{3!} \sum_{i,j,k=1}^{3n} \left( \frac{\partial^3 V}{\partial x_i \partial x_j \partial x_k} \right)_0 \Delta x_i \Delta x_j \Delta x_k + \ldots \textit{(higher terms)} \end{aligned} \tag{2}$$

In a vibrational analysis of a molecule having a geometry corresponding to a potential energy minimum, the first term $V_0$ is taken as zero. Also the second term vanishes at this geometry due to the nullification of the first derivative by the definition of the potential minimum. If the displacements of the vibration are sufficiently small, the fourth and the "higher terms" in (2) can be neglected (harmonic approximation[4-6]).

The second derivatives in the third term are called the force constants, which are arranged in the form of a matrix, the terms with $i = j$ being diagonal, and the cross-terms with $i \neq j$ being off-diagonal. Denoting the force constants

$$f_{ij} \equiv \left( \frac{\partial^2 V}{\partial x_i \partial x_j} \right)_0$$

the potential energy in a harmonic force field is simply

$$V_{potential} = \frac{1}{2} \sum_{i,j=1}^{3n} f_{ij}\, \Delta x_i \Delta x_j \tag{3}$$

If the **valence force field** is adopted, which best fits ordinary chemical ideas about the nature of the forces acting in a molecule, all the off-diagonal force constants are neglected. This results, in terms of the equilibrium bond lengths $r$, bond angles $\theta$, and torsion angles $\tilde{\omega}$, in a force field with a Hooke's law harmonic potential

$$\begin{aligned} V_{harmonic} = {} & \frac{1}{2} \sum_i f_{r,i} \,( r_i - r_i^0 )^2 + \frac{1}{2} \sum_k f_{\theta,k} \,( \theta_k - \theta_k^0 )^2 \\ & + \frac{1}{2} \sum_l f_{\omega,l} \,( \omega_l - \omega_l^0 )^2 \end{aligned} \tag{4}$$

where the first term in (4) accounts for the bond stretching, the second term for the bending, and the third term for the torsion.

However, considering there may be non-negligible deformation of the "natural" molecule during the molecular modeling, the **molecular mechanics force fields** recruits the cubic term of (2), which result in the potential energies of the stretching, bending, torsion and Van der Waals being expressed as follows, respectively:

$$
\begin{aligned}
V_{stretch} &= \frac{1}{2}\sum_i f_{r,i}\,(r_i - r_i^0)^2 + f'_{r,i}\,(r_i - r_i^0)^3 \\
V_{bend} &= \frac{1}{2}\sum_k f_{\theta,k}\,(\theta_k - \theta_k^0)^2 + f'_{\theta,k}(\theta_k - \theta_k^0)^3 \\
V_{torsion} &= \frac{1}{2}\sum_j V_j\,[1 - \cos(j\omega)] \\
V_{VdW} &= \frac{\epsilon}{1 - 6/\alpha}\left[\frac{6}{\alpha}\exp\left(\frac{\alpha}{1 - r/r_0}\right) - \left(\frac{r_0}{r}\right)^6\right]
\end{aligned}
\qquad (5)
$$

The form of $V_{VdW}$ is subject to the situation under which the torsion occurs. All the functions in (5) are parameterized based on the vibrational spectroscopic data, and undergo least squares refinement on the parameters, $k_j$, with respect to the data $y_i$ :

$$y_i\,(improved) = y_i\,(initial) + \sum_{j=1}^{k} \frac{\partial y_i}{\partial k_j}\,\delta k_j$$

## Results and Discussion

Both structures were modeled using a molecular mechanics program[3]. In each case calculations were done first assuming carbons C5 and C6 to be methylenic and then aromatic. The results obtained are shown in Figures II .3–II .6. For I, the aromatic configuration has a converged energy - 86.309 kCal whereas the aliphatic

Figure II.3 Molecular mechanics refinement for I, assuming carbons C5 and C6 to be aromatic.

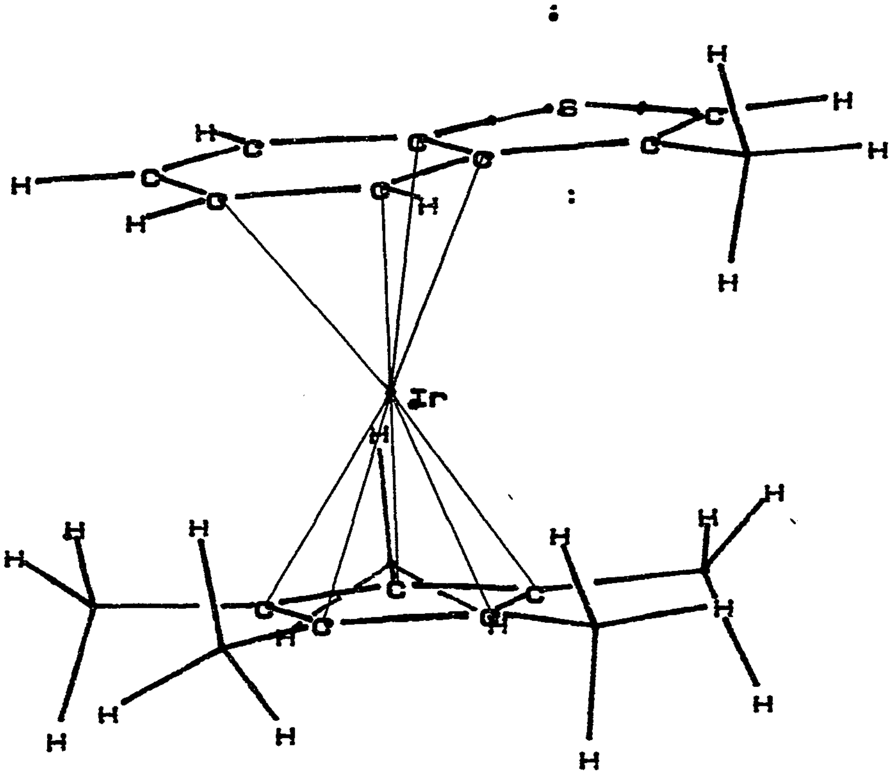

```
MMX ENERGY  -86.309 kCal
STR      .30  BEND   14.57  S-B    -.21  TOR   11.38
VDW -112.67  DIP      .32    DIPOLE MOMENT  2.0082
Heat of Formation   -90.804  Strain energy   -87.749
```

Figure II.4 Molecular mechanics refinement for I, assuming carbons C5 and C6 to be aliphatic.

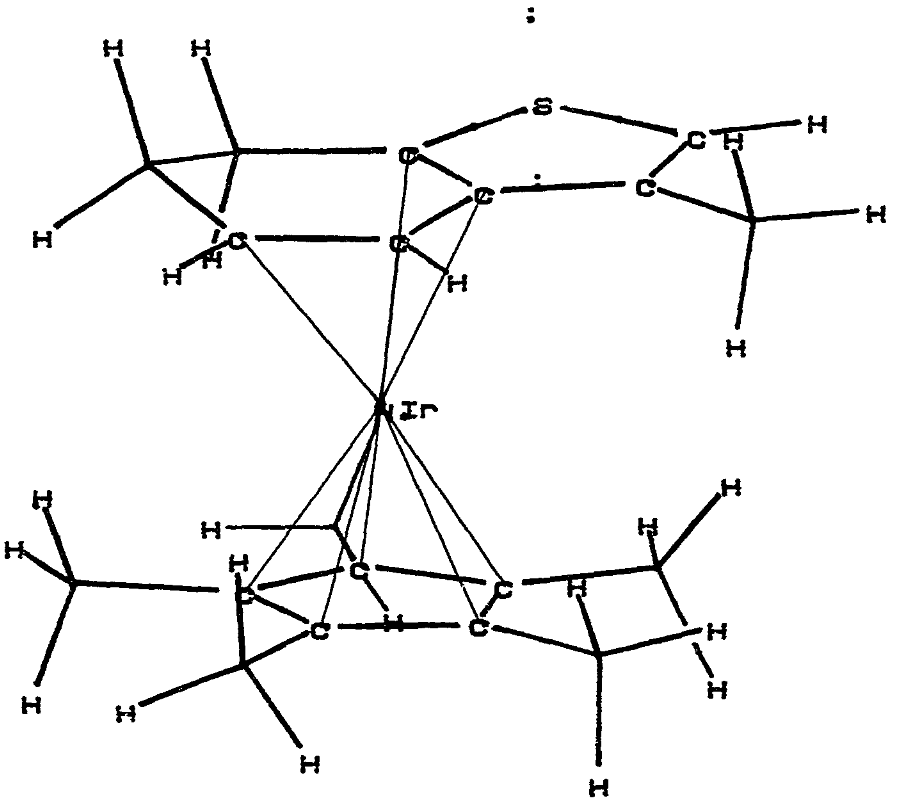

```
MMX ENERGY  -88.301 kCal
STR      .34  BEND   14.91  S-B    -.17  TOR   10.83
VDW -113.93  DIP    -.28    DIPOLE MOMENT  2.2198
Heat of Formation  -112.670  Strain energy   -90.561
```

Figure II.5 Molecular mechanics refinement for II, assuming carbons C5 and C6 to be aromatic.

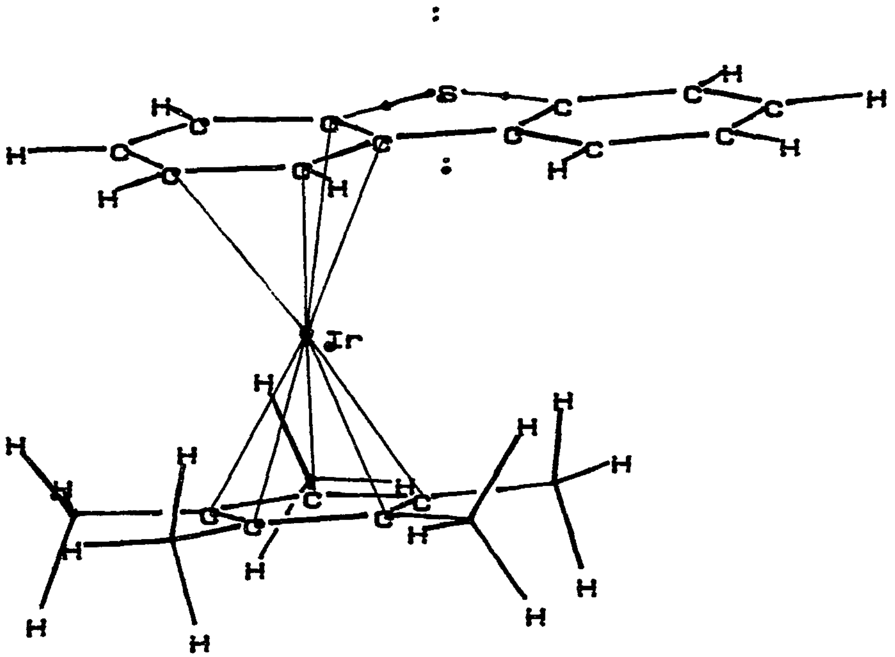

```
MMX ENERGY  -72.205 kCal
STR      .31  BEND   15.13  S-B    -.20  TOR   21.38
VDW -110.85  DIP    2.08    DIPOLE MOMENT  2.1802
Heat of Formation   -53.870  Strain energy   -73.405
```

Figure II.6 Molecular mechanics refinement for II, assuming carbons C5 and C6 to be aliphatic.

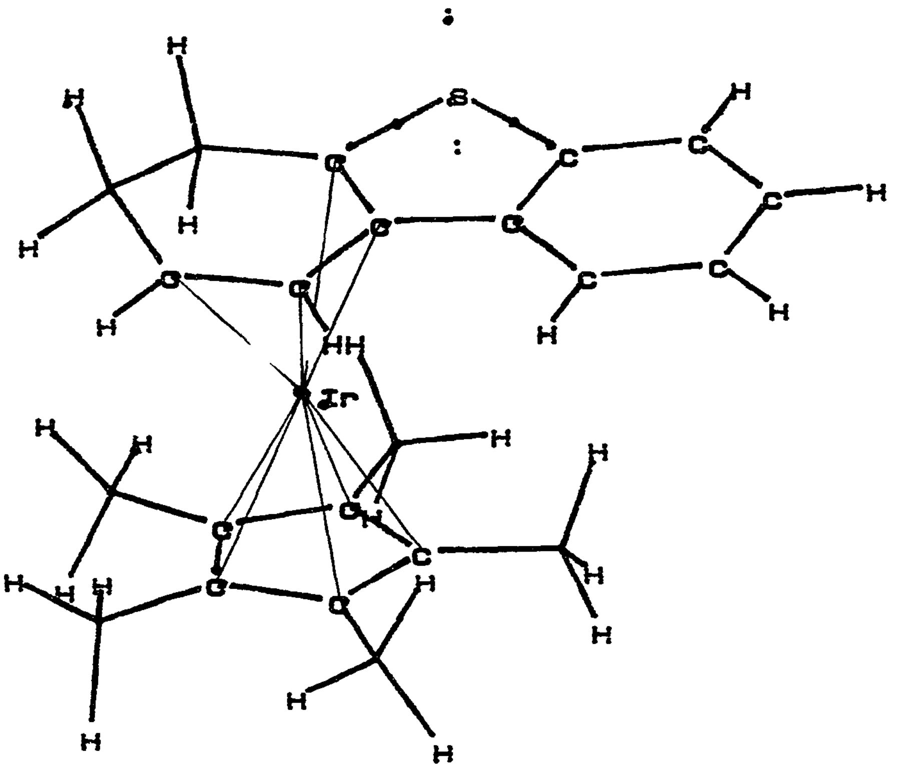

```
MMX ENERGY  -75.513 kCal
STR       .37   BEND    15.51   S-B     -.17   TOR    19.56
VDW -112.21   DIP     1.43    DIPOLE MOMENT  2.4123
Heat of Formation   -77.052  Strain energy   -77.533
```

configuration has - 88.301 kCal; For **II**, it was - 72.205 kCal of the aromatic against - 75.513 kCal of the aliphatic configuration. Those indicate that the aliphatic configurations are more stable.

Tables II .13 and II .14 compare bond distances for the X-ray results and the molecular mechanics calculation assuming C5 and C6 to be aliphatic and aromatic respectively in structures I and II; and in Tables II .15 and II .16 for the bond angles. In terms of bond lengths, one can see from Tables II .13 and II .14, for bonds not involving C5 and C6, $\delta_A$'s (the difference between the molecular mechanics calculation, in which C5 and C6 were assumed **aliphatic**, and the X-ray results) are all comparable with $\delta_B$'s (a similar quantity, but C5 and C6 were assumed **aromatic**). However, for those bonds involving C5 and C6, $\delta_B$'s are all much greater than $\delta_A$'s. [For three bonds of this kind, the average of the absolute length difference value, $\Delta_B$ is 0.09 Å *vs.* that of $\Delta_A$ being 0.04 Å for I; and $\Delta_B$ is 0.11 Å *vs.* that of $\Delta_A$ being 0.02 Å for II]. Similarly, in Tables II .15 and II .16, one can see the same thing happens to the bond angles involving C5 and C6, i.e., $\Delta_B = 7°$ *vs.* $\Delta_A = 3°$ for I; $\Delta_B = 9.5°$ *vs.* $\Delta_A = 4.5°$ for II.

TABLE II.13 Comparison of Bond lengths (Å) for **I** with those obtained from molecular mechanics calculations with C5 and C6 as Aliphatic (A) and Aromatic (B).

| atom | atom | X-ray | A | $\delta_A$[§] | B | $\delta_B$ |
|---|---|---|---|---|---|---|
| Ir | C1 | 2.16(2) | 2.32 | 0.16 | 2.30 | 0.14 |
| Ir | C2 | 2.16(1) | 2.06 | -0.10 | 2.02 | -0.14 |
| Ir | C3 | 2.14(1) | 2.02 | -0.12 | 2.04 | -0.10 |
| Ir | C4 | 2.23(2) | 2.29 | 0.06 | 2.34 | 0.11 |
| Ir | C13 | 2.16(1) | 2.07 | -0.09 | 2.06 | -0.10 |
| Ir | C15 | 2.18(1) | 2.08 | -0.10 | 2.05 | -0.13 |
| Ir | C17 | 2.24(1) | 2.07 | -0.17 | 2.05 | -0.19 |
| Ir | C19 | 2.24(1) | 2.06 | -0.18 | 2.06 | -0.18 |
| Ir | C21 | 2.20(1) | 2.06 | -0.14 | 2.05 | -0.15 |
| Δ[†] for Ir-C bonds | | | $\Delta_A = 0.12_4$ | | $\Delta_B = 0.13_8$ | |
| S | C1 | 1.76(2) | 1.77 | 0.01 | 1.77 | 0.01 |
| S | C7 | 1.72(2) | 1.77 | 0.05 | 1.77 | 0.05 |
| Δ for S-C bonds | | | $\Delta_A = 0.03$ | | $\Delta_B = 0.03$ | |
| C1 | C2 | 1.47(2) | 1.40 | -0.07 | 1.40 | -0.07 |
| C3 | C2 | 1.45(2) | 1.40 | -0.05 | 1.40 | -0.05 |
| C3 | C4 | 1.37(3) | 1.40 | 0.03 | 1.41 | 0.04 |
| C8 | C2 | 1.47(2) | 1.41 | -0.06 | 1.41 | -0.06 |
| C8 | C7 | 1.34(2) | 1.41 | 0.07 | 1.41 | 0.07 |
| C8 | C9 | 1.49(2) | 1.50 | 0.01 | 1.50 | 0.01 |
| C13 | C14 | 1.51(2) | 1.50 | -0.01 | 1.50 | -0.01 |
| C13 | C21 | 1.43(2) | 1.41 | -0.02 | 1.41 | -0.02 |

---

[§] δ is the difference between the molecular mechanics result and that of the X-ray investigation.

[†] Δ is the average of the absolute value of δ, i.e., Δ is defined as

$$\Delta = \frac{\sum_{i=1}^{n} |\delta_i|}{n}$$

TABLE II .13 (Continued)

| atom | atom | X-ray | A | $\delta_A$[§] | B | $\delta_B$ |
|---|---|---|---|---|---|---|
| C15 | C13 | 1.45(2) | 1.41 | - 0.04 | 1.41 | - 0.04 |
| C15 | C16 | 1.50(2) | 1.50 | 0.00 | 1.50 | 0.00 |
| C15 | C17 | 1.38(2) | 1.41 | 0.04 | 1.41 | 0.04 |
| C19 | C17 | 1.47(2) | 1.41 | - 0.06 | 1.41 | - 0.06 |
| C19 | C20 | 1.51(2) | 1.50 | - 0.01 | 1.50 | - 0.01 |
| C21 | C19 | 1.43(2) | 1.41 | - 0.02 | 1.41 | - 0.02 |
| C21 | C22 | 1.53(2) | 1.50 | - 0.03 | 1.50 | - 0.03 |
| Δ for bonds NOT involving C5 and C6 | | | $\Delta_A = 0.03_5$ | | $\Delta_B = 0.03_5$ | |
| C4 | C5 | 1.47(3) | 1.51 | 0.04 | 1.41 | - 0.06 |
| C5 | C6 | 1.49(3) | 1.53 | 0.04 | 1.41 | - 0.08 |
| C6 | C1 | 1.53(3) | 1.50 | - 0.03 | 1.40 | - 0.13 |
| Δ for bonds involving C5 and C6 | | | $\Delta_A = 0.03_7$ | | $\Delta_B = 0.09_0$ | |

TABLE II.14 Comparison of Bond lengths (Å) for **II** with those obtained from molecular mechanics calculations with C5 and C6 as Aliphatic (A) and Aromatic (B).

| atom | atom | X-ray | A | $\delta_A$§ | B | $\delta_B$ |
|---|---|---|---|---|---|---|
| Ir | C2 | 2.11(1) | 2.04 | -0.07 | 2.02 | -0.09 |
| Ir | C4 | 2.12(1) | 2.30 | 0.18 | 2.33 | 0.21 |
| Ir | C3 | 2.14(1) | 2.01 | -0.13 | 2.04 | -0.10 |
| Ir | C1 | 2.18(1) | 2.32 | 0.14 | 2.30 | 0.12 |
| Ir | C15 | 2.18(1) | 2.07 | -0.11 | 2.06 | -0.12 |
| Ir | C13 | 2.20(1) | 2.07 | -0.13 | 2.07 | -0.13 |
| Ir | C17 | 2.22(1) | 2.06 | -0.16 | 2.05 | -0.17 |
| Ir | C21 | 2.22(1) | 2.06 | -0.16 | 2.06 | -0.16 |
| Ir | C19 | 2.26(1) | 2.06 | -0.20 | 2.05 | -0.21 |
| Δ† for Ir-C bonds | | | $\Delta_A = 0.14_2$ | | $\Delta_B = 0.14_5$ | |
| S | C7 | 1.76(2) | 1.77 | 0.01 | 1.77 | 0.01 |
| S | C1 | 1.79(1) | 1.77 | -0.02 | 1.77 | -0.02 |
| Δ for S-C bonds | | | $\Delta_A = 0.01_5$ | | $\Delta_B = 0.01_5$ | |
| C1 | C2 | 1.49(2) | 1.41 | -0.08 | 1.41 | -0.08 |
| C2 | C3 | 1.44(2) | 1.40 | -0.04 | 1.40 | -0.04 |
| C2 | C8 | 1.46(2) | 1.41 | -0.05 | 1.41 | -0.05 |
| C3 | C4 | 1.42(2) | 1.40 | -0.02 | 1.41 | -0.01 |
| C7 | C12 | 1.39(2) | 1.40 | 0.01 | 1.40 | 0.01 |
| C7 | C8 | 1.41(2) | 1.40 | -0.01 | 1.41 | 0.00 |
| C8 | C9 | 1.38(2) | 1.40 | 0.02 | 1.40 | 0.02 |
| C9 | C10 | 1.40(2) | 1.41 | 0.01 | 1.41 | 0.01 |
| C10 | C11 | 1.37(2) | 1.41 | 0.04 | 1.41 | 0.04 |
| C11 | C12 | 1.42(3) | 1.40 | -0.02 | 1.41 | -0.01 |
| C13 | C21 | 1.43(2) | 1.41 | -0.02 | 1.41 | -0.02 |
| C13 | C15 | 1.45(2) | 1.41 | -0.04 | 1.41 | -0.04 |
| C13 | C14 | 1.50(2) | 1.50 | 0.00 | 1.50 | 0.00 |

---

§ δ is the difference between the molecular mechanics result and that of the X-ray investigation.

† definition of Δ see Table II.13.

TABLE II .14 (Continued)

| atom | atom | X-ray | A | $\delta_A$§ | B | $\delta_B$ |
|---|---|---|---|---|---|---|
| C15 | C17 | 1.45(2) | 1.41 | -0.04 | 1.41 | -0.04 |
| C15 | C16 | 1.50(2) | 1.50 | 0.00 | 1.50 | 0.00 |
| C17 | C19 | 1.43(2) | 1.41 | -0.02 | 1.41 | -0.02 |
| C17 | C18 | 1.53(2) | 1.50 | -0.03 | 1.50 | -0.03 |
| C19 | C21 | 1.39(2) | 1.41 | 0.02 | 1.41 | 0.02 |
| C19 | C20 | 1.51(2) | 1.50 | -0.01 | 1.50 | -0.01 |
| C21 | C22 | 1.51(2) | 1.50 | -0.01 | 1.50 | -0.01 |
| Δ for bonds NOT involving C5 and C6 | | | $\Delta_A = 0.01_5$ | | $\Delta_B = 0.01_3$ | |
| | | | | | | |
| C1 | C6 | 1.48(2) | 1.50 | 0.02 | 1.40 | -0.08 |
| C4 | C5 | 1.54(2) | 1.51 | -0.03 | 1.41 | -0.13 |
| C5 | C6 | 1.53(2) | 1.53 | 0.00 | 1.40 | -0.13 |
| Δ for bonds involving C5 and C6 | | | $\Delta_A = 0.01_6$ | | $\Delta_B = 0.11_3$ | |

TABLE II .15 Comparison of Bond Angles (°) for I with those obtained from molecular mechanics calculations with C5 and C6 as Aliphatic (A) and Aromatic (B).

| atom | apex | atom | X-ray | A | $\delta_A$[§] | B | $\delta_B$ |
|---|---|---|---|---|---|---|---|
| C2 | Ir | C1 | 39.9(5) | 36.8 | - 3.1 | 37.2 | - 2.7 |
| C3 | Ir | C2 | 39.5(6) | 40.1 | 0.6 | 40.3 | 0.8 |
| C3 | Ir | C4 | 36.5(6) | 37.4 | 0.9 | 36.6 | 0.1 |
| C3 | Ir | C17 | 113.3(6) | 111.2 | - 2.1 | 113.1 | - 0.2 |
| C13 | Ir | C21 | 38.2(4) | 39.6 | 1.4 | 39.8 | 1.6 |
| C15 | Ir | C17 | 36.3(6) | 39.9 | 3.6 | 40.1 | 3.8 |
| C19 | Ir | C17 | 38.2(6) | 40.0 | 1.8 | 40.1 | 1.9 |
| C21 | Ir | C17 | 63.8(5) | 67.0 | 3.2 | 67.1 | 3.3 |
| C21 | Ir | C19 | 37.6(5) | 39.8 | 2.2 | 39.8 | 2.2 |
| $\Delta$[†] for angles at Ir | | | | | $\Delta_A = 2.1$ | | $\Delta_B = 1.8$ |
| C7 | S | C1 | 91.8(8) | 90.4 | - 1.4 | 90.4 | -1.4 |
| C2 | C1 | S | 109(1) | 111 | 2 | 112 | 3 |
| C6 | C1 | S | 118(1) | 123 | 5 | 125 | 7 |
| C2 | C1 | C6 | 120(1) | 126 | 6 | 123 | 3 |
| C3 | C2 | C1 | 115(1) | 120 | 5 | 119 | 4 |
| C3 | C2 | C8 | 133(2) | 126 | - 7 | 127 | - 6 |
| C8 | C2 | C1 | 112(1) | 114 | 2 | 114 | 2 |
| C4 | C3 | C2 | 113(2) | 119 | 6 | 119 | 6 |
| C3 | C4 | C5 | 123(2) | 124 | 1 | 122 | - 1 |
| C8 | C7 | S | 117(1) | 112 | - 5 | 113 | - 4 |
| C7 | C8 | C2 | 111(2) | 112 | 1 | 112 | 1 |
| C7 | C8 | C9 | 128(2) | 123 | - 5 | 124 | - 4 |
| C2 | C8 | C9 | 121(2) | 125 | 4 | 124 | 3 |

---

[§] $\delta$ is the difference between the molecular mechanics result and that of the X - ray investigation.

[†] definition of $\Delta$ see Table II .13.

TABLE II .15 (continued)

| atom | apex | atom | X-ray | A | $\delta_A$§ | B | $\delta_B$ |
|---|---|---|---|---|---|---|---|
| C21 | C13 | C15 | 108(1) | 108 | 0 | 108 | 0 |
| C21 | C13 | C14 | 126(1) | 127 | 1 | 126 | 0 |
| C15 | C13 | C14 | 126(1) | 126 | 0 | 126 | 0 |
| C13 | C15 | C16 | 125(1) | 126 | 1 | 126 | 1 |
| C17 | C15 | C13 | 110(1) | 108 | - 2 | 108 | - 2 |
| C17 | C15 | C16 | 125(1) | 126 | 1 | 126 | 1 |
| C15 | C17 | C18 | 127(2) | 126 | - 1 | 126 | - 1 |
| C15 | C17 | C19 | 107(1) | 108 | 1 | 108 | 1 |
| C19 | C17 | C18 | 126(2) | 126 | 0 | 126 | 0 |
| C17 | C19 | C20 | 129(2) | 126 | - 3 | 127 | - 2 |
| C21 | C19 | C17 | 108(1) | 108 | 0 | 108 | 0 |
| C21 | C19 | C20 | 123(2) | 126 | 3 | 126 | 3 |
| C13 | C21 | C19 | 107(1) | 108 | 1 | 108 | 1 |
| C13 | C21 | C22 | 125(1) | 126 | 1 | 126 | 1 |
| C19 | C21 | C22 | 127(1) | 126 | - 1 | 127 | 0 |
| Δ for angles NOT at C5 and C6 | | | | | $\Delta_A = 2.4$ | | $\Delta_B = 2.1$ |
| | | | | | | | |
| C4 | C5 | C6 | 116(2) | 115 | - 1 | 120 | 4 |
| C5 | C6 | C1 | 108(2) | 113 | 5 | 118 | 10 |
| Δ for angles AT C5 and C6 | | | | | $\Delta_A = 3.0$ | | $\Delta_B = 7.0$ |

TABLE II .16 Comparison of Bond Angles (°) for **II** with those obtained from molecular mechanics calculations with C5 and C6 as Aliphatic (A) and Aromatic (B).

| atom | apex | atom | X-ray | A | $\delta_A$[§] | B | $\delta_B$ |
|---|---|---|---|---|---|---|---|
| C15 | Ir | C13 | 38.5(4) | 39.8 | 1.3 | 39.9 | 1.4 |
| C2 | Ir | C3 | 39.6(4) | 40.4 | 0.8 | 40.4 | 0.8 |
| C15 | Ir | C17 | 38.4(5) | 39.9 | 1.5 | 40.0 | 1.6 |
| C2 | Ir | C1 | 40.8(5) | 37.0 | - 3.8 | 37.2 | - 3.6 |
| C13 | Ir | C21 | 37.5(5) | 39.9 | 2.4 | 39.9 | 2.4 |
| C4 | Ir | C3 | 38.8(5) | 37.2 | - 1.6 | 36.7 | - 2.1 |
| C17 | Ir | C19 | 37.3(5) | 40.0 | 2.7 | 40.1 | 2.8 |
| C4 | Ir | C1 | 72.4(5) | 74.3 | 1.9 | 72.9 | 0.5 |
| C21 | Ir | C19 | 36.2(5) | 40.0 | 3.8 | 40.1 | 3.9 |
| Δ[†] for angles at Ir | | | | $\Delta_A = 2.2$ | | $\Delta_B = 2.1$ | |
| C7 | S | C1 | 94.5(6) | 90.2 | - 4.3 | 89.9 | - 4.6 |
| C6 | C1 | C2 | 119(1) | 126 | 7 | 123 | 4 |
| C6 | C1 | S | 118(1) | 123 | 5 | 125 | 7 |
| C2 | C1 | S | 107(1) | 112 | 5 | 112 | 5 |
| C3 | C4 | C5 | 122(1) | 124 | 2 | 122 | 0 |
| C3 | C2 | C8 | 133(1) | 127 | - 6 | 128 | - 5 |
| C3 | C2 | C1 | 113(1) | 120 | 7 | 119 | 6 |
| C8 | C2 | C1 | 114(1) | 113 | - 1 | 113 | - 1 |
| C12 | C7 | C8 | 122(1) | 122 | 0 | 122 | 0 |
| C12 | C7 | S | 126(1) | 126 | 0 | 126 | 0 |
| C8 | C7 | S | 112(1) | 112 | 0 | 112 | 0 |
| C4 | C3 | C2 | 112(1) | 119 | 7 | 119 | 7 |
| C9 | C8 | C7 | 120(1) | 120 | 0 | 120 | 0 |
| C9 | C8 | C2 | 128(1) | 128 | 0 | 128 | 0 |
| C10 | C11 | C12 | 122(1) | 120 | - 2 | 120 | - 2 |

---

[§] $\delta$ is the difference between the molecular mechanics result and that of the X - ray investigation.

[†] definition of Δ see Table II .13.

TABLE II.16 (continued)

| atom | apex | atom | X-ray | A | $\delta_A$§ | B | $\delta_B$ |
|---|---|---|---|---|---|---|---|
| C7 | C8 | C2 | 112(1) | 113 | 1 | 113 | 1 |
| C7 | C12 | C11 | 117(1) | 118 | 1 | 119 | 2 |
| C21 | C13 | C15 | 108(1) | 108 | 0 | 108 | 0 |
| C21 | C13 | C14 | 128(1) | 127 | - 1 | 127 | - 1 |
| C8 | C9 | C10 | 120(1) | 119 | - 1 | 119 | - 1 |
| C15 | C13 | C14 | 123(1) | 126 | 3 | 125 | 2 |
| C11 | C10 | C9 | 120(2) | 121 | 1 | 121 | 1 |
| C17 | C15 | C13 | 106(1) | 108 | 2 | 108 | 2 |
| C17 | C15 | C16 | 125(1) | 126 | 1 | 126 | 1 |
| C13 | C15 | C16 | 128(1) | 126 | - 2 | 126 | - 2 |
| C21 | C19 | C17 | 109(1) | 108 | - 1 | 108 | 0 |
| C21 | C19 | C20 | 126(1) | 125 | - 1 | 126 | 0 |
| C17 | C19 | C20 | 125(1) | 127 | 2 | 126 | 1 |
| C19 | C17 | C15 | 108(1) | 108 | - 1 | 108 | 0 |
| C19 | C17 | C18 | 126(1) | 126 | 0 | 126 | 0 |
| C19 | C21 | C13 | 109(1) | 108 | - 1 | 108 | - 1 |
| C15 | C17 | C18 | 126(1) | 126 | 0 | 126 | 0 |
| C19 | C21 | C22 | 129(1) | 126 | - 3 | 126 | - 3 |
| C13 | C21 | C22 | 122(1) | 126 | 4 | 126 | 4 |
| <u>Δ for angles NOT at C5 and C6</u> | | | | $\Delta_A = 2.1$ | | $\Delta_B = 1.8$ | |
| | | | | | | | |
| C6 | C5 | C4 | 110(1) | 115 | 5 | 120 | 10 |
| C1 | C6 | C5 | 109(1) | 113 | 4 | 118 | 9 |
| <u>Δ for angles AT C5 and C6</u> | | | | $\Delta_A = 4.5$ | | $\Delta_B = 9.5$ | |

# CONCLUSION

The above comparisons between the X-ray diffraction structural results and the molecular mechanics modeling results show that in the molecular mechanics calculation, if methylenic C5 and C6 carbons are assumed, the deviations of the results from that of the X-ray diffraction investigations are much smaller. This further confirms that C5 and C6 are of $sp^3$ character instead of $sp^2$, and hence there should be two hydrogen atoms associated with C5 and C6 respectively, in both structures **I** and **II**. The conversion of C5 and C6 in the phenyl ring of the reactant to aliphatic carbons in the resultants is most likely due to the over reduction of the complexes by the strong reducing reagent aluminum hydride.

In the crystallographic approach, the power of an X-ray diffraction structural determination to reveal the "real" configuration of the crystallized compound is demonstrated. Also one can see that molecular mechanics modeling can be another powerful tool and be a good supplement to the former, and can confirm some "suspicious" points in the results of the former. Molecular mechanics modeling can even make some "difficult to solve" structures possible by the X-ray methods. As an example, one can refer to the recent research results of the combination of X-ray diffraction structure determination and molecular mechanics modeling in our group[7].

# REFERENCES

[1] Johnson, C. A. ***ORTEP - II: A Fortran Thermal - Ellipsoid Plot Program for Crystal Structure Illustration***, U. S. Atomic Energy Commission Report ORNL - 3794 ($2^{nd}$ revision with supplemental instruction), Oak Ridge National Laboratory, Oak Ridge, Tenn., 1970.

[2] Ulich Burkert and Norman L. Allinger, ***Molecular Mechanics***. (ACS Monograph 177. Washington, D. C. 1982).

[3] ***PCMODEL***, A Modification of Allinger's MM2 Program, distributed by Serena Software, Box 3076, Bloomington IN.

[4] Wilson, E. B. Jr., Decius, J. C., Cross, P. C., ***Molecular Vibrations***. (McGraw - Hill: New York, 1955).

[5] Gans, P., ***Vibrating Molecules***. (Chapman & Hall: London, 1971).

[6] Herzberg, G., ***Infra-Red and Raman Spectra***. (Van Nostrand - Reinhold: New York, 1945).

[7] Day, C. L. and Jacobson, R. A., ***Structure Determination of*** $(\eta^2$ ***- Diphenylacetylene) - Titanium (Octaethylporphyrin); Combining X-ray Diffraction and Molecular Mechanics Methods***, 1991 American Crystallographic Association Annual Meeting, Toledo, Ohio, July 21 - 26, 1991, paper PE 08.

[8] Mark R. Mason, Yingzhong Su, Robert A. Jacobson and John G. Verkade, ***Bidentate and Tridentate coordination Modes of a Novel Bicyclic Ditertiary Phosphine Ether***, *Organometallics,* 10, 2335(1991).

[9] Kraus, G. A., Bougie, D., Jacobson, R. A. and Su, Y. - Z., ***The Urea Connection. Intramolecular Diels - Alder Reaction of Ureas***, *J. Organ. Chem.,* 54, 2425(1989).

[10] Glavee, G. N., Su, Y.-Z., Jacobson, R. A. and Angelici, R. J., ***Reactions of*** $C_pFe(CO)_2(=COCH_2CH_2O)^+$, $C_pFe(CO)_2[=C(SMe)_2]^+$ ***and Related Carbene Complexes with Reducing Agents and Nucleophiles. The Structure of*** $C_pFe(CO)_2[=C(SMe)_2]\bullet PF_6$, *Inorgan. Chim. Acta,* 157, 73 - 84(1989).

[11] Kraus, G. A., Thurston, J., Thomas, P. J., Jacobson, R. A. and Su, Y., *2-Benzoyloxynitroethylene as a Cis-2-Aminoethenol Equivallent*, *Tet. Lett.*, 29, 1879(1988).

[12] Jiabi Chen, Yingzhong Su, Robert A. Jacobson, and Robert J. Angelici, *Hydride Addition to and Reduction of* $C_p^*Ir(\eta^6\text{-}BT)^{2+}$ *and* $C_p^*Ir(\eta^6\text{-}DBT)^{2+}$, *where BT = benzo[b]thiophene and DBT = dibenzothiophene*, *J. Organomet. Chem.*, (accepted for publication).

[13] Ahmad A. Naiini, Yingzhong Su, Sharon L. Ringrose, Robert A. Jacobson and John G. Verkade, *Synthesis and Reactivity Studies of diethylaminotitanatrane: X-ray Structural Characterization of* $iso\text{-}Pr\text{-}S\text{-}Ti(OCH_2CH_2)_3N$ *and* $N(CH_2CH_2O)_3Ti\text{-}OC(Me)_2O\text{-}Ti(OCH_2CH_2)_3N$, (to be published).

# SECTION III

# AN ALIGNMENT PROCEDURE FOR A HILGER-WATTS DIFFRACTOMETER ON A RIGAKU ROTATING ANODE X-RAY GENERATOR

# INTRODUCTION

Alignment of an X-ray diffractometer is a necessity both as part of initial installation and at other times, especially after changing a filament in a rotating anode X-ray generator, or changing a sealed X-ray tube.

Alignment is usually carried out following the instructions provided by the manufacturer, with the X-ray beam produced by the generator as the detectable medium.

When the diffractometer is completely out of alignment, using X rays to align the diffractometer can be tedious and sometimes even hazardous; the X-ray beam is often not confined in a safe path, and the person carrying out the alignment could be in danger of being exposed to the X rays scattered by the off-alignment parts for a long time, even though the scattered beam is of low intensity. Usually the only way to determine the position of the X-ray beam is by using a fluorescent screen or an alignment jig with fluorescent material pasted around the jig hole. A person often needs to approach very close to the fluorescent spot since the fluorescence is weak.

In order to obtain a crude alignment before the more precise X-ray alignment is performed, an optical alignment procedure making use of ordinary optical telescopes was developed. This provides a visible alignment operation as contrasted to the use of the invisible, hazardous X-ray trial-and-error type of operation. This was carried out on a Hilger-Watts diffractometer with a RIGAKU Rotating Anode X-ray generator as well as a DATEX diffractometer with a sealed X-ray tube; both resulted in a quick and safe alignment.

The Hilger-Watts four-cycle diffractometer was manufactured in the early 1960s and two such units were purchased by the Ames Laboratory in the mid-1960s for X-ray and for neutron diffraction. The Hilger-Watts diffractometer's design is different from most of the other units available today. Its measuring system is entirely free from the mechanical effects of wear and backlash, since the movement and the positioning of its four circles are controlled by a Moiré fringe technique:

The four circles are engraved with radial gratings (3,600 lines in $\omega$, $\phi$ and $\chi$; 1,800 lines in $2\theta$), and the measuring heads are fitted with a small segment of a similar crossed grating as a reference. Light is projected through the two gratings and, as the circle revolves and the gratings move past one another, a Moiré fringe pattern travels across the field at right angles to the direction of movement.

The measuring head, which contains a lamp and a photocell assembly, examines the fringe movements through four separate silicon photocells whose output takes the shape of approximately sinusoidal waveforms in quadrature (Figure III . 1) thus providing complete and continuous information about the direction of the movement and the position of the circle.

The sinusoidal output from the measuring heads is converted electronically into one tenth fringe increments, and these represent circle displacements of 0.01° for $\omega$, $\phi$ and $\chi$ circles, and 0.02° for $2\theta$ circle. These are entirely unaffected by the gearing or by backlash in the drive.

Each radial grating is marked with a datum point which is detected by a separate measuring head to the same accuracy; so an automatic check can be made on the setting accuracy at any time. The absolute position of the circles can be read from scales and micrometer heads.

The diffractometer ceased being used since the late 1960s due to the instability of the light source (the lamp deteriorates during usage, thus affecting the intensity detected by the photocell assembly) and instabilities in the related electronic parts. Both diffractometers were put into storage.

Recently a decision was made by Dr Jacobson after discussion with Harold Skank, head of the Instrumentation Services Department in the Ames Laboratory, to try to place one of these units back into operation, and make use of a free port of the high intensity RIGAKU Rotating Anode X-ray generator. This seemed feasible because a new type of light source is now available which is a solid state device, a light emitting diode, with very long life time, and electronic components for the detector assembly are now available with much more stable characteristics. Thanks to the effort of Harold Skank and workers in his Instrumentation Services Department and the Machine Shop of the Ames Laboratory, one diffractometer was reassembled making use of parts from the two stored Hilger-Watts units. It now resides on one of the two X-ray ports of the RIGAKU Rotating Anode X-ray generator. The design of parts for collimator housing and related hardware and the alignment of this unit were done by the author of this dissertation.

In this section, details regarding the combination of the optical and X-ray alignment procedure employed for the Hilger-Watts diffractometer is discussed on a step-by-step basis.

Figure III .1 'Moiré fringe patterns and the sinusoidal output of the measuring head on the patterns.

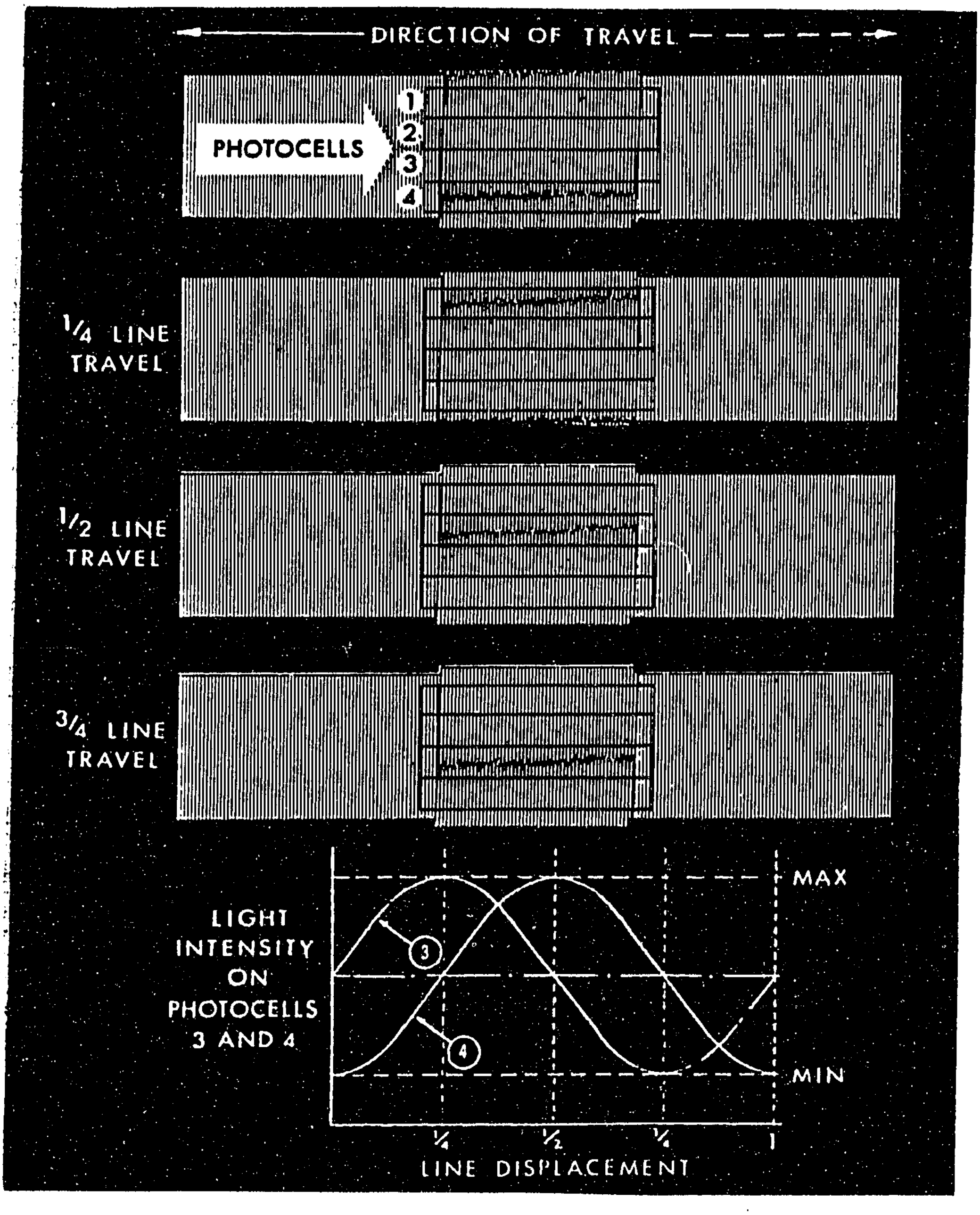

# LEVELING AND VERIFYING POINT OF AXIAL INTERSECTION IN THE ALIGNMENT OF THE DIFFRACTOMETER

1. Level the diffractometer base:

Put an air bubble level on the round track for the Theta arm. For two perpendicular orientations of the level on the track, make the bubble reside at the middle line, by turning the three bolts, if necessary.

2. Level the Theta arm:

Set Theta at 0°. Put the level on top of the counter and shim it if necessary to make the bubble reside on the middle line. When turning theta from the positive maximum to negative maximum angle; the bubble should stay invariant.

3. Adjust the intersection of the goniometer axes to a common point:

This is done by mounting a needle on the goniometer head, and rotating the Phi, Chi and Omega axes. On viewing from a leveled telescope which may have to be set beside the diffractometer on the same table, with its internal cross hairs well focussed, the position of the tip should be invariant with respect to the intersection of the hairs upon rotations. If not, the position of the needle with respect to the goniometer head should be adjusted if deviation appears upon Phi rotation, or the position of the goniometer head and the Phi motor assembly should be adjusted with respect to the

Chi-circle if deviation appears upon Chi rotation.

4. Alignment of the Phi and Omega axes:

This is done by setting Chi = 0°, rotating Phi in one direction, followed by a rotation of Omega in the opposite direction by the same amount. The position of the tip of the needle should be invariant. If not, the base of the Chi-circle must be shimmed.

# SETTING ANGLES FOR THE MONOCHROMATING CRYSTAL AND OBTAINING AN X-RAY BEAM

1. Close the shutter via the panel switch and bring the generator up.

2. Fit a round piece of fluorescent screen onto the slit holder opening with the fluorescent side out, and mark the vertical diameter of the slit holder opening on it.

3. Unlock the crystal holder clamping screw and the slit holder clamping screw. Set both the angle of the monochromating crystal ($\theta$) and the angle of the reflected beam ($2\theta$) to zero. Push the slit holder into the microswitch and use scotch tape to fix this position, so that the microswitch stays depressed and the shutter switch on the panel can function.

4. Shield the beam path at the end of the table with a thick sheet of lead. **Be careful, you will be dealing with the strong direct beam from the anode!** Turn off the light in the lab. Open the shutter on the panel. A round, evenly bright image of the primary beam should be seen on the round fluorescent screen and the vertical diameter of the spot should be coincident with the mark on the screen. If not, move the slit holder or turn the crystal vernier to make it so. This is the zero angle for both the monochromating crystal and the reflected beam. Turn on the light in the lab.

5. Turn the crystal approximately 6° away and move the slit holder 12° away from their zero points if a graphite monochromator is used, as the Bragg angle of Mo K$\alpha$ is about 6.08° for its (0002) plane. Knowing that only that portion of the primary beam that is on a plane 6.08° away from the graphite crystal (0002) plane would be reflected, one would expect that the reflection will take the shape of the intersection of two planes, i.e., a bright vertical line should be seen on the fluorescent screen. Fine tune both the crystal and the slit holder to make this line as sharp as possible and let the brightest part of it fall on the mark of the fluorescent screen. Lock the $\theta$ position with the crystal holder clamping screw and note the $2\theta$ monochromator position. These angles must not be changed. Close the shutter. Carefully take off the fluorescent screen.

# ALIGNMENT OF THE DIFFRACTOMETER WITH THE MONOCHROMATED BEAM

1. Determine a crude straight line passing through the center of the slit holder opening and the center of the diffractometer:

Take away the incident and receiving collimators as well as the beam detector from their stands.

Position the diffractometer such that the center of the four circles, the axis of the incident and receiving collimators and the center of the opening of the beam detector are approximately coincident with the monochromated beam, and such that if the incident collimator were mounted on its stand and slid into the slit holder, it would depress the microswitch and do so without changing the slit holder angle $2\theta$.

Position a long focal length telescope I, with its internal cross hairs having been very well focused, approximately onto the monochromated (secondary) beam. This can be done by proceeding as follows:

On viewing from the detector end, adjust the position of the diffractometer as well as the position of the telescope such that when focussed individually, the tip of the needle, and the center of the circle of the slit holder opening falls at the intersection point of the hairs of the telescope, respectively.

2. Find the path of the secondary X-ray beam and make it pass through the

center of the diffractometer:

Replace the goniometer head with the alignment jig. Use the telescope to make sure that the pin hole of the jig resides at the same point as the tip of the pin on the goniometer head did. Set Chi = 90° and Phi = 90°. Unlock the Phi shaft and turn the flat side of the pin hole up. Put a level on the flat side, lock the shaft and fine tune the Phi angle with the two screws adjacent to the clamping screw of the Phi shaft such that the flat side is levelled according to the air bubble of the level. Set the Phi angle at either 0° or 180° using program SETTER such that the fluorescent material pasted around the pin hole of the jig faces the incident beam.

Set up telescope **II** on the monochromator side and focus on the pin hole of the alignment jig.

Turn off the light in the lab. Open the shutter. The secondary X-ray beam should come out from the monochromator and cast a vertical bright line on the fluorescent material of the alignment jig. Viewing through telescope **II**, the pin hole of the jig should coincide with the maximum intensity of this line. If not, carefully tap the legs of the diffractometer to move the pin hole to make it so.

3. Make the axis of telescope **I** coincident with the secondary X-ray beam path:

Turn on the light in the lab. Close the shutter. Carefully tear off the scotch tape used to keep the microswitch depressed. Remove the radiation protection cover from the top of the monochromator drum.

Illuminate the inside of the opened monochromator drum with a strong lamp. Turn Phi to + 90° or - 90° so that the flat part of the jig will not completely block the opening of the slit holder. View through telescope I and, by focusing on the inside of the monochromator drum, one should see the image of the tunnel of the primary beam path being reflected by the mirror-like graphite crystal as a dark round spot on the background of the shiny copper metal. If the graphite crystal is perfectly vertical and so is the shaft of Omega (or that of Phi when Chi = 0°), the path of the secondary X-ray beam should be coincident with the straight line defined by the center of this dark spot and the center of the pin hole of the alignment jig.

Focus on the center of the dark spot, and move the telescope so as to make the intersection point of the hairs coincide with the center of the dark spot.

Turn the Phi angle such that the flat part of the alignment jig faces telescope I. Focus back to the pin hole to see if the intersection point of the hairs falls on the center of the pin hole.

More often than not, one has to adjust the height, the position and the orientation of telescope I so that when one focuses back and forth on the pin hole and the dark spot, the intersection point of the hairs of telescope I always falls on their centers. What one actually needs to do is to scan the vector which originates from the center of the dark spot and points to the intersection point of the hairs, to make it go through the pin hole. That is to say, in each movement, one has to imagine the axis of the telescope pointing to the center of the dark spot, even if it is not focussed there. In making adjustments, one must realize that the image of either the pin hole or the dark spot one sees in the telescope may be reversed, depending on the telescope used. If this is the case, each movement should go in the opposite direction. For example, if one sees that the pin hole is in the upper left quadrant formed by the cross hairs, imaging that the axis of the telescope always points to the center of the dark spot, one first moves the telescope laterally to the right hand side to make the center of the pin hole fall at the vertical hair, then lowers the height to make it fall at the intersection point.

After achieving the above, one may find that the wall of the pin hole is not lined up with the axis. When this occurs, one has to repeat the above two steps after making a small adjustment in the Phi angle to achieve a perfect coincidence of the axis of the telescope with the path way of the secondary beam.

4. Positioning the incident collimator:

This is done by putting the axis of the incident collimator onto the straight line defined above.

Adjust the y - slide and z - slide of the incident collimator stand such that when you move the collimator housing along the x - slide to let it sit into the slit holder and push against the microswitch, it will not hit the wall of the slit holder to change the $2\theta$ angle position of the holder.

After the incident collimator has been inserted into the slit holder and all slides are locked, turn Phi to 90° and turn the set screws on the incident collimator housing for the outlet hole (close to the alignment jig) until the light reflected from the inside of the monochromator drum can be seen. Then fine turn the inlet and outlet holes of the collimator such that when focused on either hole, the intersection point of the hairs is coincident with the center of the holes.

5. Positioning the receiving collimator:

This is done by a similar procedure to that of the incident collimator as described above. One has to turn the set screws on the inlet end or shim the outlet end to make the center of the two circular holes fall at the intersection point of the hairs when these two holes are focused with telescope I.

# CONFIRMATION OF THE ALIGNMENT

Focus on:

(a) the image of the primary X-ray beam tunnel;

(b) the inlet circle of the incident collimator;

(c) the outlet circle of the incident collimator;

(d) the pin hole of the alignment jig facing telescope **I**;

(e) the inlet circle of the receiving collimator; and

(f) the outlet opening of the receiving collimator [ darker and bigger then (e) ], respectively, with telescope **I**; the center of each of them should fall on the intersection point of the hairs. One should also be able to see the light reflected from inside the monochromator drum even when the pin hole of the alignment jig faces telescope **I**. By using a small piece of white paper and moving it in and out of the front of the tunnel inside the illuminated monochromator drum, one can also verify through the pin hole that the light is blinking.

## TESTING THE ALIGNMENT WITH THE X-RAY BEAM

Mount the detector, and shield its receiving opening with thin metal sheets such that the direct beam is attenuated in order to prevent the detector from being damaged or being overexposed.

Turn off the light in the lab. Open the shutter. On looking through telescope II, one should see that a round, bright spot, caused by collimation of the secondary X-ray beam by the incident collimator, is being emitted by the fluorescent material of the alignment jig around the pin hole. If the round spot is not centered on the pin hole, fine tune the set screws on the outlet end of the incident collimator.

By placing a commercial square fluorescent screen between the alignment jig and the receiving collimator, one can detect the beam as a smaller bright round spot after it has passed through the pin hole.

With the aid of a small piece of fluorescent screen glued on the inlet end of the receiving collimator, and having a hole pierced it through the inlet hole, one can easily trace the beam path into the hole. If any deviation occurs, one can turn off the power to the diffractometer motors and manually turn the detector arm to cast the beam into the hole. In addition to viewing this by eye, one can use the rate meter on the panel for the optimal 2 - Theta zero position by noting where the maximum reading occurs on the rate meter when turning the 2 - Theta arm.

Finally, one opens and closes in turn the upper - lower and left - right half slits on the outlet end of the receiving collimator and watches the reading on the rate meter to make sure the half opening of the outlet circle cuts half of the radiation. Should any deviation occur, one needs to fine tune the position of outlet end of the receiving collimator to correct it.

Once this is done, this phase of the alignment procedure is completed, The program DOIT should be run with a reflection near CHI = 90° to obtain instrument zeroes and determine whether any additional fine adjustments need be made.

# GENERAL SUMMARY

This dissertation is divided into three sections.

In Section I, the grain size determinations of powder materials by various methods were discussed and compared; these included the convolution methods used in the Rietveld refinement, the "direct" investigation by the transmission electron microscope, and a computer program for Fourier deconvolution developed by the author of this dissertation. Emphasis was on the treatment of noise and discontinuities associated with the patterns of the standard sample and the sample of interest; this was shown to be a key factor regarding the successfulness of the backward Fourier transformation in obtaining the deconvoluted peak associated with the grain size effect. After cubic-spline-smoothing the raw data patterns, and truncating the Fourier transformed patterns at the right points, the deconvolution method gave results for grain size which were found to be in excellent agreement with those from the transmission electron microscope investigation. It seems that the Fourier deconvolution method is indeed a "most powerful technique"[2] in dealing with the analysis of grain size (and also of stress, if it exists in the sample), including the revelation of the characteristics of the peaks responsible for the grain size and stress respectively, since this method does not assume any particular peak shape function in determination of the peak broadening which is used in the Scherrer's equation for the grain size calculation.

In Section II, X-ray investigation of metal complexes containing a nominal benzo-ligand, namely, I: benzo-[2,3]-4-methyl-thiophene, $C_9H_{10}S$-Ir-[$C_5(CH_3)_5$], and II: dibenzothiophene, $C_{12}H_{10}S$-Ir-[$C_5(CH_3)_5$] were described. The results indicated the two carbon atoms in the benzo-group two carbon atoms which are not coordinating with the Ir atom now had an $sp^3$ character in this coordinated ligand; molecular mechanics also confirmed this result. Molecular mechanics modeling can be a promising supplement to X-ray diffraction structure determination.

Section III presents an optical alignment procedure using ordinary optical telescopes, instead of directly using hazardous X rays, to align a recently reassembled Hilger-Watts four-cycle diffractometer on a Rigaku rotating anode X-ray generator. This procedure provides efficient, safe and accurate alignment, especially when the instrument is completely out of alignment.

## ACKNOWLEDGEMENTS

I would like to use this opportunity to express my gratitude to my supervisor Dr. Robert A. Jacobson for his guidance and encouragement in my course of study in ISU. Without him this dissertation would be impossible. His patience and kindness in treating people deeply impressed me and he himself provides a model for me to imitate.

I would also like to thank the former and present group members Sangsoo Kim, Lance Miller, Musiri Janakiraman, Thom Hendrixson, Shumei Yang, Cathy Day, Sharon Ringrose and our secretary Brenda Smith for their helping me to understand crystallography and to know how to run the instruments and the programs to solve the structures, their interest in my research and their friendship to make the group like a family. I will never forget the warm congratulations when my son Jeremy was born just as I started writing this thesis.

Thanks are also directed to Chi-Ming Hsu, Drs. Bill McCallum, Jeff Shield, David Echels and Marlene Frisk for their help.

Finally, and most importantly, I thank my mother and my wife Ziwen, to whom I dedicate this dissertation. Without their full support, love and sacrifice neither this dissertation nor even my study in America would be realistic.

This work was performed at under contract No. W-7405-Eng-82 with the U. S. Department of Energy and this thesis has been assigned a report number IS-T-1591.